University of Groningen

Correlations between charge, orbital, and spin degree of freedom in magnetic competing systems

Handayani, Ismudiati

IMPORTANT NOTE: You are advised to consult the publisher's version (publisher's PDF) if you wish to cite from it. Please check the document version below.

Document Version
Publisher's PDF, also known as Version of record

Publication date:
2014

Link to publication in University of Groningen/UMCG research database

Citation for published version (APA):
Handayani, I. (2014). *Correlations between charge, orbital, and spin degree of freedom in magnetic competing systems*. [Thesis fully internal (DIV), University of Groningen]. s.n.

Copyright
Other than for strictly personal use, it is not permitted to download or to forward/distribute the text or part of it without the consent of the author(s) and/or copyright holder(s), unless the work is under an open content license (like Creative Commons).

The publication may also be distributed here under the terms of Article 25fa of the Dutch Copyright Act, indicated by the “Taverne” license. More information can be found on the University of Groningen website: https://www.rug.nl/library/open-access/self-archiving-pure/taverne-amendment.

Take-down policy
If you believe that this document breaches copyright please contact us providing details, and we will remove access to the work immediately and investigate your claim.

Downloaded from the University of Groningen/UMCG research database (Pure): http://www.rug.nl/research/portal. For technical reasons the number of authors shown on this cover page is limited to 10 maximum.

Download date: 05-05-2023

Correlations between Charge, Orbital, and Spin Degrees of Freedom in Magnetic Competing Systems

Ismudiati Puri Handayani

university of groningen

faculty of mathematics and natural sciences

zernike institute for advanced materials

The work described in this thesis was performed in the group "Optical Condensed Matter Physics" (part of the Zernike Institute for Advanced Materials) of the University of Groningen, The Netherlands. The PhD program of Ismudiati Puri Handayani is financially supported by the Schlumberger Faculty for Future Program and Netherland Fellowship Program

Zernike Institute PhD thesis series 2014-09
ISSN : 1570-1530
ISBN : 978-90-367-6956-3 (electronic version)
ISBN : 978-90-367-6955-6 (printed version)

Front cover : Illustration of octahedrals shined by light
Back cover : Illustration of *d*-orbitals
Cover design : Iwan Cony Setiadi
Printed by : Offpage, The Netherlands, April 2014

rijksuniversiteit
groningen

Correlations between Charge, Orbital, and Spin Degrees of Freedom in Magnetic Competing Systems

Proefschrift

ter verkrijging van de graad van doctor aan de
Rijksuniversiteit Groningen
op gezag van de
rector magnificus dr. E. Sterken
en volgens besluit van het College voor Promoties.

De openbare verdediging zal plaatsvinden op

vrijdag 2 mei 2014 om 14.30 uur

door

Ismudiati Puri Handayani

geboren op 12 maart 1976
te Magelang, Indonesië

Promotor
Prof. dr. ir. P.H.M. van Loosdrecht

Co-promotor
Dr. A.A. Nugroho

Beoordelingscommissie
Prof. dr. D. Khomskii
Prof. dr. M. O. Tjia
Prof. dr. B. Noheda Pinuaga

untuk Ibu

Contents

Chapter 1

Introduction

The transition metal oxides have been a subject of great research interest owing to their rich variety of interesting and important properties discovered in this class of materials. The *d*-electrons responsible for those properties are known to constitute the strongly correlated electron systems which must be treated as many body systems. Given the additional attribute of electron spin, the strongly correlated electron systems have been shown, both theoretically and experimentally, to exhibit antiferromagnetic (AFM) insulating ground state which undergoes a transition to ferromagnetic (FM) metallic state upon the increase of Coloumbic correlation strength or equivalently an increase in electron density. This phenomenon has been well explained on the basis of the Hubbard model. In addition to charge and spin, Kugel-Khomskii further introduced the importance of orbital degree of freedom in controlling the properties of transition metal oxides [1]. The interplays among charge, orbital, and spin degrees of freedom have proved to play the major roles in a number of new and important phenomena such as superconductivity [2], colossal magnetoresistance [3–6], and multiferroicity [7–9].

Along with other important experimental methods, optical spectroscopy has been widely utilized to uncover and explain the unique properties of strongly correlated systems [10–13]; for example , the coupling between conducting carriers and spin fluctuation in superconductor materials has been studied using infrared spectroscopy [11] and the coincidence between anomalous phonon behaviors with the onset of superconductivity has been observed by Raman spectroscopy [14]. In manganites, optical spectroscopy has provided important information concerning the electronic structures [15–17], signature of metal to insulator transition [18], magnetic and ferroelectric transition in multiferroics [19–21], spin-phonon coupling [22, 23], signature of charge/orbital melting [24], and transient hidden phase [25].

In this thesis, the study is focused on the roles of interplay between charge, lattice, orbital, and spin degrees of freedom in multiferroic compound $TbMnO_3$ (TMO), the half-doped layered manganite $Pr_{0.5}Ca_{1.5}MnO_4$ (PCMO), and geometrically frustrated system of $KFe_3(OH)_6(SO_4)_2$ (iron jarosite). In these magnetic systems, the presence of different types of exchange interactions are known to give rise to magnetic competition resulting in a variety of magnetic phases. In several cases, this competition even creates magnetic frustration in the systems [26, 27]. One of the major work reported here is the time resolved experiments performed to study the interplay between the photo excited electrons and the magnetic structure in TMO, as well as the relaxation process of the excited electron which is strongly coupled to the magnetic sub-lattices. In this connection, the modulation of ferroelectric polarization induced by photo-excitation is also investigated. Raman spectroscopy, in combination with X-ray diffraction (XRD) measurement as well as thermodynamic measurement techniques, charge transport, and specific heat measurements are used to explore the correlations between lattice dynamics and charge, orbital, as well as the spin degrees of freedom in PCMO. Further, the effects of optical excitation on the charge, orbital, and spin orderings are studied by time resolved pump probe spectroscopy. In particular the study is aimed to yields information on the photo-induced lattice/orbital disorder as well as the role of the magnetic system in providing the decay channels for the excited electrons. Raman spectroscopy is also used to study magneto electric and magneto elastic couplings in iron jarosite in relation to the activation of the associated phonon modes.

In this chapter, a brief description of the competing magnetic systems in manganite and iron jarosite is presented in section 1.1. The charge, orbital, and spin ordering are summarized in section 1.2 to give an overview of the different phases and their transitions. In section 1.3, the phenomena observed by a time resolved pump probe experiment and Raman spectroscopy are presented. Finally, section 1.4 gives an overview of the scope of this thesis.

1.1 Magnetically Competing Systems

In a geometrically frustrated system, the geometrical structure gives rise to a magnetically competing effect in the system where the magnetic interaction between spins can not be minimize simultaneously. Fig. 1.1 (a) shows a simple descriptions of triangular coordination where two spins are oppositely aligned to fulfill the minimum energy of AFM ground state while the third spin cannot minimize its magnetic interaction with the other two spins with either FM of AFM ground state simultaneously. The degree of frustration is measured by the "frustration index" $f = \theta_{cw}/T_c$ where θ_{cw} and T_c are the Currie-Weiss temperature and magnetic ordering temperature, respectively. Th spin frustration is known to lead to a large degree of degeneracy in the ground state and to the appearance of complex magnetic structures. This system is sensitive to small external perturbations such as the variations of temperature and magnetic field. Under certain conditions, the unusual magnetic phases as spin glass, spin liquid, and spin ice have been observed [26, 28–30].

Another example of a quasi-two-dimensional geometrically frustrated system

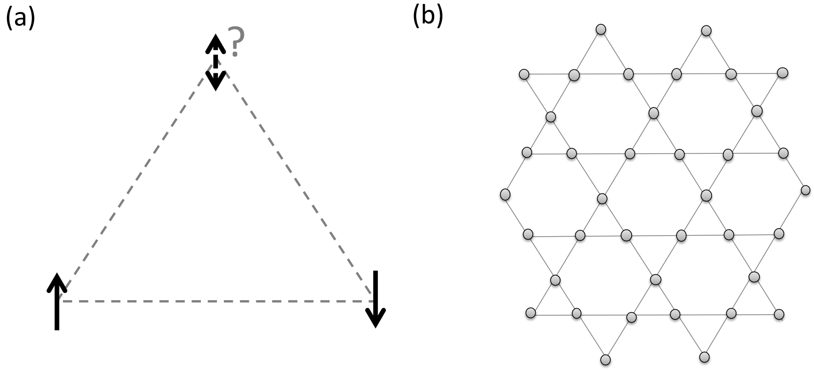

Figure 1.1: *(a) Geometrically frustrated system in triangular lattice. (b) Kagomé lattice.*

is found when the magnetic ions forms a kagomé lattice, as shown in Fig. 1.1 (b). It differs from the triangular lattice in the presences of corner-sharing triangulars. One of the kagomé systems is found in the jarosite compound. Even though it has a geometrically frustrated structure, a particular lattice symmetry allows the existence of the asymmetric Dzyaloshinsky-Moriya interaction, which might trigger a long range magnetic ordering at a finite temperature [31].

The pervoskite manganite $RMnO_3$ is another system with magnetic competition, as shown in Fig. 1.2. The staggered $d_{3x^2-r^2}/d_{3y^2-r^2}$ orbital configuration in the *ab*-plane creates FM interactions between nearest neighbor (NN) e_g orbitals along the diagonal direction (J_1<0) and AFM interactions between next nearest neighbors (NNN) along the *b*-axis (J_2>0). When the distances between NN manganite ions are much shorter than that of NNN, the FM interaction becomes dominant and the AFM interaction is negligible. In the presece of $GdFeO_3$-type distortion, the distance along the *b*-axis is shorted and the NNN interaction can not be neglected. Consequently, ferromagnetic and antiferromagnetic interaction becomes comparable leading magnetic frustration in this system.

The competition between FM and AFM interactions creates different types of magnetic ground states at a low temperature depending on the ionic radius of rare earth element (R), as shown in Fig. 6.3 [27, 32, 33]. In perovskite manganite $RMnO_3$ with large radius of R such as $LaMnO_3$, A-type AFM is formed. In manganites with an intermediate R radius such as $GdMnO_3$, $TbMnO_3$, and $DyMnO_3$, competition between FM and AFM magnetic interactions takes place at high temperatures exhibiting the magnetically frustrated state. It leads to the formation of incommensurate sinusoidal AFM coupling along the *b*-axis below the Néel temperature. At still lower temperature, the system shows the formation of spiral spin structure in concurrence with the appearance of spontaneous electric polarization as a result of strong coupling between magnetization and electric po-

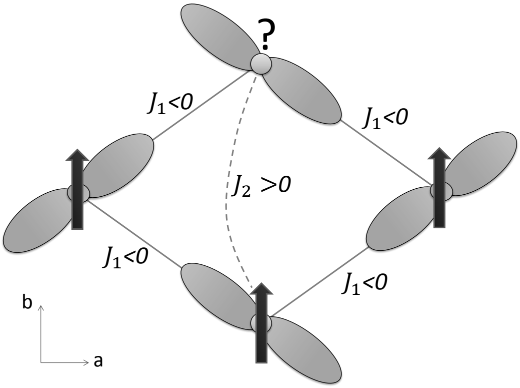

Figure 1.2: *The orbital configuration leading to spin frustration in distorted manganite.*

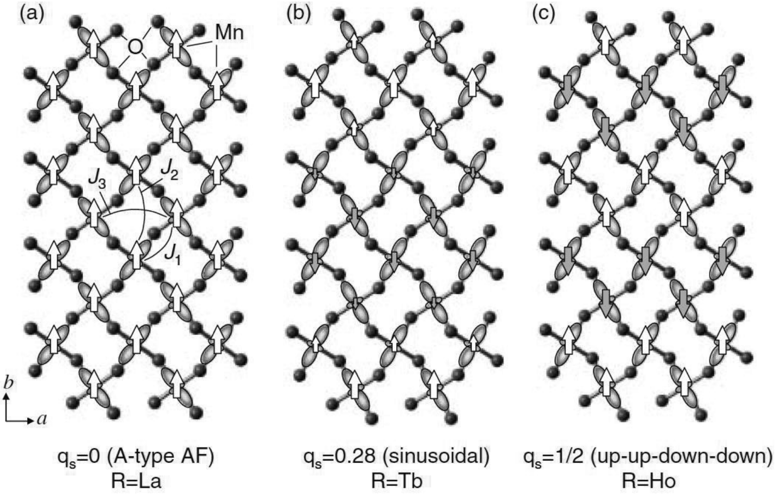

Figure 1.3: *(a) A-type, (b) sinusoidal, and (c) E-type antiferromagnetic interaction. Figures are adopted from [32].*

larization exhibiting the property of multiferroicity. In the compounds with small R radius such as $HoMnO_3$, the $GdFeO_3$-type distortions are very large so that the AFM interaction along the *b*-axis is stabilized resulting in the E-type AFM order at low temperatures.

Substituting the lanthanate trivalent metal with divalent metal induces changes in the relative number between Mn^{3+} and Mn^{4+}. Depending on the dopant concentration, the electron in the t_2g orbital of Mn^{3+} and Mn^{4+} may tend to couple antiferromagnetically due to superexchange interaction or ferromagnetically coupled due to double exchange interaction between Mn^{3+} and Mn^{4+}mediated by the mobile electon in e_g orbital. In general, the coexistence and competition between the FM and AFM coupling are expected in this magnetic system [34, 35] which produce complex magnetic structure that varies with temperature. At high temperatures, the system is paramagnetic with FM domains. As the temperature lowers, the AFM coupling becomes dominant and creates a 2D short range AFM order. Specifically, the magnetic ground state has been proposed as being a long range charge exchange (CE)-type AFM order below the Néel temperature (T_N), even though in some cases the system is rather known to be in the spin glass phase without a long-range spin order [35, 36]. Schematically, the spin configuration of CE-type AFM in the *ab*-plane is shown in Fig. 1.4. The spins are coupled ferromagnetically along zig zag chains and antiferromagnetically coupled between two adjacent chains.

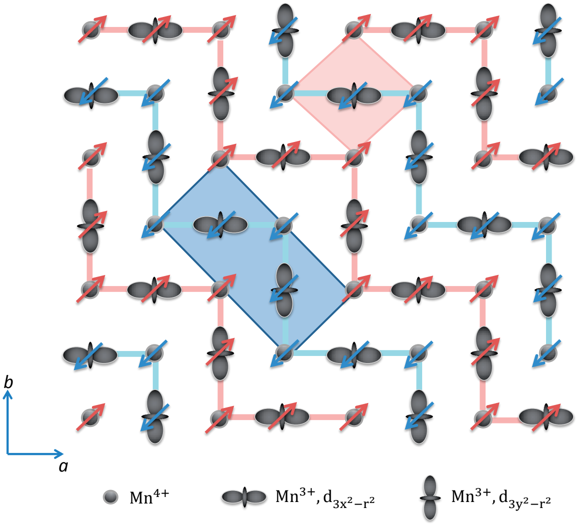

Figure 1.4: *The CE type spin structure in the ab-plane of alkali doped manganite. Red and blue shadows show the unit cells at the charge and orbital order phases.*

1.2 Charge, Orbital, and Spin Ordering

The half-doped manganite with the same concentration of Mn^{3+} and Mn^{4+} has special features. At high temperatures, the Mn^{3+} and Mn^{4+} are randomly arranged in a crystal structure. As the temperature is lowered, they could rearrange themselves to a charge order (CO) phase, as shown in Fig. 1.4. The onset of a CO is usually marked by the large step like increase of resistivity, which is a sign that the e_g electron is more localized and inter site hopping is suppressed. Experimentally, the stability of a CO is observed from the magnetic field dependent resistivity and magnetization measurements which suggest that the stability of CO is determined by the size mismatch between trivalent and divalent alkali metal [36, 37].

The CO is also closely related to the orbital order (OO) due arising from alternating electron occupancy of different d-orbitals Mn^{3+}. It is generally accepted that below OO transition, the $d_{3x^2-r^2}$ and $d_{3y^2-r^2}$ are alternately occupied and ordered, as shown in Fig. 1.4, even though a model of mixed orbital is also proposed [38, 39]. The OO is proposed to set in at the charge order transition. However, instead of a long range OO, the orbital domain state is also reported to be formed below the CO transition [40].

At low temperatures, the spins are generally ordered in various types of magnetic ground states as discussed in the previous section. In several cases, the spin orders (SO) are closely coupled with other degrees of freedom. For example, in a charge ordered system, the charge localization below the CO transition tends to destabilize the FM coupling which becomes dominated by the AFM coupling below the CO transition temperature leading to the formation of the CE-type AFM order below the Néel temperature. The coupling between spin and lattice is also observed in multiferroics and frustrated systems [8, 41, 42].

1.3 Optical Study

Optical spectroscopy offers a unique ability of selective excitation and the probing of the subsequent fast dynamical response arising from various types of coupling. It is expected to provide the rich information on the underlying physical mechanism, particularly the intricate coupling among the charge, spin, and lattice system in the material. This method has been widely used to elucidate the electronic structures and properties of materials. The optical properties of a material is usually expressed in terms of optical response functions such as dielectric functions, refractive index, absorption coefficient, and optical conductivity. Their physical origins cover a wide range of processes such as free electron absorption, interband transition, excitation from the core level, intersite transitions, and phonon assisted electronic transition. In a manganite system for instance, two distinct absorption spectra centered around 1.5 eV and above 3 eV have been assigned to the inter-site d-d transition and charge transfer p-d transition, respectively [15, 17, 43]. The orbital order [24, 44, 45] as well as the magnetic order [15, 46] have been shown to influence the optical spectra. The anisotropic optical spectra are observed along different crystallographic directions with different types of d-orbital orders [24, 45]. They are also strongly influenced by the onset of magnetic order [15]. Besides, the phase transitions are often related to the excitation of certain ordered phase with the excitation energy scaled by the strength of the associated interaction. In this case, optical spectroscopy has been used to observe the excitation of magnon [21] and the electromagnon (a hybridized magnon-phonon excitation) in multiferroic compounds [20, 47, 48].

Apart from probing the material properties, certain phase transitions can also be induced by light [49]. Optically induced phases may differ from any of the thermal equilibrium phases occurring in a material, and, moreover, may take place on a very fast sub-picosecond time scale. Ultrafast spectroscopy has the appropriate time resolution required to monitor the ultrafast transient processes and phase transformations in materials. It often offers information that is not accessible by experiments under equilibrium condition. In the following subsection, the phenomena observed by time- resolved pump probe spectroscopy and Raman spectroscopy are briefly described to give an overview of the physical mechanism that can be revealed by the two optical spectroscopies used in this thesis.

1.3.1 Time-resolved Pump Probe Spectroscopy

Time resolved spectroscopy is useful for observing the relaxation process of an excited system. The process is schematically described in Fig. 1.5. A very short pump pulse excites the system from the ground state into an excited state. The excited system might return immediately to the ground state or relax via several successive intermediate transient states. The excited state and the intermediate states often offer information about the electronic, magnetic, orbital, and lattice degrees of freedom, which are different from those found the equilibrium state. The information are usually extracted by probing tools that are relevant to certain characteristics of the transient states.

The time resolved spectroscopy provides a valuable tool to probe the dynamics of multiple degrees of freedom in materials having the charge, orbital, spin, and lattice degrees of freedom . In a system with charge ordering, time- resolved spectroscopy has been used to probe the temporal evolution of photo-induced charge order melting associated with insulator to metal transitions [24, 50, 51]. In a material with orbital orders, the uniform and staggered orbital configurations exhibit inequivalent optical responses so the photoinduced orbital disorder can be probed by observing the anisotropic changes of the transient reflectivity [24] or optical birefringence [52]. The effect of photoexcitation on the spin system has also been investigated, for example by time- resolved magneto optical Kerr spectroscopy, yielding information on the ultrafast spin dynamics during spin-lattice thermalization [53] and ferromagnetic phase formation due to charge-orbital order destruction [54]. A sensitive element probe using a tunable X-ray synchrotron source has also been deployed to monitor the photoinduced effects on orbital order [25], crystal structure [55], and magnetic system [56]. The X-ray probe is chosen in resonant with a certain energy corresponding to the excitation energy of each element in the system.

In a strongly correlated system, it is difficult to distinguish directly the con-

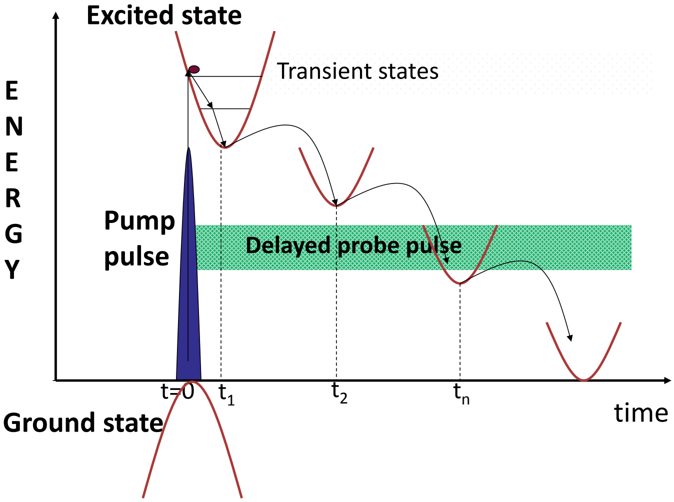

Figure 1.5: *Illustration of multiple stage of relaxation process of an excited system via several transient states.*

tribution of particular degree of freedom. One common approach to cope with this problem is to measure successive relaxation times related to the thermalization of each degree of freedom. The relaxation process of an excited system is generally conceived as an energy releasing process of an excited electron via successive channels involving lattice and spin degrees of freedom. Schematically, the multiple relaxation processes of an excited charge via lattice and spin systems are depicted in Fig. 1.6. The ultrafast pump pulse creates an excited electron with electron temperature T_e. The electron subsequently releases its energy to the lattice at certain lattice temperature T_l. The relaxation process occurs via electron-phonon interaction within a typical relaxation time τ_{el} which the lattice temperature will increase until the electron-lattice thermal equilibrium is reached. The typical length of τ_{el} is about 1 up to 10 ps. In manganite, the coupling between an excited electron and lattice can induce charge orbital disorder [54], JT distortion, structural change [55], and lattice expansion [25]. Further, the excited electron can also distribute its energy via the spin system. A theoretical study has shown that the relaxation rate is enhanced with increasing magnetic exchange integral [57]. The relaxation process of an excited system has also been connected to the annihilation and creation of a magnon. The magnon has been proposed as an effective decay channel for relaxation of the excited electron [57, 58]. In such a case, the relaxation process will increase the spin temperature and disturb the magnetic ordering. The change of temperature as well as the demagnetization process are usually treated in terms of three temperature regime involving the charge, lattice, and spin system [59]. The demagnetization process can directly occur via electron-spin interaction or indirectly via electron-lattice-spin interaction. In the case of manganite, a typical time for the direct process τ_{es} is less than 1 ps whereas the indirect process takes place with time duration τ_{ls} of ps up to ns [53, 60].

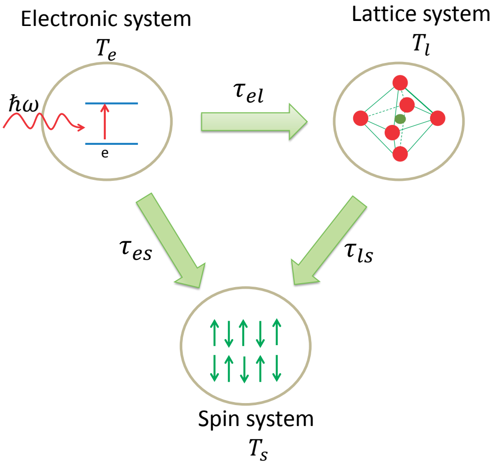

Figure 1.6: *The electronic relaxation via lattice and spin thermalization*

In this thesis, time -resolved pump probe spectroscopy is used to study the relaxation process of excited system in multiferroic compound TMO and a half-doped manganite layered system PCMO. In both cases, the excited electrons are generated by *p*-*d* charge transfer. The relaxation of excited electrons is probed by observing the transient reflectivity associated with the change of inter-site *d*-*d* transition. In the case of TMO, the relaxation of excited electrons is found to be strongly coupled to a magnetic sublattice. In PCMO, the strongest transient response is observed around CO transition temperature and is interpreted to induce lattice disorder.

1.3.2 Raman Spectroscopy

In Raman spectroscopy one observed the frequency up shift and downshift of the light scattered by the material. The shifts are classically associated with two sidebands resulted from the change of polarizability due to its modulation by periodic oscillation of the crystal lattice at its eigen frequency Ω. Quantum mechanically, the Stokes lines associated with the frequency down shift can be interpreted as the result of emission of a phonon from the electronic excited state in the photon scattering process, while the anti Stokes line related to frequency up shift is associated with the absorption of the phonon in the process. In a material having a magnetic structure, the photon-phonon scattering described above can also occur concurrently with phonon-magnon scattering. In short, Raman spectroscopy serves as a useful tool for probing the electronic, lattice, and magnetic structure as well as their related dynamical interplay. It should be noted that the phonons involved in Raman scattering are only the ones with momentum $q \approx 0$.

The active phonon or Raman modes can be predicted from the crystal symmetry using group theory. For this purpose, the scalar polarizability and atomic displacement are replaced by the susceptibility tensor and the normal coordinates, respectively. In certain geometries, the non-vanishing Raman modes are determined by the Raman tensors, which are defined as the derivatives of a susceptibility tensor with respect to the normal coordinates. The component of a Raman tensor depends on the nature of crystal symmetry and is represented by a 3 x 3 matrix. The particular Raman modes can be observed by properly choosing the polarizations of the incident and scattered lights. The intensity of the Raman mode is proportional to the square of the corresponding component of the Raman tensor.

Lattice dynamics plays an important role in determining the electronic and magnetic properties of manganite. Raman studies have revealed that the lattice dynamics has its origin in the Mn-O motions involving the cooperative dynamics of JT distortion, the tilting/bending mode of the MnO_6 octahedral, and the rotation of MnO_6 [61–64]. Raman modes at frequencies around 500 up to 700 cm^{-1} have been assigned as internal Mn-O bond stretching, which is strongly influenced by the occupation of the e_g orbital in the Mn^{3+} responsible for the occurrence of JT distortion. In addition, the size mismatches of the rare earth (RE) ion and divalent alkali metal (RA) ions from the Mn ion have been suggested to generate lower frequency modes related to MnO_6 octahedral bending and Mn-O-Mn tilting. Meanwhile the phonon modes around 400 cm^{-1} have been assigned to be bending modes [61, 64] whereas phonons around 200 cm^{-1} have been assigned to either Mn-O-Mn tilting modes [64] or MnO_6 octahedral rotation mode [61]. Other phonon modes lower than 200 cm^{-1} have been assigned to RE/RA-O vibrations [64]. The stretching modes are influenced by the Mn-O distances whereas the bending, tilting, and rotation modes are influenced by the Mn-O-Mn angles. Therefore information on the geometrical structure can be deduced from Raman spectrum.

In the doped manganite, the ordering of Mn^{3+} and Mn^{4+} also influences the Raman spectra. The CO order induces Mn^{3+}-O-Mn^{4+} bonds and breaks the symmetry of $Mn^{3.5}$-O-$Mn^{3.5}$ bonds. This subsequently modulates the lattice and appears as an anomaly of phonon evolution. Besides, the charge and orbital order might also induce doubling of unit cells, as indicated in Fig. 1.4. As a result, the CO and OO might also activate new Raman modes. In magnetic systems, the Raman spectra have been observed to have an anomalous behavior such as phonon frequency softening due to spin-phonon coupling associated with the modulation of lattice vibration by exchange integral. [47, 65].

A simple description of spin-lattice coupling is given in Fig. 1.7 (a), in which superexchange interaction is shown to trigger the spin lattice coupling. The exchange constant J depends on the metal-oxygen-metal distance and the oxygen-metal-oxygen angle therefore a shift of oxygen position relative to that of metal changes the amplitude of the superexchange constant. This situation is proposed to occur for example in manganite systems [8, 41] and kagomé lattice [42]. For those cases, the dependence of the exchange energy between two spins on the relative displacement of magnetic ions (δ_{ij}), is formulated in the following form:

$$E_{ij} = [J + (dJ/dr)\delta_{ij} + ...](S_i \bullet S_j) \tag{1.1}$$

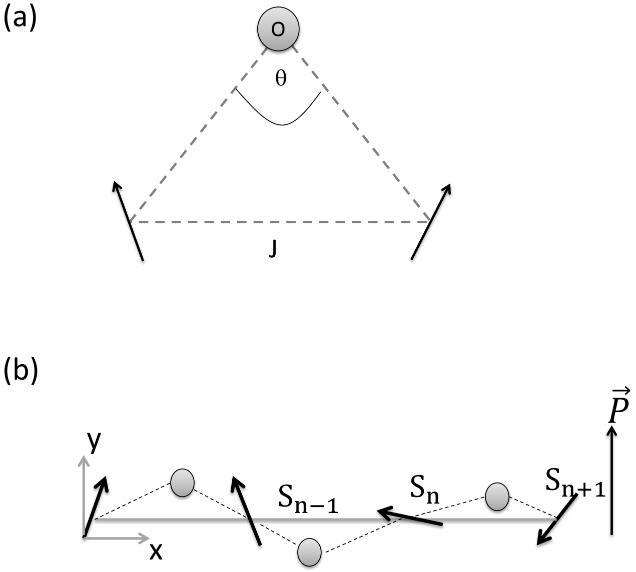

Figure 1.7: *(a) The illustration of spin lattice coupling in a system where the magnetic interaction is mediated by oxygen. (b) The oxygen shifts relative to magnetic ion positions and the associated electric polarization. Figures are adopted from [41].*

In a frustrated system, this coupling is expected to lift the magnetic degeneracy as the lattice distortion might favor exchange interaction along a certain spin pair over the others. In such a case, a certain magnetic order might occur at a finite temperature. The associated magnetic transition will be accompanied by the spontaneous breakdown of a lattice symmetry yielding a polar lattice. In the case of manganite, this spontaneous breakdown of lattice symmetry generates the appearance of spontaneous electric polarization resulting in multiferroicity. Figure 1.7 (b)) shows the direction of spontaneous electric polarization relative to the spin orientations and the shift of oxygen position relative to that of the magnetic ions. The electric polarization is $P \approx (Q \times e)$ where $\boldsymbol{Q}$ is the wave vector describing the spin propagation and $e = S_i \times S_j$ is the spin rotation axis [66]. This can also be understood in terms of antisymmetric Dzyaloshinskii -Moriya interaction (DMI) in the non-collinear spin structure [41]. The DMI is $D(r_n) = \vec{x} \times \vec{r_{12}}$, where $\vec{x}$ and $\vec{r_{12}}$ denoting the relative shift of oxygen position and a vector connecting the two neighboring spins, respectively. The electric polarization is then given by $P = D(r_n) \bullet (S_n \times S_{n+1})$. Therefore, the electric polarization increases with the increasing of the oxygen position shifts. Raman spectroscopy, in complement with infra red spectroscopy, has been used to observe the presence of electromagnon modes, which consist of the hybridization of phonon and magnon modes [67]. These modes have been proposed as the signature of multiferroicity.

1.4 Thesis overview

This thesis focuses on the study of correlations among the electronic, lattice, and magnetic degrees of freedom in manganite systems and iron jarosite compound as well as the roles they play in the appearance of the observed phenomena. The entire report is divided into six chapters and organized as follows

- Chapter 1 reviews the various types of magnetically competing systems that are found in manganites and iron jarosite. The phenomena of charge, orbital, and spin order are further described. In particular, the dynamical phenomena in manganite, usually observed by time resolved spectroscopy and Raman spectroscopy, are also discussed.

- Chapter 2 describes the experimental methods used in this study.

- Chapter 3 presents the results on charge dynamics in magnetically ordered phases and photoinduced electric polarization modulation in the multiferroic systems of TMO, which are studied by means of optical spectroscopy. A time resolved pump probe experiment was deployed to investigate the temperature dependence of transient reflectivity in TMO. The observed correlation between hopping conductivity and magnetic correlations is discussed. Additionally, Chapter III also presents the observed modulation of ferroelectric polarization in the multiferroics TMO studied by means of laser induced pyroelectric current modulation experiments.

- Chapter 4 reports the results of study on the phase transitions and their underlying physical mechanism in the half- doped layered manganite PCMO. The correlation between lattice dynamics and charge, orbital, and spin degrees of freedom are investigated by performing a temperature dependent experiment of Raman spectroscopy in combination with X-ray diffraction, magnetization, dc-transport, and specific heat measurement.

- Chapter 5 presents the photoinduced phenomena in PCMO whic are revealed and investigated by a time resolved pump probe experiment. Included in this chapter are the observation of photoinduced disorder domains, the role of spin assisted decay channel for excited carriers, and the photoinduced phase transition.

- Chapter 6 reports the magneto-electric and magneto-elastic coupling in iron jarosite system, which are observed by Raman spectroscopy.

Bibliography

[1] K. I. Kugel' and D. I. Khomskii. *Sov. Phys. Usp.*, 25:231, 1982.

[2] E. Dagotto. *Rev. Mod. Phys.*, 66:763, 1994.

[3] H. Kuwahara, Y. Tomioka, A. Asamitsu, Y. Moritomo, and Y. Tokura. *Science*, 270:961, 1995.

[4] M. Imada, A. Fujimori, and Y. Tokura. *Rev.Mod. Phys.*, 70:1039, 1998.

[5] Y Tokura and Y Tomioka. *Journal of Magnetism and Magnetic Materials*, 200:1, 1999.

[6] Y Tokura. *Rep. Prog. Phys.*, 69:797, 2006.

[7] T. Kimura. *Ann. Rev. Mater. Res.*, 37:387, 2007.

[8] S W Cheong and M Motovoy. *Nature*, 6:13, 2007.

[9] D. Khomskii. *Physics*, 2:20, 2009.

[10] T. P. Devereaux and R. Hackl. *Rev. Mod. Phys.*, 79:175, 2007.

[11] J. P. Carbotte, E. Schachinger, and D. N. Basov. *Nature*, 401:354, 1999.

[12] J. T. Stewart, J. P. Gaebler, and D. S. Jin. *Nature*, 454:744.

[13] W. Z. Hu, J. Dong, G. Li, Z. Li, P. Zheng, G. F. Chen, J. L. Luo, and N. L. Wang. *Phys. Rev. Lett.*, 101:257005, 2008.

[14] B. Friedl, C. Thomsen, and M. Cardona. *Phys. Rev. Lett.*, 65:915, 1990.

[15] N. N. Kovaleva, A. V. Boris, C. Bernhard, A. Kulakov, A. Pimenov, A. M. Balbashov, G. Khaliullin, and B. Keimer. *Phys. Rev. Lett.*, 93:147204, 2004.

[16] Y. S. Lee, T. Arima, S. Onoda, Y. Okimoto, Y. Tokunaga, R. Mathieu, X. Z. Yu, J. P. He, Y. Kaneko, Y. Matsui, N. Nagaosa, and Y. Tokura. *Phys. Rev. B*, 75:144407, 2007.

[17] A. S. Moskvin, A. A. Makhnev, L. V. Nomerovannaya, N. N. Loshkareva, and A. M. Balbashov. *Phys. Rev. B*, 82:035106, 2010.

[18] A. Rusydi, R. Rauer, G. Neuber, M. Bastjan, I. Mahns, S. Müller, P. Saichu, B. Schulz, S. G. Singer, A. I. Lichtenstein, D. Qi, X. Gao, X. Yu, A. T. S. Wee, G. Stryganyuk, K. Dörr, G. A. Sawatzky, S. L. Cooper, and M. Rübhausen. *Phys. Rev. B*, 78:125110, 2008.

[19] R. Valdés Aguilar, A. B. Sushkov, S. Park, S.-W. Cheong, and H. D. Drew. *Phys. Rev. B*, 74:184404, 2006.

[20] R. Valdés Aguilar, M. Mostovoy, A. B. Sushkov, C. L. Zhang, Y. J. Choi, S-W. Cheong, and H. D. Drew. *Phys. Rev. Lett.*, 102:047203, 2009.

[21] A. Pimenov, A. Shuvaev, A. Loidl, F. Schrettle, A. A. Mukhin, V. D. Travkin, V. Yu. Ivanov, and A. M. Balbashov. *Phys. Rev. Lett.*, 102:107203, 2009.

[22] E. Granado, A. Garc´, J. A. Sanjurjo, C. Rettori, I. Torriani, F. Prado, R. D. Sánchez, A. Caneiro, and S. B. Oseroff. *Phys. Rev. B*, 60:11879, 1999.

[23] J. Laverdière, S. Jandl, A. A. Mukhin, V. Yu. Ivanov, V. G. Ivanov, and M. N. Iliev. *Phys. Rev. B*, 73:214301, 2006.

[24] T. Ogasawara, T. Kimura, T. Ishikawa, M. Kuwata-Gonokami, and Y. Tokura. *Phys. Rev. B*, 63:113105, 2001.

[25] H. Ichikawa, S. Nozawa, T. Sato, A. Tomita, K. Ichiyanagi, M. Chollet, L. Guerin, N. Dean, A. Cavalleri, S. Adachi, T. Arima, H. Sawa, Y. Ogimoto, M. Nakamura, R. Tamaki, K. Miyano, and S. Koshihara. *Nat.Mater.*, 10:101, 2011.

[26] R. Moessner and A.P. Ramirez. *Physics Today*, 81:24, 2006.

[27] J.-S. Zhou and J. B. Goodenough. *Phys. Rev. Lett.*, 96:247202, 2006.

[28] Steven T. Bramwell and Michel J. P. Gingras. *Science*, 294:1495, 2001.

[29] John E. Greedan. *J. Mater. Chem.*, 11:37, 2001.

[30] John E. Greedan. *Journal of Alloys and Compounds*, 408:444, 2006.

[31] M. Elhajal, B. Canals, and C. Lacroix. *Phys. Rev. B*, 66:014422, 2002.

[32] R. Kajimoto, H. Mochizuki, H. Yoshizawa, H. Shintani, T. Kimura, and Y. Tokura. *J. Phys. Soc. Japan*, 74:2430, 2005.

[33] T. Kimura, S. Ishihara, H. Shintani, T. Arima, K. T. Takahashi, K. Ishizaka, and Y. Tokura. *Phys. Rev. B*, 68:060403, 2003.

[34] F. Millange, S. de Brion, and G. Chouteau. *Phys. Rev. B*, 62:5619, 2000.

[35] D. Senff, N. Aliouane, D.N. Argyriou, A. Hiess, L.P. Regnault, P. Link, Sidis Y. Hradil, K., and M. Braden. *Journal of Physics - Condensed Matter*, 20:434212, 2008.

[36] R. Mathieu, M. Uchida, Y. Kaneko, J. P. He, X. Z. Yu, R. Kumai, T. Arima, Y. Tomioka, A. Asamitsu, Y. Matsui, and Y. Tokura. *Phys. Rev. B*, 74:020404, 2006.

[37] Y. Tomioka and Y. Tokura. *Phys. Rev. B*, 70:014432, 2004.

[38] D. J. Huang, W. B. Wu, G. Y. Guo, H.-J. Lin, T. Y. Hou, C. F. Chang, C. T. Chen, A. Fujimori, T. Kimura, H. B. Huang, A. Tanaka, and T. Jo. *Phys. Rev. Lett.*, 92:087202, 2004.

[39] V. Capogrosso, M. Malvestuto, I. P. Handayani, P. H. M. van Loosdrecht, A. A. Nugroho, and E. Magnanoand F. Parmigiani. *Phys. Rev. B*, 87:155118, 2013.

[40] M. v. Zimmermann, J. P. Hill, Doon Gibbs, M. Blume, D. Casa, B. Keimer, Y. Murakami, Y. Tomioka, and Y. Tokura. *Phys. Rev. Lett.*, 83:4872, 1999.

[41] I. A. Sergienko and E. Dagotto. *Phys. Rev. B*, 73:094434, 2006.

[42] Kris T. Delaney, Maxim Mostovoy, and Nicola A. Spaldin. *Phys. Rev. Lett.*, 102:157203, 2009.

[43] M. W. Kim, S. J. Moon, J. H. Jung, Jaejun Yu, Sachin Parashar, P. Murugavel, J. H. Lee, and T. W. Noh. *Phys. Rev. Lett.*, 96:247205, 2006.

[44] M. W. Kim, S. J. Moon, J. H. Jung, Jaejun Yu, Sachin Parashar, P. Murugavel, J. H. Lee, and T. W. Noh. *Phys. Rev. Lett.*, 96:247205, 2006.

[45] K. Tobe, T. Kimura, and Y. Tokura. *Phys. Rev. B*, 69:014407, 2004.

[46] M. Bastjan, S. G. Singer, G. Neuber, S. Eller, N. Aliouane, D. N. Argyriou, SL Cooper, and M. Rübhausen. *Phys. Rev. B*, 77:193105, 2008.

[47] H. Barath, M. Kim, S. L. Cooper, P. Abbamonte, E. Fradkin, I. Mahns, M. Rübhausen, N. Aliouane, and D. N. Argyriou. *Phys. Rev. B*, 78:134407, 2008.

[48] A. Pimenov, A. A. Mukhin, V. Yu. Ivanov, V. D. Travkin, A. M. Balbashov, and A. Loidl. *Nat Phys*, 2:97, 2006.

[49] K. Nasu. *Photoinduced Phase Transitions.* World Scientific, 2004.

[50] K. Miyano, T. Tanaka, Y. Tomioka, and Y. Tokura. *Phys. Rev. Lett.*, 78:4257, 1997.

[51] M. Fiebig, K. Miyano, Y. Tomioka, and Y. Tokura. *Appl. Phys. B*, 71:211, 2000.

[52] R. Singla, A. Simoncig, M. Först, D. Prabhakaran, A. L. Cavalieri, and A. Cavalleri. *Phys. Rev. B*, 88:075107, 2013.

[53] T. Ogasawara, K. Ohgushi, Y. Tomioka, K. S. Takahashi, H. Okamoto, M. Kawasaki, and Y. Tokura. *Phys. Rev. Lett.*, 94:087202, 2005.

[54] M. Matsubara, Y. Okimoto, T. Ogasawara, Y. Tomioka, H. Okamoto, and Y. Tokura. *Phys. Rev. Lett.*, 99:207401, 2007.

[55] P. Beaud, S. L. Johnson, E. Vorobeva, U. Staub, R. A. De Souza, C. J. Milne, Q. X. Jia, and G. Ingold. *Phys. Rev. Lett.*, 103:155702, 2009.

[56] H. Ehrke, R. I. Tobey, S. Wall, S. A. Cavill, M. Först, V. Khanna, Th. Garl, N. Stojanovic, D. Prabhakaran, A. T. Boothroyd, M. Gensch, A. Mirone, P. Reutler, A. Revcolevschi, S. S. Dhesi, and A. Cavalleri. *Phys. Rev. Lett.*, 106:217401, 2011.

[57] Z. Lenarčič and P. Prelovšek. *Phys. Rev. Lett.*, 111:016401, 2013.

[58] S. F. Zhang. *Journal of Applied Physics*, 79:4542, 1996.

[59] E. Beaurepaire, J-C. Merle, A. Daunois, and J-Y. Bigot. *Phys. Rev. Lett.*, 76:4250, 1999.

[60] A. I. Lobad, R. D. Averitt, C. Kwon, and A. J. Taylor. *Applied Physics Letters*, 77:4025, 2000.

[61] M. N. Iliev, M. V. Abrashev, H.-G. Lee, V. N. Popov, Y. Y. Sun, C. Thomsen, R. L. Meng, and C. W. Chu. *Phys. Rev. B*, 57:2872, 1998.

[62] K. Yamamoto, T. Kimura, T. Ishikawa, T. Katsufuji, and Y. Tokura. *Phys. Rev. B*, 61:14706, 2000.

[63] M. V. Abrashev, J. Bäckström, L. Börjesson, M. Pissas, N. Kolev, and M. N. Iliev. *Phys. Rev. B*, 64:144429, 2001.

[64] L. Martin-Carron, A. de Andrés, M. J. Martinez-Lope, M. T. Casais, and J. A. Alonso. *Phys. Rev. B*, 66:174303, 2002.

[65] E. Granado, A. Garc´, J. A. Sanjurjo, C. Rettori, I. Torriani, F. Prado, R. D. Sánchez, A. Caneiro, and S. B. Oseroff. *Phys. Rev. B*, 60:11879, 1999.

[66] M. Mostovoy. *Phys. Rev. Lett.*, 96:067601, 2006.

[67] P. Rovillain, M. Cazayous, Y. Gallais, A. Sacuto, M-A. Measson, and H. Sakata. *Phys. Rev. B*, 81:054428, 2010.

Chapter 2

Experimental Methods

This chapter describes the experimental techniques and instruments used for the studies reported in this thesis. The optical techniques deployed in this work consist of two part. The first one is the time resolved pump probe spectroscopy which is used for the study of dynamical properties of the excited systems. The second part is the Raman spectroscopy employed in the study of the lattice dynamics. The structural characterization of the sample is performed by X-ray diffraction to extract information of crystallographic structure while magnetization measurement is conducted to characterize the magnetic properties. The entropy change at phase transition is determined by measuring the corresponding change of temperature dependent specific heat and the resistivity measurements is performed to characterize the charge transport.

2.1 Time Resolved Pump Probe Spectroscopy

The setup of time resolved pump probe experiment is given in Fig. 2.1. A Ti-sapphire laser (Hurricane, Spectra Physics) was utilized to generate short (<200 fs) pulses with central wavelength 800 nm and a 1 kHz repetition rate. The beam was split into pump and probe beam using beam splitter. The pump light went to delay line and a 400 nm pump beam was subsequently generated via second harmonic generation using BBO crystal. Both pump and probe beam were spatially and temporally overlapped in the sample which was mounted inside Janis cryostat. The system was excited by the pump beam while the transient response was measured by detecting the reflectivity of probe beam. The polarization of the incoming probe beam was aligned at 45^0 with respect to the certain crystallographic axis and a Wollaston prims was used to analyze the reflected probe beam polarization. With this configuration, the two reflected beam with mutually orthogonal polarization can be detected simultaneously by Si-photodetectors which connected to the SR-830 lockin amplifier with bandpass filters were placed in front of the detectors to ensure that only 800 nm probe beams entered the detectors.

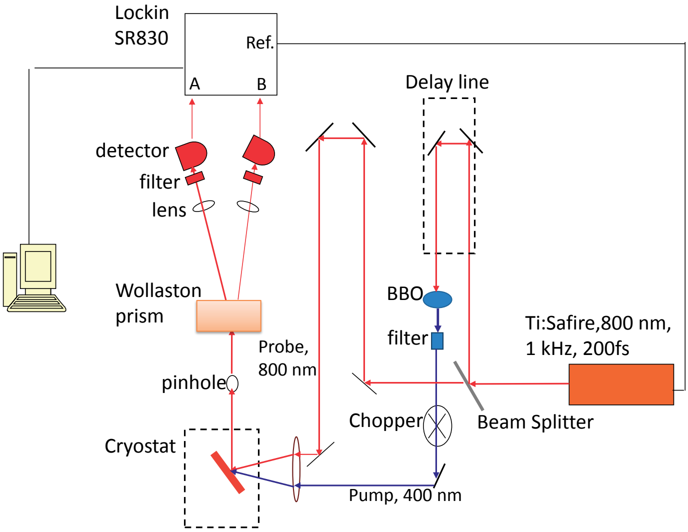

Figure 2.1: *Schematic description of time resolved pump probe spectroscopy setup.*

2.2 Raman Spectroscopy

The schematic diagram of Raman experiment setup is shown in Fig. 2.2 (a). The setup consists of a laser, mirrors, polarizer, optical confocal microscope with triple grating spectrometer (Jobin Yvon T64000), cryostat, CCD detector, and Labspec software. A 532 nm continuous wave generated by Nd:YO$_4$ laser was used as excitation source in Pr$_{0.5}$Ca$_{1.5}$MnO$_4$ study while 676.4 nm line from Kr$^+$ laser was used in studying the KFe$_3$(OH)$_6$(SO$_4$)$_2$. Mirrors direct the laser beam to the optical confocal microscope. The schematic diagram of confocal microscope is presented in Fig. 2.2 (b). It consists of spatial filter, beamsplitter, objective lens, and a pinhole. The spatial filter was placed before beamsplitter to ensure a Gaussian beam profile. The beamsplitter transmits only 20 % of perpendicular polarized light and 40 % of parallel polarized light. The objective lens focuses the beam on the sample which was mounted in the continuous flow cold finger cryostat. The backscattered light is focussed to the confocal pinhole, ensuring that only light originating from the sample enters the spectrometer.

The next part was the triple spectrometer which contained three gratings (1800 gr/mm). The backscattering light which came from the pinhole was polychromatic. It passed the entrance slit S$_1$ and was dispersed by grating 1. The entrance slit was open at 100 μm. The intermediate slit 1, which was open at 2 cm, selected a bandpass in the range of λ_1 and λ_2. The grating 2 recombined the dispersed beam to a polychromatic beams but only in the range of λ_1 and λ_2. This polychromatic beam was dispersed once more by the grating 3. Here, the spectral range detected by CCD detector was selected. All processes are schematically described in Fig. 2.2 (c). The whole spectra were recorded by using multiwindows acquisition which moved the gratings simultaneously to different positions for different ranges of frequency.

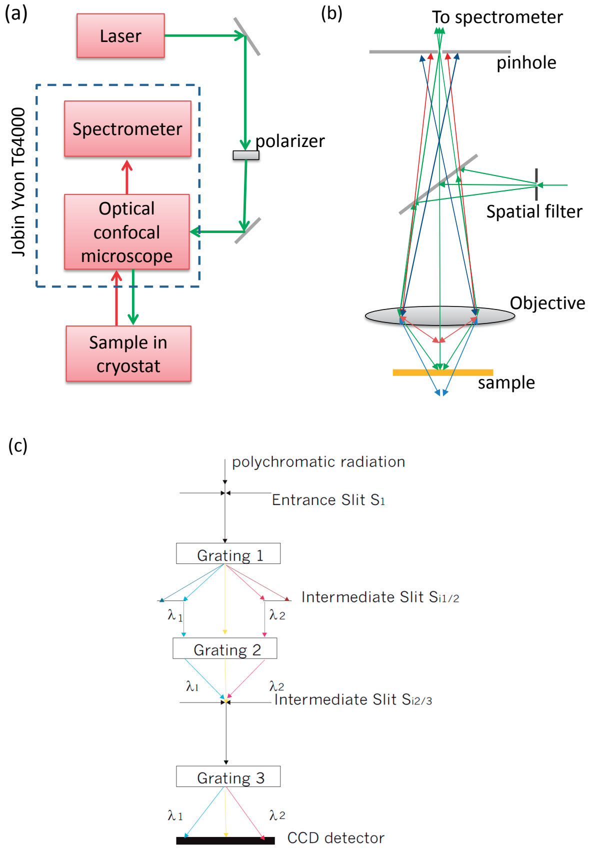

Figure 2.2: *(a) Schematic diagram of Raman experimental setup. (b) The optical confocal microscope. Only beams scattered by sample pass the pinhole and go to spectrometer. (c). Schematic diagram of triple grating spectrometer.*

To study the lattice dynamics and analyze the origin of lattice dynamics, polarized Raman measurements were done by selecting the polarization of incoming and scattered beams. In this thesis, polarization configuration is written based on the Porto notation. For example the $c(ba)\bar{c}$ means the incoming beam is polarized along b-axis and propagates along c-axis while the scattered beam is polarized along a-axis and propagates along -c-axis.

2.3 X-Ray Diffraction Measurement

X-ray diffraction measurement was carried out to characterize the crystallographic structure of material. The basic configuration of measurement is given in Fig. 2.3. The measurements were done using Bruker D8, Huber G670, and Enraf-Nonius CAD4 diffractometer facilities in Solid State Material for Electronic Group, Zernike Institute for Advanced Materials, University of Groningen.

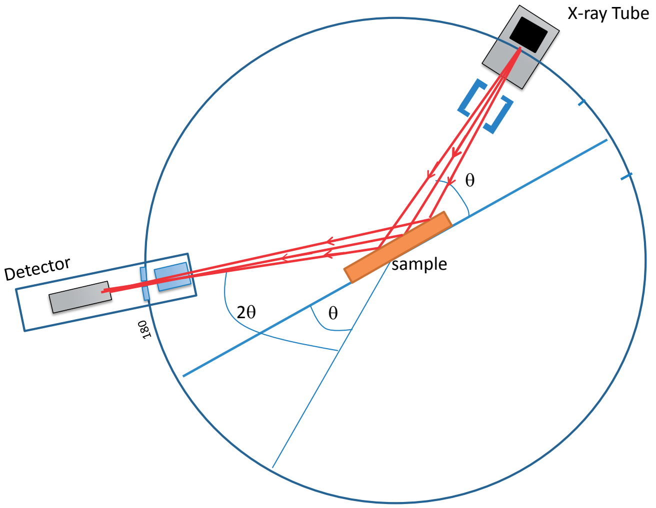

Figure 2.3: *Basic configuration of X-ray diffractometer.*

The Bruker D8 diffractometer was used to observe X-ray diffraction on powder sample from 298 K up to 343 K. The machine operates based on Bragg Brentano geometry with Cu K_α radiation source and energy dispersive solid state detector. The powder sample was placed in a rotating sample holder. The diffraction angle (2Θ) can be varied from 0 up to 100^0 with interval 0.02^0. The Huber G670 diffractometer was used to observed X-ray diffraction on powder sample from 298 K down to 20 K. The machine had Cu and Mo K_α radiation sources and G670 Gruiner camera which detected the transmitted X-ray beam after passing the sample. A closed cycle refrigerator system supplied by Helix Technology Corporation was used for low temperature measurement. The powder sample was placed in thin fiber mounted in rotating holder. The diffraction angle (2Θ) can be varied from 0 up to 100^0 with interval 0.005^0. The Enraf-Nonius CAD4 diffractometer were used to orient the single crystal axes. The machine has Mo radiation source and scintillation detector which detected the reflected X-ray beam. A very small-thin sample was mounted on top of rotating sample holder to minimize X-ray absorption. 25 reflected X-ray light from sample were usually sufficient enough to determine the crystal axes.

The X-ray diffraction on $TbMnO_3$ was carried out by N. Mufti on crushed single crystal using Huber G670 diffractometer with Mo radiation source. The obtained lattice parameters are presented in Fig.3.4 chapter 3. The $Pr_{0.5}Ca_{1.5}MnO_4$ structure was characterized by performing powder X-ray diffraction on crushed single crystal using Bruker D8 diffractometer and Huber G670 diffractometer. Both measurements used Cu K_α radiation source. The temperature was varied from 20 K up to 343 K. Those measurements were done in collaboration with S. Riyadi and G. Blake. The obtained spectra were analyzed using General Structure Analysis System (GSAS) software package with EXPGUI interface [1]. The result are presented in Fig. 4.4-4.7 chapter 4. The XRD measurement on $KFe_3(OH)_6(SO_4)_2$ was done by J. Buurma at room temperature.

2.4 Magnetization Measurement

Magnetization measurement was performed using Quantum Design Magnetic Properties Measurement System (MPMS) XL7 Magnetometer which the basic configuration is described in Fig.2.4. The main part of the machine consisted of a superconducting magnet, a superconducting detection coil (pick up coil), a superconducting quantum interface device (SQUID) , and a superconducting magnetic shield. The superconducting magnet was able to produce magnetic field up to 7 T which was used to influence the magnetic moment of the sample. The observed magnetic response from the sample, which was proportional to the sample magnetic moment, was detected by pick-up coil and connected to SQUID which acted as magnetic flux to voltage converter. An alternating voltage was produced when the sample was moved up and down. This alternating voltage was amplified and was read out by the electronic part of the device which was automatic controlled using LabView program. It had sensitivity to detect magnetic moment down to 10^{-7} emu. The MPMS XL 7 was equipped by temperature controlling system which was able to operate from 2 up to 400 K. During measurement process, the sample was placed inside a gelatin capsule together with some cottons to avoid sample movement. The gelatin capsule was then inserted into straw and attached to MPMS probe.

The magnetization of $TbMnO_3$ was carried out by N. Mufti. The results are presented in Fig.3.5 chapter 3. The magnetization of $Pr_{0.5}Ca_{1.5}MnO_4$ was observed from temperature 4 K up to 340 K. The results are presented in Fig.4.8 chapter 4. The magnetization of $KFe_3(OH)_6(SO_4)_2$ was carried out by J. Buurma. The result is presented in Fig. 6.2 chapter 6.

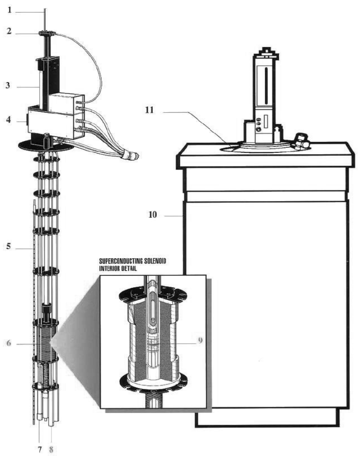

1. Sample rod
2. Sample rotator
3. Sample transport
4. Probe assembly
5. Helium level sensor
6. Superconducting selenoid

7. Flow impedance
8. SQUID capsule with magnetic shield
9. Superconducting pick up coil
10. Dewar isolation system
11. Dewar

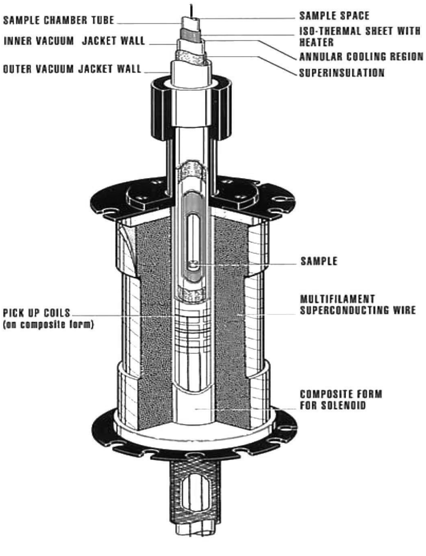

Figure 2.4: *Basic configuration of MPMS. Figure is adopted from [2].*

2.5 Heat Capacity Measurement

The temperature dependence of heat capacity was measured using a Quantum Design 9T physical property measurement system (PPMS). The setup configuration is described in Fig. 2.5. The sample was mounted on the microcalorimeter platform using Apiezon N grease. The temperature was varied from 5 up to 340 K with interval 5 K. The machine was able to perform automated relaxation heat capacity measurement. Each measurement was automatically analyzed with two-tau model which simulated the heat flow from the microcalorimeter platform to the sample as well as from the platform to the puck stage. The machine was also equipped by built-in data subtraction feature which removed automatically the heat capacity background arise from the adhesive and sample platform contribution. This measurement was performed by N. Mufti in Max Planck Institute for Chemical Physics of Solids, Dresden, Germany.

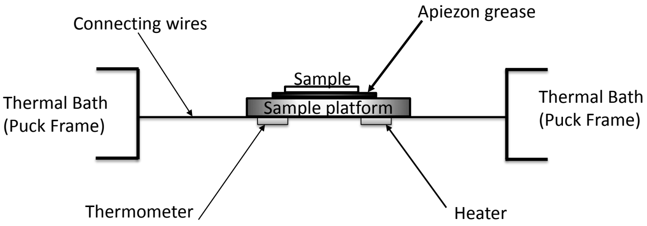

Figure 2.5: *Configuration setup of heat capacity measurement.*

2.6 Resistivity Measurement

The temperature dependence of resistivity measurement was carried out using four probe method in which four electrical contacts were made from $\approx$ 1 mm^2 silver paste droplets deposited in an array along the a axis with a 1 mm interval. Platinum wires were used to connect these silver paste electrodes to the terminal of a chip-carrier which was mounted on the cold finger of a He flow cryostat. The temperature was varied from 340 K to 100 K . The I-V measurement was carried out using a Keithley 237 source-measure unit. The measurement was done by varying voltages and measuring currents. The resistance of the sample is determined by taking the slope of I-V curve.

Bibliography

[1] A. C. Larson and R. B. von Dreele. *General Structure Analysis System (GSAS)*. Los Alamos National Laboratory Report LAUR, 2004.

[2] M. McElfresh. *Fundamental of Magnetism and Magnetic Measurements: Featuring Quantum Design's Magnetic Properties Measurement System.* Purdue University, 1994.

Chapter 3

Dynamics of Photo-excited Electrons and Optically Modulation Of Electric Polarization in $\mathrm{TbMnO_3}$

3.1 Introduction

The physical properties of *3d* transition metal oxides result from an intricate interplays among the lattice, charge, orbital, and spin. The manganite oxides, the $\mathrm{RMnO_3}$ series with R = rare earth, for example, are know to exhibit a variety of ordered phases of charges, orbitals, and spins states [1], which are responsible for the observed properties ranging from colossal magneto-resistive phenomena [2] to multiferroicity [3]. A size mismatch between the rare earth ion and the 'free space' in the pseudocubic unit cell induces a $\mathrm{GdFeO_3}$ type distortion of the $\mathrm{MnO_6}$ octahedral, leading to a highly distorted orthorhombic structure. In addition, the Jahn-Teller (JT) active $\mathrm{Mn^{3+}}$ ion induces a further distortion of the $\mathrm{MnO_6}$ octahedral causing different lengths of the Mn-O bonds and a splitting of e_g orbitals.

Figure 3.1 (a) shows a typical arrangement of e_g orbital occupation in $\mathrm{RMnO_3}$. The filling of the $d_{3x^2-r^2}$ and $d_{3y^2-r^2}$ (red orbitals) forms a checkerboard pattern in the *ab*-planes while the stacking is parallel along the c-axis. The unoccupied orbitals ($d_{3x^2-z^2}$ and $d_{3y^2-z^2}$) are shown by blue color. An optical study [5], however, has shown that there is some degree of hybridization between the $d_{3x^2-y^2}$ and $d_{3z^2-r^2}$ orbitals.

Figure 3.1 (b) shows the phase diagram of $\mathrm{RMnO_3}$, showing both JT transition temperatures and the different types of magnetic ordering for various rare earth ions in the compounds. Two different types of magnetic ordering, E-type and A-type antiferomagnetic ordering (AFM) , are schematically presented. The JT distortion occurs more easily for $\mathrm{RMnO_3}$ with smaller radius rare earth ions leading to a higher JT transition temperature. The type of magnetic ordering also depends on the size of the rare earth ion. For rare earth ions with a radius exceeding 1.11 Å, an A type AFM is realized while it is E type AFM for radii smaller 1.07 Å. In the intermediate case, i.e. for Tb and Dy, a sinusoidal AFM ordering is formed below

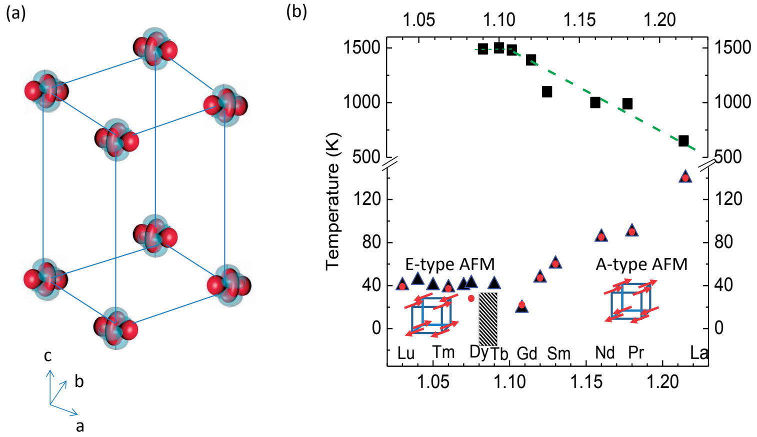

Figure 3.1: *(a) The e_g-orbital arrangement in $RMnO_3$. Red and blue colors indicate the occupied and unoccupied orbitals, respectively. (b) Phase diagram of $RMnO_3$ as a function of rare earth ion radius indicating JT transition temperatures (black squares), magnetic ordering temperatures (blue triangle), and temperatures where anomalous of conductivity occurs (red circles). Figure is modified from Ref.[4]*

the Néel temperature (T_N) and spiral spin structure occurs below a transition temperature T_c. Shaded area in Fig. 3.1 (b) shows the phase existence region for this anomalous magnetic ordering.

The MnO_6 octahedral configuration and the splitting of d-orbitals are shown in Fig. 3.2. The octahedra consists of an Mn ion in the center, four oxygen ions square coordinated in the basal plane, and two oxygen ions at the apical direction. The outer electrons of the Mn ion occupy the d-orbitals. In a free Mn ion, the energy levels of d-orbitals are degenerated. The presence of oxygen ions in the octahedral cage induces crystal field splitting so that five fold degenerate d-orbitals split into higher energy e_g orbitals and lower energy t_{2g} orbitals. Three electrons fill the lower energy t_{2g} orbitals while one electron is in a higher energy e_g orbital. A Jahn Teller (JT) distortion deforms the MnO_6 octahedra and creates the elongation or shortening of Mn-O bonds. Figure 3.2 shows an example of elongation along the apical direction. This JT distortion splits the e_g orbital into $d_{z^2-r^2}$ and $d_{x^2-y^2}$ as well as the t_{2g} into d_{xy}, d_{xz}, and d_{yz}. Due to Hund's rule, the four electrons of the Mn^{3+} ion tend to be aligned in parallel and form a ferromagnetic (FM) configuration.

$TbMnO_3$ is one of the most widely studied member of the $RMnO_3$ family. The interest in this compound derives from its complex magnetic structure which in the low temperature phase is accompanied by a magnetically driven spontaneous ferroelectric polarization [6]. The MnO_6 octahedra in $TbMnO_3$ is known to be tilted as shown in Fig.3.3 [7]. It has one apical Mn-O bond along the c-axis with a bond length of 1.946(1) Å and two equatorial bonds in ab-plane with long bond

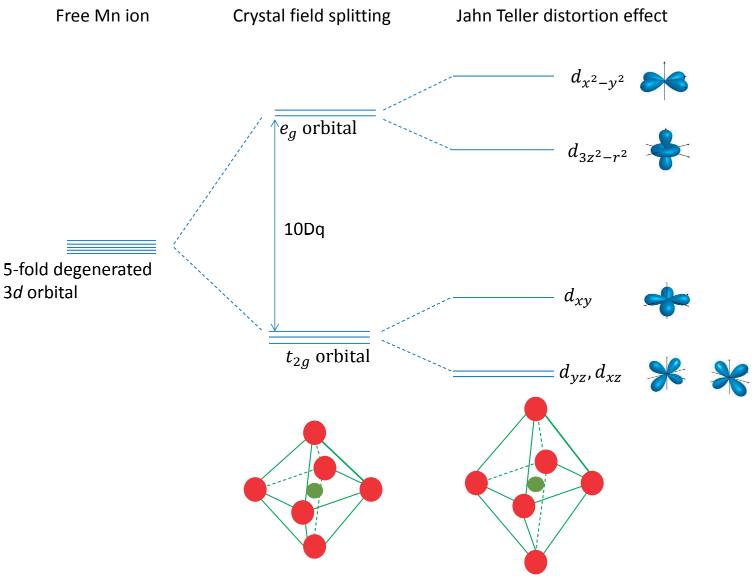

Figure 3.2: *The JT energy splitting and electron occupation in d-orbital of Mn*

length of 2.234(4) Å and short bond length of 1.8894(4) Å. The Mn-O-Mn angle in ab-plane is about 145^0. The short and long Mn-O bonds alternate in the ab-plane.

The Mn spins interact via Mn-O-Mn superexchange interaction. The orbital order of $d_{3x^2-r^2}$ and $d_{3y^2-r^2}$ generates $e_g^1 - O - e_g^0$ ferromagnetic (FM) interaction in the ab-plane whereas $e_g^1 - O - e_g^1$ antiferromagnetic (AFM) coupling exists along c-axis. The small atomic radius of Tb^{3+} ion distorts the cubic perovskite structure giving rise to the highly distorted $GdFeO_3$-type lattice of the orthorhombic structure. Together with the JT induced anisotropic distortion of the Mn-O bond lengths, the $GdFeO_3$ tilting leads to a weakening of the FM and strengthening of the AFM interaction along the b-axis. This leads to frustration of the manganese spin degree of freedom due to strong competition between FM coupling of nearest neighbor (NN) magnetic interactions and AFM coupling of next nearest neighbor (NNN) magnetic interactions [9]. As a consequence, a sinusoidal AFM spin structure is formed along the b direction at the Néel temperature, $T_{N,1}$=41 K. Below $T_{N,2}$=26 K, the magnetic structure changes to a bc-cycloid with the simultaneous appearance of the spontaneous electric polarization along the c-axis [10, 11]. The sinusoidal AFM and spiral spin structures are shown in Fig. 3.3 (b).

This chapter reports the results of our study on $TbMnO_3$. The sample growth and characterization are reviewed in section 3.2 which explains the structural, magnetization, and ferroelectric properties of the material used in our experiment. Section 3.3 reviews the optical properties of $TbMnO_3$. The result of dynamical study of photoexcited electrons is reported in section 3.4. For this study, the cou-

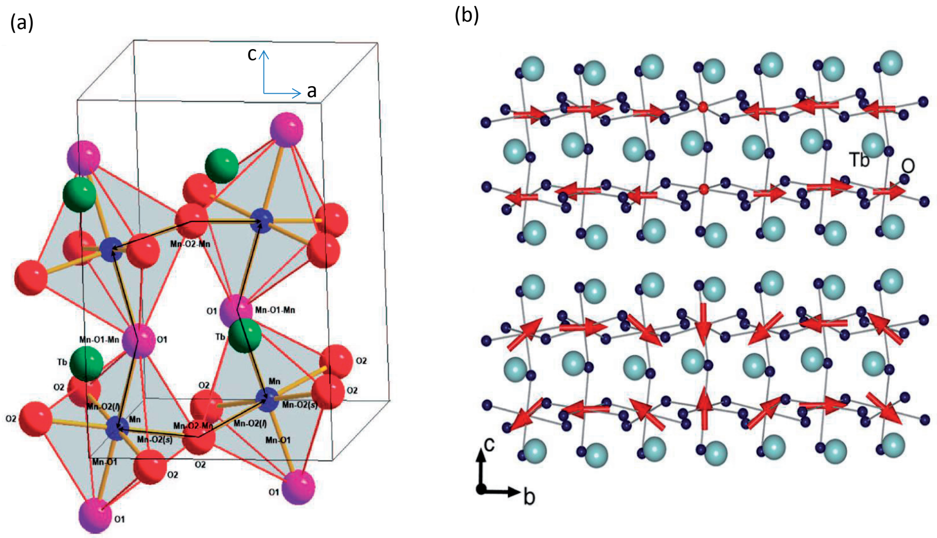

Figure 3.3: *(a) The MnO6 octahedral tilting of* $TbMnO_3$ *[7](b) The sinusoidal AFM spin structure below 41 K (upper panel) and the spiral spin structure below 26 K (lower panel) [8]*

pling of charge (hopping) transport with magnetic order is investigated by probing the dynamics and relaxation processes of the excited material across the magnetic phase transitions. Section 3.5 gives the results of photoinduced polarization modulation experiments. Finally, section 3.6 summarizes the conclusions drawn from our experiments.

3.2 Material Characterizations

The material chosen for our experiment is the multiferroic $TbMnO_3$ compound. It was grown using a traveling solvent floating zone method utilizing a four mirror furnace (Crystal System Corp., FZT-10000-H-VI-VP). Here, we briefly review the structure, magnetic, and ferroelectric properties of our sample as previously reported by N. Mufti [12].

The crystal structure was characterized by X-ray powder diffraction which shows that the sample is a single crystal with orthorhombic unit cell having Pbnm space group. The lattice parameters at room temperature are a = 5.29969(9) Å, b = 5.84236(9) Å, and c = 7.40147(12) Å. The temperature dependent variations of the lattice parameters are shown in Fig. 3.4. The lattice parameters are anisotropic below 60 K with a clear visible changes at 26 K. Along the a-axis, the lattice constant increases almost linearly with temperature. A small but distinguishable change appears at 26 K. On the other hand, a large and non-monotonous changes of lattice parameter are observed along the *b*-axis with lowering temperature featuring a drastic and a large step like decreases at 26 K. Along the *c*-axis, the lattice parameter is relatively constant but again with a small step of change at 26 K.

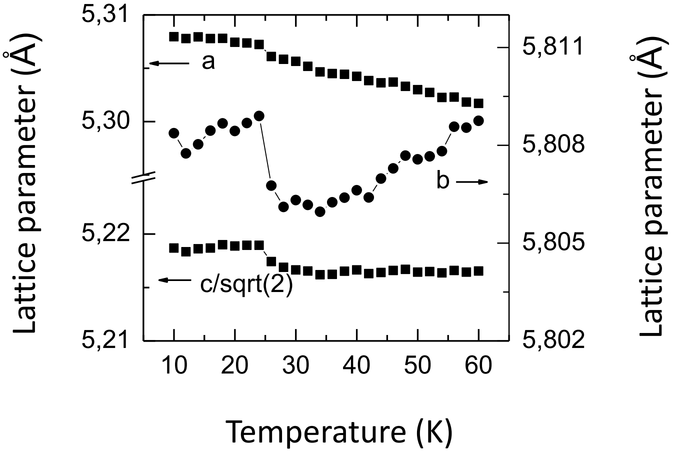

Figure 3.4: *The temperature dependence of lattice parameters.*

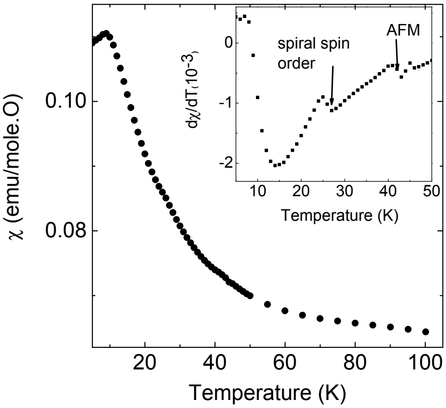

Figure 3.5: *The temperature dependent variation of magnetic susceptibility measured along the c-axis. The inset shows the derivative of the susceptibility displaying the AFM and spiral spin order transition*

The magnetization of our sample was measured using a Quantum Design MPMS-7 SQUID magnetometer in an applied magnetic field of 0.5 T. The result is presented in Fig. 3.5 showing magnetic susceptibility (χ) observed along the c-axis direction. The magnetic susceptibility is dominated by the response of the Tb^{3+} sublattice, which shows the typical paramagnetic 1/T dependence and antiferromagnetic ordering below 7 K. The inset of Fig. 3.5 shows the temperature derivative of the susceptibility to highlight the changes occurring at the temperatures where the Mn sublattice orders. These phase transitions are clearly marked by abrupt changes at 41 K and 26 K, associated with the occurrence of the sinusoidal AFM and the spiral spin structures, respectively.

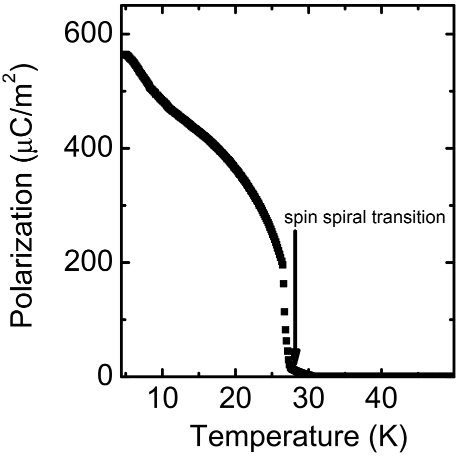

Figure 3.6: *The temperature dependent electric polarization measured along the c-axis.*

The spiral spin transition coincides with the appearance of spontaneous polarization along the c-axis, as indicated in Fig. 3.6, evidencing the multiferroicity of the sample. It is shown that the polarization sets in at 26 K and rises toward its maximum of about 600 $\mu C/m^2$, consistent with earlier reports [6]. This spontaneous polarization is about 1000 times smaller than the polarization observed in PZT [13]. The enhancement observed below 7 K, a phenomenon not observed in conventional ferroelectric materials, coincides with the formation of AFM ordering in the Tb sublattice. Supposedly, it is due to the magnetic coupling between the Tb and Mn spins that leads to the observed enhancement of the electric polarization as proposed previously [14, 15].

3.3 Optical Properties of $TbMnO_3$

The influences of orbital and magnetic interactions on optical properties of manganite oxide have been widely discussed [5, 16, 17]. The different absorption bands found in the compound of different rare earth element are closely relate to MnO_6 distortion as well as the Mn-O-Mn angle. The optical transitions are strongly dependent on orbital overlap between occupied and unoccupied states [5, 16] and spin ordering between two nearest neighbor (NN) of Mn ions [5, 17]. Figure 3.1 (a) show that the occupied orbital is parallel with unoccupied orbital in the *ab*-plane so that the orbital overlap and the intersite *d*-*d* transition probability should be large. Below the magnetic ordering temperature, two NN manganite ions have a primarily ferromagnetic alignment favoring intersite *d*-*d* transition. On the other hand, the occupied and unoccupied orbitals along the *c*-direction are orthogonal, minimizing the orbital overlap and therefore the intersite *d*-*d* transition along the *c*-direction.. The octahedral tilting and mixed orbital state apparently induces orbital overlap in *c* direction so that the intersite *d*-*d* transition is still possible. Below T_N, two NN Mn ions align antiferromagnetically so that the intersite *d*-*d* transition requires more energy to overcome the Hund's coupling energy. These different types of intersite *d*-*d* transitions appear in anisotropic optical spectra [5, 17]

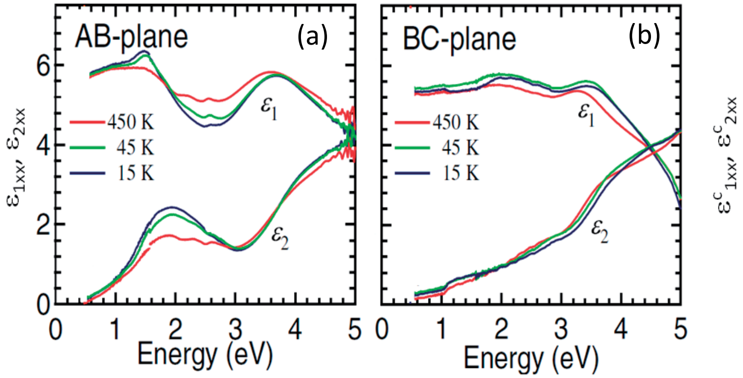

Figure 3.7: *The dielectric constant measured at (a) ab-plane and (b) bc-plane as reported at Ref. [18]*

The optical properties of TbMnO$_3$ in the energy range of 0.5 - 5 eV was studied by Bastjan et al.[18] observed optical dielectric constant using ellipsometry. Their spectra are shown in shown in Fig. 3.7. In the *ab*-plane, the optical dielectric constant has main features centered at 2 eV which can be detailed into separate peaks of 1.9 eV, 2.3 eV, and 2.6 eV. Besides, a broad band appears at a energy higher than 3 eV (see Fig. 3.7 (a)). The 2 eV band is sensitive to spin order while the higher one is relatively independent. The optical dielectric constant in the *bc*-plane features a broad energy band which depends only weakly on temperature with small bumps appearing around 2.6 eV and 3.8 eV (see Fig. 3.7 (b)).

To understand qualitatively the influence of the orbital and spin ordering on the optical properties of TbMnO$_3$ we adopt the discussion of LaMnO$_3$ [5, 17] and limit our discussion to the NN intersite *d*-*d* transitions mediated by the oxygen

p-orbitals. Crucial factors influencing the transition strength of the intersite d-d transitions are the orbital overlap between the Mn-d and O-p orbitals [16] as well as the spin alignment of the Mn ions involved. For the latter, a FM alignment favors the intersite d-d transition since in this case the transition does not require extra energy to overcome the Hund's coupling energy.

Below the orbital ordering temperature the e_g orbital is split and occupied by one electron. This electrons fill alternately the orbital $d_{3x^2-r^2}$ and $d_{3y^2-r^2}$ (AFO = antiferro-orbital) in ab-plane and the spin alignment between two NN of Mn is parallel (FM). Along the c-direction, the e_g electrons on adjacent Mn ions occupy the same type of orbital (FO = ferro-orbital ordering) and the spins are aligned anti parallel (AFM). In this situation, the $d_{x^2+z^2}$ and $d_{y^2+z^2}$ orbital are always unoccupied. It is noted that an orbital mixing between $d_{3z^2-r^2}$ and $d_{x^2+y^2}$ has been proposed to describe the occupied and unoccupied state of manganite. However, here we neglect this mixing and provide a qualitative description only.

The intersite d-d transitions excite electrons to either an empty or a half filled d-orbital. Adjacent ion pairs are transformed from a $\mathrm{Mn}^{3+}/\mathrm{Mn}^{3+}$configuration to the $\mathrm{Mn}^{4+}/\mathrm{Mn}^{2+}$ one. The excitation to an empty e_g orbital can lead to either a high spin (HS) or a low spin (LS) state, whereas excitation to a half occupied e_g orbital can lead to a LS state only due to the Pauli principle. Observation along different crystallographic axis with different spin allignment shows the 2 eV band is sensitive to magnetic order. Due to Hund's rule, the intersite d-d transition in ab-plane with FM spin alignment costs lower energy than the one along c-axis with AFM spin alignment. This consideration brings to interpretation that the band centered at 2 eV in the ab-plane should be intersite d-d transition with HS state. Transition to LS state and intersite d-d transition along c-axis has been discussed to be observed at optical band higher than 3 eV [17] and overlap with p-d charge transfer band. Other interpretations on the origin of 2 eV band is related to phonon assisted intra site transition. However, the temperature dependent shift of the optical band shows disagreement with this scenario [5].

The above assignments are supported by calculations of the transition energies[17]. The effective on-site Coulomb energy was estimated to be $U^{*}=U-V$ 2.8 eV, where U is the Coulomb repulsion on the same e_g orbital and V accounts for NN excitonic attraction. The cystal field splitting between t_{2g} and e_g is given as 10Dq $\approx$ 1.5 eV. Due to Jahn Teller splitting, two e_g levels apart with energy difference of $\Delta_{J_T} \approx 0.7$ eV. The Hund interaction has also been calculated to be $J_H \approx 0.5$ eV.

3.4 Dynamics of photo-excited electrons in magnetically ordered TbMnO_3

Unraveling the underlying interactions that dictate the emergent behavior in manganite oxides is not always straightforward using static experiments aimed at ground state properties and excited state spectra. In recent years it has become clear that extending the experimental repertoire to dynamical phenomena leads to valuable new insights. For instance, it offers the potential for temporally decoding the competing interactions [19–21]. One of the most straightforward implementations of this is the investigation of hot electron relaxation following the photo excitation, and its consequences on the transient material properties [19, 22]. As the sample temperature is lowered through a succession of phase transitions, apart from the conventional electron-phonon scattering channel, additional scattering channels alter the relaxation dynamics and provide a means to clarify the array of interactions that dictate the dynamical behavior. This methodology can be applied in many systems, including those where charge transport is influenced by underlying magnetism, and materials with coupled ferroic properties.

It is the purpose of the present study to investigate the coupling of charge (hopping) transport with magnetic order by probing the dynamic relaxation processes of the excited material. In addition, we are interested in the relevance of magneto-electric couplings in multiferroic materials to these relaxation dynamics. We have chosen $TbMnO_3$ which allows us to monitor these relaxation dynamics along orthogonal crystallographic directions with different underlying magnetic orderings. We find, not unexpectedly, that transport along these two directions are considerably different. Using a simple model, we describe the observed dynamics by considering the intersite hopping processes between nearest neighbors subject to the constraints imposed by the underlying magnetic lattice. In this picture, we see that electron-magnon interactions dominate the relaxation processes in the ordered magnetic state and find a strong coupling of the electron hopping process with low-energy magnonic excitations.

The sample for our experiment is cut and polished to obtain a *b*-axis surface normal. The crystal size is roughly 3mm x 2 mm in cross section and 0.5 mm in thickness. With this cut, two distinct magnetic orderings are optically accessible by a 90° rotation of the incoming light polarization: 1) Along the $< 100 >$ crystallographic axis (parallel to *a*-direction), ferromagnetic ordering is present, while 2) along the $< 001 >$ direction (parallel to *c*-axis) antiferromagnetic ordering is exhibited. Using light tuned to the manganite intersite *d*-*d* transition [18], we probe the magnetic order through the sensitivity of the intersite *d*-*d* transition to the underlying magnetic lattice along the associated ordering directions.

To illucidate the interactions between photo-injected electrons and the magnetic lattice, two-color pump-probe measurements were performed across a wide temperature range encompassing $T_{N,1}$=41 K and $T_{N,2}$=26 K. The hot electrons are photo excited onto the manganese site using 3.0 eV photons, the second harmonic of our laser, which is well tuned to oxygen-to-manganese charge transfer excitations [18]. Subsequently, the manganese-to-manganese intersite *d*-*d* transition is monitored by 1.5 eV light, the fundamental of our laser, which overlaps the nearest neighbor inter-site *d*-*d*-transition energy. Both beams are derived from our 1 kHz Ti:sapphire amplified laser system (Hurricane, Spectra Physics) which produces 200 fs pulses with a central wavelength of 800 nm. Pump and probe are spatially and temporally overlapped on the sample surface and the pump fluence is 0.1 mJ/cm^2 for all experiments reported here[1]. In order to probe the response along ferromagnetically and antiferromagnetically coupled directions, the probe light is polarized at 45 degrees with respect to the a- and c-axes and analysed by a Wollaston prism. The temporal dynamics are investigated in the temperature range between 9 K and 125 K.

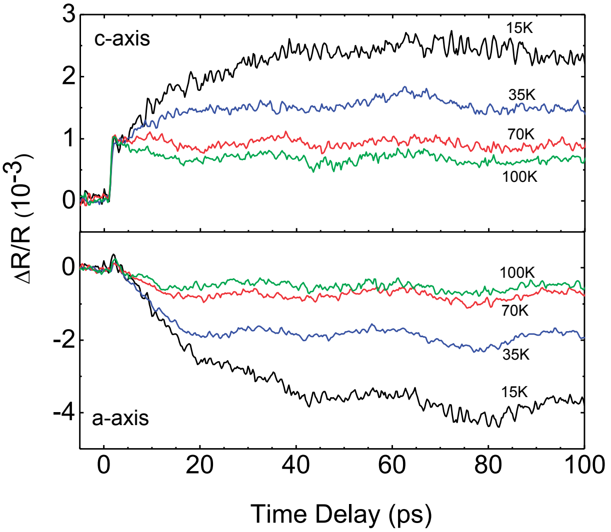

Figure 3.8: *Characteristic transient reflectivity curves along the two principal crystallographic directions for temperatures above and below the magnetic transition at 41 K. Along the ferromagnetically coupled a-axis, we witness a decrease in transient reflectivity while along the antiferromagnetically coupled c-axis we witness an increase in transient reflectivity.*

In figure 3.8 we show transient reflectivities $\frac{\Delta R(t)}{R}$ measured along the c-axis (top) and a-axis (bottom), as the sample temperature is lowered through the magnetic transition. The observed dynamics along the two axes are markedly different. In particular the photo induced state is marked by a reduction in reflectivity along the a-axis and an increase in reflectivity along the c-axis, while the trend is given by an increase of $|\frac{\Delta R_i(t)}{R}|_{i=a,c}$ as the temperature is lowered. The different behaviors along the two axes are further distinguished by the appearance of the temperature-independent ultrafast response along the c-axis, which is well matched to the pump-probe cross correlation. We also note a common oscillatory component which is attributed to generation of acoustic phonons. The responses along both axes persist longer than 300 ps, the limit of our translation stage.

---

[1] The pump fluence is in the linear regime as checked by fluence dependent experiments

Further analysis of the transient reflectivity is provided in figure 3.9, where we show the temperature dependent transient reflectivity at the metastable state, measured at 95 ps time delay. Representative error bars are the standard deviation of the data points in a small time window around the 95ps time delay. For the *c*-axis data (squares) the sharp jump at zero time delay is subtracted. The first magnetic phase transition at $T_{N,1}$=41 K is clearly visible as changes in the slopes along both axes. Changes at $T_{N,2}$=26 K are also present, but less noticeable. To highlight these more subtle changes, a linear fit in the region between $T_{N,1}$ and $T_{N,2}$ is included. Deviations from linearity are now evident as a slight change in the slope at $T_{N,2}$. Additionally, we observe a difference in signal amplitude above $T_{N,1}$ for the two crystallographic directions, indicative of possible effects of different short range magnetic order that persists for temperatures above the magnetic ordering temperatures. Signatures of such short range order were found by Bastjan *et. al.* [18] up to 300 K. We note that even above the magnetic ordering temperature, orbital order and structural distortions persist up to 800 K[4, 9], and therefore it is not surprising to see slight deviations along the different axes.

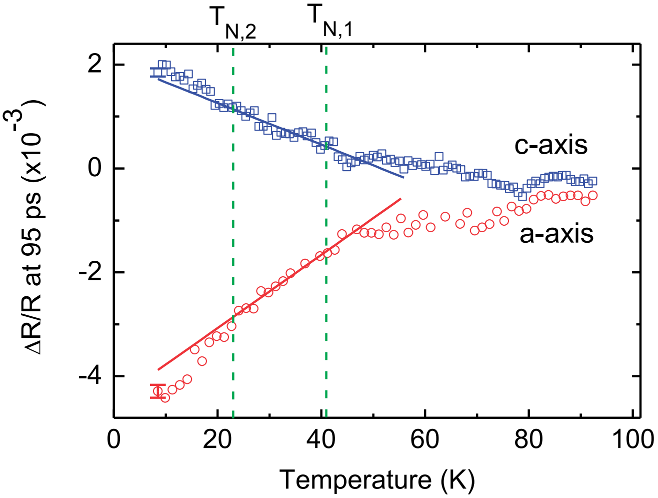

Figure 3.9: *The transient reflectivity probed at 95 ps shows clear changes in amplitude at the first magnetic transition, $T_{N,1}$. Using a solid linear fit between 26 K and 42 K, more subtle changes are observed in amplitude at $T_{N,2}$. Above the magnetic transition the difference in transient reflectivity indicates that short range magnetic interactions persist.*

The onset of magnetic ordering is further revealed in the extracted time constants, obtained from fitting the time dependent transient reflectivity with a single exponential function and plotted with respect to varying temperature in figure 3.10. The inset shows such representative curves (deduced from figure 3.8) together with their fit for temperatures spanning the magnetic transitions. Upon entering the magnetic phase at 40 K the dynamic response slows down dramatically. Above the transition temperature, the onset time remains constant up to 100 K, most easily seen in the a-axis response. The c-axis response is less clear due to the difficulty in fitting the fast component at t_0 (See Fig. 3.8). As the temperature is lowered, the time constants along both axes asymptote to a value of $\tau = 17$ ps.

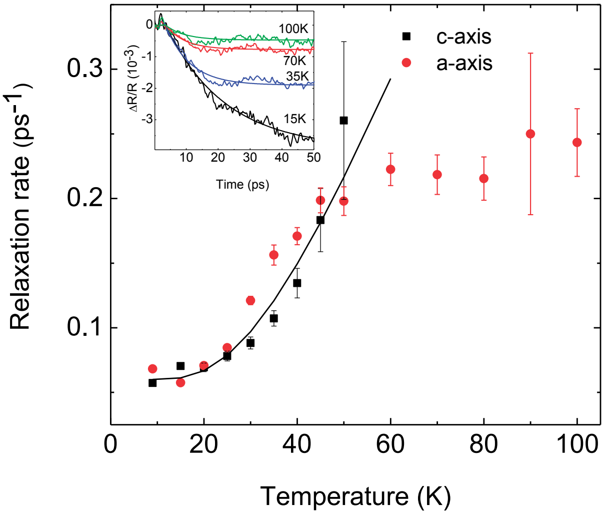

Figure 3.10: *The relaxation rates of photo-injected electrons, obtained by fitting an exponential function as shown in the inset, exhibits an increase in the time constant as a function of temperature. Fitting this time constant to a Bose-Enstein distribution for the number of magnons at temperature T, we extract a characteristic energy of 8 meV, well matched to the near zone boundary magnon energy.*

To interpret the observed dynamics we must consider the effects of both the underlying magnetic interactions, the main aim of this study, and those arising from differences in structure. We first briefly address the jump in reflectivity apparent along the c-axis and absent along the a-axis, which we can identify as having a non-magnetic origin. The direct indication of this is the absence of temperature dependency in the amplitude of this effect. Furthermore, this fast transient reflectivity linearly depends on the number of photo-excited electrons, as evidenced by experiments performed at different fluences *(data not shown)*. We therefore attribute this feature to optical intersite d-d transitions induced by the presence of the photo excited electrons, which is favorable along the c-direction due to the out-of-plane nature of the newly occupied orbitals ($x^2 - z^2$ or $y^2 - z^2$). Apart from this instantaneous jump, the 'slow' onset and long lived dynamics are interpreted as arising from the interaction between the photo excited electron and the underlying magnetic lattice. This is evident in the amplitude of the transient reflectivity at long time delays as shown in figure 3.9. Changes in the amplitude, manifested as modifications of the slope in figure 3.9, directly map to the magnetic transitions independently measured in [11, 12]. We profer this magnetic interaction as the dominant effect in determining the long lived temporal evolution by noting that the underlying lattice parameters continuously change over the entire temperature range [23], displaying only a modest change at the temperature where we see our largest change in dynamics.

To understand the interaction between the photo excited electron and the underlying magnetic lattice, we first consider the effects of magnetic ordering on the reflectivity at the probe wavelength. The relevant transitions at 1.5 eV are the intersite *d*-*d* transitions $(\mathrm{Mn}^{3+},\mathrm{Mn}^{3+})\rightarrow(\mathrm{Mn}^{2+},\mathrm{Mn}^{4+})$. As has been discussed by Kovaleva et. al. and Bastjan et al. [17, 18], the energy of this transition depends on the spin alignment of the neighboring Mn^{3+} ions. For parallel alignment, as is the case along the *a*-direction, the transition occurs around 1.5-2 eV, whereas for antiparallel alignment (along the *c*-direction) the energy of this transition is increased by Hund's energy. Therefore one expects for the perfect spin ordered case, the transitions along the *a*-direction have maximal probability, whereas those along the *c*-direction have minimal probability.

Next we consider the effect of photodoping on the e_g levels through an oxygen to manganese *p*-*d* transition, resulting in the creation of Mn^{2+} ions. Once created, the additional electron which, through Hund's rule coupling, will be spin aligned, can in principle hop to different Mn sites leading to a photo-induced hopping conductivity. In the presence of magnetic order, this hopping is expected to be highly anisotropic. Along the *a*- and *b*-directions where the magnetic alignment of neighboring Mn sites is predominantly ferromagnetic, the hopping costs minimal energy, and moreover, will not affect the magnetic order of the system. In contrast to this, hopping along the *c*-direction, where the spin alignment is antiferromagnetic, is prohibited by an energy cost equivalent to Hund's energy unless a spin-flip occurs. Therefore, along this direction only magnon-assisted hopping is allowed which strongly modifies the ground state magnetic order. Each hop of the photo excited electron along the *c*-direction necessarily modifies the optical response along both axes at 1.5 eV. One hopping process along *c*-axis, creates a magnonic excitation leading to a decrease in magnetic order. This induced magnetic disorder naturally leads to the observed negative response along the *a*-direction (decrease of NN ferromagnetic alignment) and a positive response along the *c*-direction (decrease of antiferromagnetic NN alignment). Furthermore, the trend with decreasing temperature towards increasing signal amplitude can be seen in the same light. As the temperature is increased from zero, thermally induced magnetic disorder in the system increases, reducing the magnitude of the pump induced signal. Finally, the probability of this magnon-assisted hopping process is known to scale with the magnon number density [24] and hence observed time constant is expected to increase as the temperature is raised.

Based on the above discussions, we interpret the transient behavior of the reflectivity presented in Figs. 3.9 and 3.10 as the signature of photo-induced magnon assisted hopping conductivity leading to a transient reduction of the magnetic order in the material. The rate of decrease of magnetic order is proportional to the hopping probability and hence to the magnon number density $n(\omega_q, T)$.

Since we are considering hopping to nearest neighbors in the c-direction, the relevant magnon frequency, ω_q, dominating the hopping process should be the lowest zone boundary magnon frequency. This is indeed corroborated by the observed temperature dependence of the fitted time constants. The time constants extracted from our fitting procedure are shown in figure 3.10. The time constant data is fitted with a Bose-Einstein distribution - combined with a constant to accommodate additional relaxation processes ($[A/exp(\hbar\omega_q/k_BT) - 1]^{-1}$+B) - between the 10 K and 41 K, giving the average number density of magnons at temperature T. The characteristic energy of extracted from the fit is 8.5 ± 1 meV, well matched to the energy of the zone boundary excitation as observed in [8]. This magnetic excitation is known to disperse from 1.5 meV at zone center to 8.5 meV at the boundary. In probing the hopping conductivity, we focus particularly on nearest neighbor magnetic alignment, which couples most strongly to the zone boundary excitation.

3.5 Photo-induced Modulation of Ferroelectric Polarization in Multiferroic TbMnO$_3$

The ability to control different states of ferroelectric materials by optical means has important applications in device technology such as optically addressed ferroelectric memories [25–27] and optically driven mechanical actuators [28]. Among the most widely studied materials in this connection is the lead zirconate titanate (PZT). More recently, efforts have also been dedicated to develop new functional materials, often based on complex oxides [29, 30] exploiting their intricate interplay between the charge, lattice, and spin degrees of freedom in these materials. One of the strong driving forces behind this research is the need for new types of electronic devices and for lead-free non-toxic ferroelectric devices to be used in for instance biomedical applications.

One of the intriguing phenomena observed in normal ferroelectrics is the photoexcitation induced transient current [31–34]; a phenomenon which is sensitive to the polarization state of the material [32]. Several interpretations have been proposed to understand the origin of the induced transient current, including transient pyroelectric current [31], photovoltaic [32, 33], and photo-strictive effects [34]. This section reports the results of a study of photo-induced ferroelectricity modulation in TbMnO$_3$. Here we demonstrate that light irradiation can also induce a transient pyroelectric current in the ferroelectric phase of TbMnO$_3$ even though the static electric polarization is very small compared to that in conventional ferroelectric materials. We conclude that for $TbMnO_3$ the transient current is induced by a thermal modulation of the ferroelectric polarization.

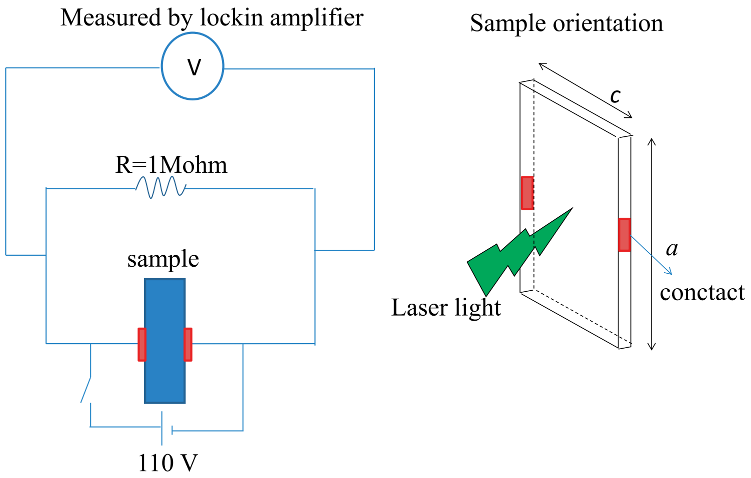

Figure 3.11: *The experimental setup and sample orientation for photo-induced transient voltage experiment*

Having been assured of the multiferroic nature of the sample, we investigated the ferroelectricity modulation by measuring the transient voltage following laser illumination of the sample. The electronic circuit and sample orientation are schematically depicted in Fig. 3.11. For this experiment, two gold pads of 1 mm^2 were deposited on the a-c plane of the sample with 2 mm spacing in the c direction. Platinum wires were used to connect these gold electrodes to the terminals of a chip carrier. The sample was mounted on the cold finger of a He flow cryostat. A 110 V external voltage from a Keithley 236 was used to pole the sample during cooling and was disconnected during measurement of the induced transient voltage along the c axis (Vc). The photo-induced voltage was measured by illuminating the sample in the ac plane with a 532 nm continuous wave laser modulated by a 100 Hz chopper and recording the resulting amplitude of the transient voltage across the sample using a SR-830 lock-in amplifier synchronized to the chopper frequency from 10K up to 35K. In order to get insight into thermal effects on transient voltage, a separate transient voltage measurement was performed using a heat pulse generated by Philips PM 5712 pulse generator with 1 kHz frequency and output energy of 1 μJ/pulse. The transient signal was measured with the same set up as for photo-induced transient voltage measurement.

Fig. 3.12 shows some typical photo-induced transient voltage curves obtained using the configuration depicted in Fig. 3.11 for a number of photo-excitation power densities. The curves show a sudden rise of the signal below a certain temperature in the vicinity of the ferroelectric transition temperature. Upon lowering the temperature the voltage rapidly reaches a peak value and thereafter reduces again to a more or less temperature independent level at lower temperatures. The amplitude of the transient voltage is seen to increase with increasing laser power density. The fact that the onset of the initial transient signal is about 2 K below that of ferroelectric transition is due to the reduced thermal contact of the sample mounted in a chip carrier with the cold finger of the cryostat. Apart from that, the onset temperature is also observed to depend on power density. We attribute this latter shift to a temperature rise of the sample due to laser heating (about 3 K at 21 W/cm^2).

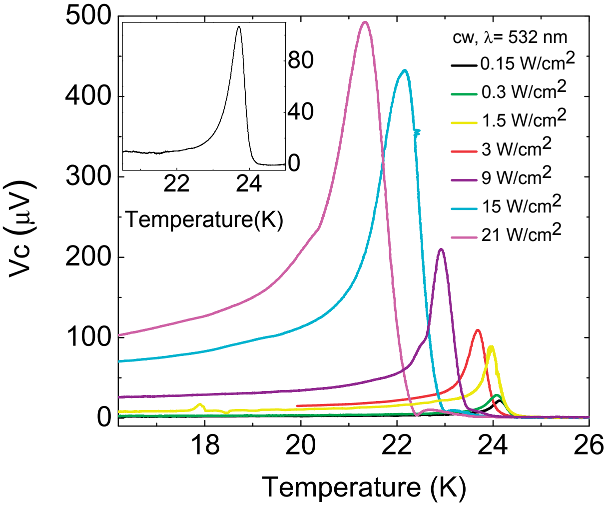

Figure 3.12: *The temperature dependent transient voltage induced by 532 nm laser light of power density varying from 0.15 up to 21 W/cm^2. The inset shows a typical curve of the transient voltage induced by heat pulse.*

The inset of Fig. 3.12 shows the similarity between temperature dependent photo-induced transient voltage and a typical result obtained using the heat pulse method. This similarity indicates that the observed transient voltage has its origin in the pyroelectric current produced most likely by thermally modulating ferroelectric polarization.

The observed pyroelectric current (I) is induced by the time variation of the ferroelectric polarization (P)[35]:

$$I = A\frac{dP}{dt} = A\frac{dP}{dT}\frac{dT}{dt} \tag{3.1}$$

where A is the electrode area. In static experiments, one keeps the rate of change of temperature constant over a wide temperature range. Hence the electric polarization can be approximated as the integral of current over temperature (T), or alternatively over time (t):

$$P = \int \frac{I}{A} \left[\frac{dT}{dt} \right]^{-1} dT = \int \frac{I}{A} dt \tag{3.2}$$

This formula is used to obtain the electric polarization as presented in Fig. 3.6.

As discussed above, we interpret the appearance of the observed transient voltage as due to a modulation of the temperature, and hence of the polarization, induced by the modulated laser irradiation. To find the connection between the transient voltage and the temperature modulation we consider a simplified situation where the temperature variation is modeled by a sinusoidal modulation at the frequency ω of the optical chopper:

$$T(t) = T_i + \Delta T_{av} + \Delta T_m sin(\omega t) \tag{3.3}$$

where T_i and T_{av} are the temperature without laser illumination, and the laser induced average temperature rise, respectively. The third term represents the temperature modulation due to the chopped laser which induces the polarization modulation. Substituting Eq. 3.3 into Eq. 3.1 yields the pyroelectric current modulation

$$I(T) = A \Delta T_m \omega cos(\omega t) \frac{dP}{dT} \tag{3.4}$$

Therefore, assuming small modulations such that dP/dT can be taken as constant, the root mean square (rms) transient voltage measured by the lock-in amplifier can be expressed as

$$V_{rms} = RI_{rms} = \frac{RA\Delta T_m \omega}{\sqrt{2}} \frac{dP}{dT} \tag{3.5}$$

where R is the total resistance in the electronic circuit and dP/dT is the derivative of the curve in Fig. 3.6.

Though the approximations made above are not always fully justified, in particular the assumption of constant dP/dT at high laser powers, the simplified model does show a fairly good agreement between the temperature dependence of the measured transient voltage and derivative of Fig. 3.12 (scaled by a constant α), as shown in Fig. 3.13.

3.6 Conclusions

In conclusion, we unraveled the detailed scenario of charge-spin interactions by means of relatively simple time resolved experiments, which has in particular

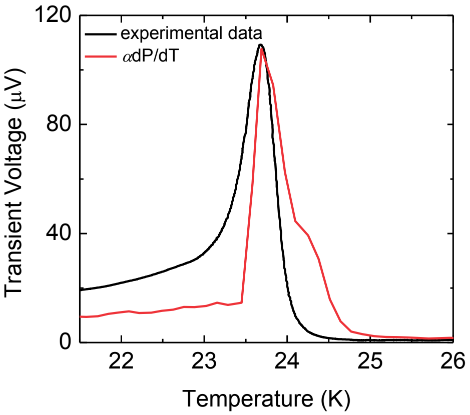

Figure 3.13: *Comparison between the observed transient voltage (black line) at a laser power density of 3 W/cm^2 with the derivative of the curve of Fig. 3, dP/dT (red line). The temperature scale of dP/dT has been shifted to match with the onset of transient voltage*

showed the intrinsic correlation between hopping conductivity and magnetic order. The charge-spin correlation is observed by investigating transient response of two different crystallographic axes which have different types of spin alignment. The temperature dependent as well as the anisotropic behavior of transient response has led to a conclusion that at magnetic ordered phase, the relaxation process of excited electrons is strongly coupled to spin, and is effectively mediated by magnons. The results presented here are expected to be relevant not only for $TbMnO_3$, but certainly also for conducting chemically doped variants of this material, as well as for many other 3d oxide compounds.

In addition we have also shown that the ferroelectric nature of the multiferroic complex oxide $TbMnO_3$ can be studied by means of laser induced pyroelectric current modulation experiments. Even though the electric polarization in this system is very small in comparison to those of conventional ferroelectric systems, the polarization modulation is readily observed in our experiment and is interpreted in terms of a temperature modulation of the ferroelectric polarization on the basis of rms response. It would be interesting to extend this method into the time domain in order to elucidate the dynamical properties of the polarization modulation in multiferroic oxides and their potential in fast switching applications.

Bibliography

[1] Y. Tokura and N. Nagaosa. *Science*, 288:462, 2000.

[2] A. P. Ramirez. *Journal of Physics - Condensed Matter*, 9:8171, 1997.

[3] S W Cheong and M Motovoy. *Nature*, 6:13, 2007.

[4] J.-S. Zhou and J. B. Goodenough. *Phys. Rev. Lett.*, 96:247202, 2006.

[5] M. W. Kim, S. J. Moon, J. H. Jung, Jaejun Yu, Sachin Parashar, P. Murugavel, J. H. Lee, and T. W. Noh. *Phys. Rev. Lett.*, 96:247205, 2006.

[6] T. Kimura, T. Goto, H. Shintani, K. Ishizaka, T. Arima, and Y. Tokura. *Nature*, 426:55, 2000.

[7] J. M. Chen, T. L. Chou, J. M. Lee, S. A. Chen, T. S. Chan, T. H. Chen, K. T. Lu, W. T. Chuang, H.-S. Sheu, S. W. Chen, C. M. Lin, N. Hiraoka, H. Ishii, K. D. Tsuei, and T. J. Yang. *Phys. Rev. B*, 79:165110, 2009.

[8] D. Senff, N. Aliouane, D.N. Argyriou, A. Hiess, L.P. Regnault, P. Link, Sidis Y. Hradil, K., and M. Braden. *Journal of Physics - Condensed Matter*, 20:434212, 2008.

[9] T. Kimura, S. Ishihara, H. Shintani, T. Arima, K. T. Takahashi, K. Ishizaka, and Y. Tokura. *Phys. Rev. B*, 68:060403, 2003.

[10] S. Quezel, F. Tcheou, J. Rossat-Mignod, G. Quezel, and E. Roudaut. *Physica B+C*, 86:916–918, 1977.

[11] R. Kajimoto, H. Yoshizawa, H. Shintani, T. Kimura, and Y. Tokura. *Phys. Rev. B*, 70:012401, 2004.

[12] N. Mufti, A. A. Nugroho, G.R. Blake, and T.T.M. Palstra. *Phys. Rev. B*, 78:024109, 2008.

[13] H. Nakaki, H. Uchida, S. Koda, S. Okamoto, and H. Funakubo. *App. Phys. Lett*, 87:182906, 2005.

[14] T. Goto, T. Kimura, G. Lawes, A. P. Ramirez, and Y. Tokura. *Phys. Rev. Lett*, 92:257201, 2004.

[15] O. Prokhnenko, R. Feyerherm, E. Dudzik, S. Landsgesell, N. Aliouane, L. C. Chapon, and D. N. Argyriou. *Phys. Rev. Lett*, 98:057206, 2007.

[16] K. Tobe, T. Kimura, Y. Okimoto, and Y. Tokura. *Phys. Rev. B*, 64:184421, 2001.

[17] N. N. Kovaleva, A. V. Boris, C. Bernhard, A. Kulakov, A. Pimenov, A. M. Balbashov, G. Khaliullin, and B. Keimer. *Phys. Rev. Lett.*, 93:147204, 2004.

[18] M. Bastjan, S. G. Singer, G. Neuber, S. Eller, N. Aliouane, D. N. Argyriou, SL Cooper, and M. Rübhausen. *Phys. Rev. B*, 77:193105, 2008.

[19] RD Averitt, AI Lobad, C Kwon, SA Trugman, VK Thorsmølle, and AJ Taylor. *Phys. Rev. Lett.*, 77:4025, 2001.

[20] M. Matsubara, Y. Okimoto, T. Ogasawara, Y. Tomioka, H. Okamoto, and Y. Tokura. *Phys. Rev. Lett.*, 99:207401, 2007.

[21] C. Boeglin, E. Beaurepaire, V. Halt*é*, V. L*ó*pez-Flores, C. Stamm, N. Pontius, H. A. D*ü*rr, and Bigot J-Y. *Nature*, 465:458, 2010.

[22] E. Beaurepaire, J-C. Merle, A. Daunois, and J-Y. Bigot. *Phys. Rev. Lett.*, 76:4250, 1999.

[23] J. Blasco, C. Ritter, J. Garcia, J. de Teresa, J. Perez-Cacho, and M. Ibarra. *Phys. Rev. B*, 62:5609, 2000.

[24] S. F. Zhang. *Journal of Applied Physics*, 79:4542, 1996.

[25] J.F. Scott and C.A. P. De Araujo. *Science*, 246:1400, 1989.

[26] S. Takhoor. *Appl. Phys. Lett*, 60:3319, 1992.

[27] S. Takhoor, E. Olson, , and R. H. Nixon. *Integrated Ferroelectrics*, 4:257.

[28] T. Ikehara, M. Tanaka, S. Shimada, and H. Matshuda. *Sensor and Acutuator*, 22:239, 2001.

[29] G. Catalan and J. F. Scott. *Advanced Materials*, 21:2563, 2009.

[30] W. Prellier, M. P. Shingh, and P. Murugavel. *J. Phys. Condens. Matt*, 17:R803, 2005.

[31] J. Lee, S. Esayan, J. Prohaska, and A. Safari. *Appl. Phys. Lett.*, 64:294, 1994.

[32] J. Lee, S. Esayan, J. Prohaska, and A. Safari. *Appl. Phys. Lett.*, 72:130, 1998.

[33] K. Yao, B. K. Gan, M. Chen, and S. Shannigrahi. *Appl. Phys. Lett.*, 87:212906, 2005.

[34] A. L. Kholkin, S. O. Iakovlev, and J. L. Baptista. *Appl. Phys. Lett.*, 79:2055, 2001.

[35] H.J.Sajosh. *Infrared Physics*, 28:263, 1988.

Chapter 4

Phase Transitions in Half Doped Layered Manganite $Pr_{0.5}Ca_{1.5}MnO_4$

4.1 Introduction

The mixed valence manganites are known to show a complex phase diagram arising from the competition and interplay between the spin, charge, and orbital degree of freedom. These phenomena further lead to a rich variety of physical properties which can be controlled by chemical substitution as well as temperature, pressure, and external fields. One of the best known phenomena observed in this type of materials is the colossal magneto resistance which is due to the enhancement of the electron hopping probability in the magnetic field induced ferromagnetic state [1].

The properties of the mixed valence manganites in a crystal system containing MnO_6 octahedral are known to depend strongly on the ratio between the amount of Mn^{3+} and Mn^{4+} ions, the local distortions of the Mn-O coordination, the dimensionality, and the detailed connectivity between the MnO_6 octahedra [2, 3]. One of the key parameters controlling the electronic properties of these mixed valence compounds is the intersite transfer probability of the electrons in the e_g orbitals. The related electron mobility strongly depends on the types of magnetic order, and plays a crucial role in the competition between the double exchange mechanism favoring a ferromagnetic-metallic state and the superexchange interaction mechanism which favors an antiferromagnetic-insulating state. In the case of half-doped system (equal number of $Mn^{3+}$and Mn^{4+}ions), there is a strong tendency to charge ordering in conjunction with an ordering of the e_g orbital occupations.

The stabilities of charge order(CO), orbital order (OO), and spin order (SO) depend strongly on the size mismatch between the rare earth (R^{3+}) ion and the divalent ion of alkali metal dopant (A^{2+}) [4, 5]. Variations of R^{3+} and A^{2+} radii lead to different Mn-O bond lengths as well as Mn-O-Mn angles, resulting in a variation of structural distortion of the MnO_6 octahedra. In the case of a half doped system, two parameters related to R^{3+} and A^{2+} sizes have been proposed to play a crucial role in the occurrence of long or short range orbital and charge ordering; namely the average radius and the variance of the radius. The average value of the radius is defined by $r_{av} = \Sigma_i x_i r_i$, with r_i denoting the radius of ion $i = (A^{2+}, R^{3+})$, and x_i its fractional occupation. The variance is defined as $\sigma^2 = \Sigma_i x_i r_i^2 - r_{av}^2$

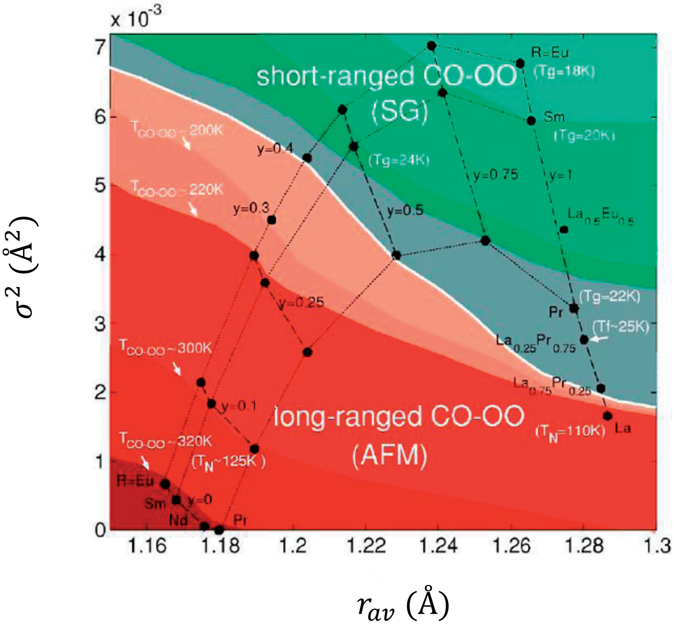

Figure 4.1: *The phase diagram of single layered manganite in terms of the average radius and variance (see text), adapted from Ref. [5]*

Figure 4.1 shows the phase diagram of single layered mixed valence manganite in terms of the variance and the average radius. For large average radius and large variance the ground state is a disordered state with short range charge and orbital orders exhibiting a spin glass behavior (green and blue areas in figure 4.1). This phase has been dubbed the 'quenched disorder' phase. Long range CO-OO order are found in the structure with relatively small variance or small average radius (red and orange areas in figure 4.1). For small enough average radius and variance, the system also shows antiferromagnetic order (red areas in figure 4.1). For very large average radius (not shown here), the distortion of the octahedra becomes small, favoring double exchange between the Mn ions and a ferromagnetic metallic state.

The work described in this chapter is focused on the investigation of the phase transitions in half doped layered system $Pr_{0.5}Ca_{1.5}MnO_4$ (PCMO). This compound has a relatively small average radius of 1.18 Å and a small variance of 2×10^{-7} Å^2 yielding a large octahedral distortion and corresponding suppression of the quenched disorder. These conditions lead to a high CO-OO phase transition temperature of 320 K, followed by the formation of two dimensional (2D) short range AFM at 200 K, and three dimensional (3D) long range AFM and 127 K, respectively [5, 6].

In order to investigate the nature of these phases and the related phase transitions, a variety of experiments have been performed that are discussed in the remainder of this chapter which is organizing as follows: After an introduction to the charge, orbital, and spin ordering phenomena observed in $Pr_{1-x}Ca_{1+x}MnO_4$, this chapter presents the experimental results of X-ray diffraction (section 4.3)and magnetization measurement(section 4.4). These will be continued by the presentation of experimental result based on the resistivity (section 4.5), specific heat (section 4.6), and Raman spectroscopy (section 4.7) measurements. These experimental findings, particularly in relation to the phase transitions and various orderings, are discussed in section 4.8. Finally, the summary of the results and the conclusion are given in section 4.9.

4.2 Overview of $Pr_{1-x}Ca_{1+x}MnO_4$ Properties

The single layer $Pr_{1-x}Ca_{1+x}MnO_4$ compound belongs to the family of the Ruddlessden-Popper compounds which crystallize in an orthorhombic distorted K_2NiF_4 crystal structure, as shown in Fig. 4.2 (a). The crystal structure consists of corner sharing MnO_6 octahedra forming a single layer structure sandwiched by a rock-salt type Pr(Ca) structure. This type of structure can be considered as a quasi-two dimensional (2D) MnO_2 layered structure.

Fig. 4.2 (b) shows the phase diagram of $Pr_{1-x}Ca_{1+x}MnO_4$ [7]. For hole doping concentration less than 0.35, the system shows a charge exchange (CE)-glass state with short range orbital order even down to very low temperature. The onset of long range CO-OO order (T*) occurs at doping concentration of $x = 0.35$ with a CO-OO transition temperature of 200 K, as observed in transmission electon microscopy [8]. Further increase of the doping concentration up to $x = 0.5$ results in an increase of the CO-OO transition temperature (T_{CO-OO}). For 0.5 $<x<$0.7, the T_{CO-OO} remains more or less constant at 325 K. As shown in Fig. 4.2 (b), the AFM ordering starts to appear at half doping, x=0.5, with a transition temperature of $T_N = 130$ K which slightly decreases in overdoped systems (0.55<x<0.7). In addition to that, indication of the 3D magnetic correlation and 2D short range AFM order in the (ab)-plane) have been reported, based on the existence of a largely broadened peak in the temperature dependent AC magnetic susceptibility [5] for doping concentration $x \geq 0.5$. The underdoped system does not show AFM ordering, but rather tends to be in spin glass (SG) phase, with onset temperature T_f.

This work focuses on the half doped layered manganite $Pr_{0.5}Ca_{1.5}MnO_4$, which exhibits a CO-OO transition at 320 K [5, 7–9] and AFM order below 130 K [5–7]. At lower temperatures, the system has been proposed to have a CE-type

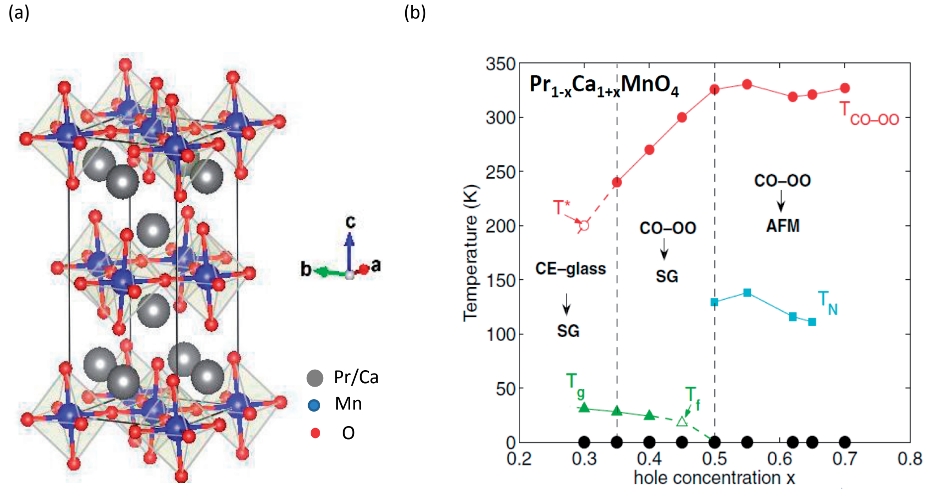

Figure 4.2: *(a) The crystal structure of single layered manganite and (b) the phase diagram of* $Pr_{1-x}Ca_{1+x}MnO_4$ *taken from Ref. [7].* T^*, T_g, *and* T_f *indicate the onset temperature of long range charge-orbital order, the spin glass state, and the onset of spin glass transition, respectively*

ordered structure [10] similar to the isostructural $La_{0.5}Sr_{1.5}MnO_4$ compound [6, 7]. A previous study also reported a structural phase transition from tetragonal to orthorhombic occurring at 470 K [11]. Both CO-OO and AFM transitions in this system were shown to be accompanied by structural changes [6, 9]. It was pointed out that the change in orthorhombicity at T_N indicates an important coupling between the spins and the lattice [6], which distinguishes $Pr_{0.5}Ca_{1.5}MnO_4$ from many of other manganites [12, 13].

The charges in $Pr_{0.5}Ca_{1.5}MnO_4$ order in a checkerboard manner as depicted in Fig. 4.3 [6]. This ordering includes an orbital ordering of the e_g orbitals on the Mn^{3+}sublattice, where the occupied $d_{3x^2-r^2}$ and $d_{3y^2-r^2}$ orbitals alternately bridge the Mn^{4+}ions [8]. The CO-OO order occurring at 320 K is followed by an AFM spin ordering below 130 K, with the Mn spins aligned ferromagnetically (FM) along the zig-zag chain in the ab plane, and antiferromagnetically (AFM) between adjacent zig-zag chain. In this conventional model, the orbital as well as the spin orientations are confined in the ab-plane. The orbital and spin interaction along the c axis are considered to be weak.

Recently it became clear from soft x-ray linear dichroism experiments that the simple picture of pure in plane orbital ordering is not completely correct since there is a substantial mixing of the in plane $d_{3x^2-r^2}$ ($d_{3y^2-r^2}$) e_g orbitals with the out of plane $d_{x^2-z^2}$ ($d_{y^2-z^2}$) e_g orbitals leading to interlayer orbital interactions as well [14, 15]. In addition, there are indications that the spin orientation is also

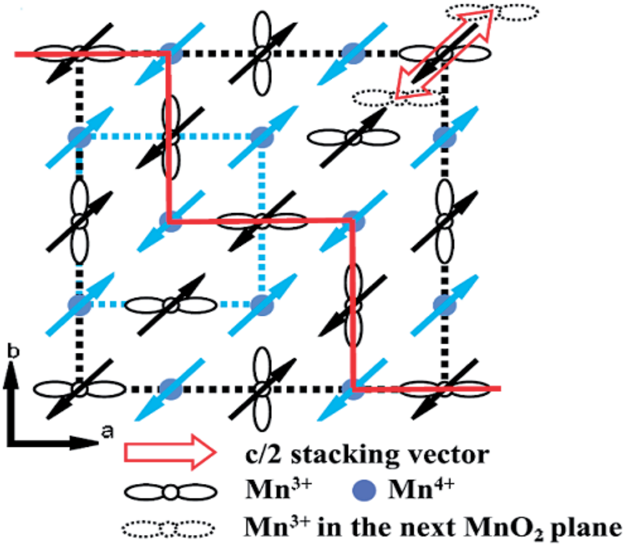

Figure 4.3: *The CE type structure in* $Pr_{0.5}Ca_{1.5}MnO_4$*, adopted from Ref. [6]*

not exactly in plane, but rather slightly canted along the *c* direction [16]

4.3 Structural Characterization

The crystal structure of $Pr_{0.5}Ca_{1.5}MnO_4$ was investigated using X-ray diffraction technique on powder obtained by pulverizing the single crystal sample. High temperature spectra were measured by a Bruker-D8 Advanced Diffractometer using Cu-K_α radiation at temperature ranging from 298 K up to 343 K. The measurement was carried out with interval of 0.02 degree/step and an integration time of 4 s/step. The low temperature spectra, ranging from 300 K to 40 K, were measured using a Huber G670 diffractometer with total scanning time 16 hours for each spectrum.

The crystal structure of the $Pr_{0.5}Ca_{1.5}MnO_4$ was first analyzed for the spectra measured at 293 K and compared with previously suggested space groups of Pbmn, Pbcm, Bbam, Pban, Pbnm, [11], Pmam [17]and Bmab [6, 9, 11]. The Bmab space group was found to give the best refinement, not only for the 293 K data, as shown in Fig. 4.4, but also for the whole temperature range. The Bmab space group is isomorphic with Cmca which allows the same position to accommodate either the Mn^{3+}or Mn^{4+}ions [18]. In our refinement, Mn positions are fixed by symmetry at the (0,0,0) position with Wyckoff position 4a whereas the O and Pr/Ca positional parameters are optimized by the analysis. The refined orthorhombic has lattice parameters a = 5.3760(28) Å, b = 5.4107(57) Å, and c = 11.8301(90) Å at room

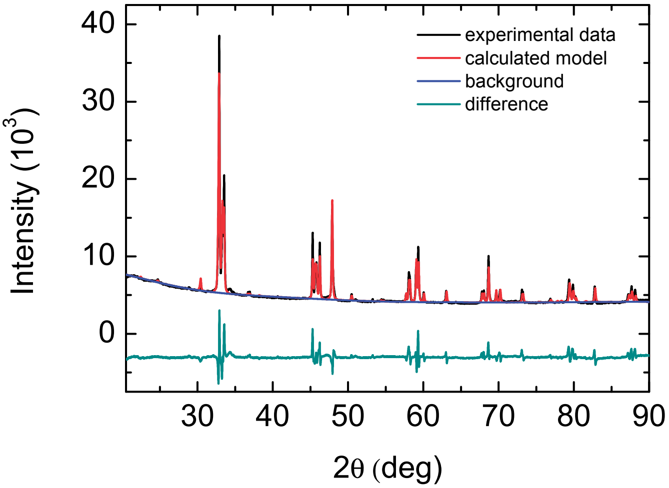

Figure 4.4: *X-ray diffraction data recorded using a Huber G670 diffractometer at 293K and its refinement based on a Bmab space group model. The black, red, blue and light blue lines represent the experimental data, the Bmab based calculated refinement, the background, and the residual spectrum, respectively.*

temperature. The Wyckoff positions of O ions are found at 8e and 8f whereas it is at 8e for the Pr/Ca ions. Details of the refinement at 343 K (disordered phase), 293 K (CO-OO phase), and 40 K (AFM phase) are provided in table 4.1.

Another space group previously suggested for the COO phase is the Pnma group[19], one of the subgroups of Bmab. In this space group, a doubling of the unit cell along the b axis is considered to occur in COO phase. The Mn^{3+} and Mn^{4+} are expected to sit at different positions and have different types of MnO2 octahedral environments. In this case only the Mn^{3+} position is fully fixed by symmetry, whereas the other ions, including the Mn^{4+} ion, are free to be adjusted during the refinement. Our XRD refinement based on the Pnma space group also gives a good fit to the data for the whole temperature range. However, the Pnma refinement does not give a substantial improvement over the result of Bmab refinement despite the use of more adjustable free parameters. Therefore, we chose to use the Bmab space group for the structural analysis presented in our report.

Despite unchanged space group across the T_{CO-OO}, the evolution of (020) and (200) diffraction peaks indicate that structural changes do occur across the T_{CO-OO}. As is shown in Fig. 4.5, the two peaks which are largely overlapping above T_{CO-OO} become fully split below it, indicating that the ratio between the length of a and b lattice parameters undergoes substantially changes across T_{CO-OO}.

Fig. 4.6 (a) shows the temperature dependence of the lattice constants, the unit

Table 4.1: *Refinement results of the diffraction data recorded at the disordered (343 K), charge and orbitally ordered (293 K), and antiferromagnetically ordered (40 K) phases of* $Pr_{0.5}Ca_{1.5}MnO_4$ *using the Bmab space group.*

Parameters	343 K	293 K	40 K
a (Å)	5.3798(23)	5.3760(28)	5.3764(01)
b (Å)	5.4046(10)	5.4107(57)	5.4219(64)
c (Å)	11.8298(21)	11.8301(90)	11.8096(69)
χ^2	5.901	8.091	0.03774
W_{rp}	0.4674	0.0386	0.0084
R_p	0.3417	0.0248	0.0061
Atomic positions			
Mn (0,0,0)			
Pr/Ca (0,0,z)	z = 0.3563(53)	z = 0.3572(32)	z = 0.3558(59)
O1 (x,y,z)	x = 0.25	x = 0.25	x = 0.25
	y = 0.25	y = 0.25	y = 0.25
	z = 1. 0202(64)	z = 1.0086(15)	z = 1.0184(51)
O2 (0,y,z)	y = 0.9820(87)	y = 0.0372(22)	y = 0.9494(62)
	z = 0.1710(59)	z = 0.1679(06)	z = 0.1744(03)

cell volume, and the degree of orthorhombicity. All of these structural parameters show pronounced changes across CO-OO transition. A non-monotonic change also occurs around the antiferromagnetic transition at T_N, indicating a strong coupling of the charges and spins to the lattice. Those observation are also supported by the temperature dependent variations of the Mn-O bond lengths and O-Mn-O bond angles obtained from the Rietveld analysis of the powder XRD data, as shown in Fig. 4.7. In this figure, O_1 and O_2 are the oxygens occupying the in plane and apical oxygen ions, respectively. The apical oxygen is more sensitive to the CO-OO phase transition, leading to the peculiar temperature dependent variations of the Mn-O_2 bond length and in particular the O_1-Mn-O_2 bond angle around T_{CO-OO}, as depicted in Fig. 4.7 (b) and (d). There is also a clear anomaly around AFM phase transition. These structural changes will be further discussed in the section on Raman spectroscopy.

4.4 Magnetic Properties

The temperature dependent magnetization was measured using a Quantum Design MPMS XL SQUID magnetometer. A 40 mg sample was placed in a gelatin capsule filled with cotton to avoid sample rotation during the measurement. The magnetization measurement was performed in both zero field cooled (ZFC) and

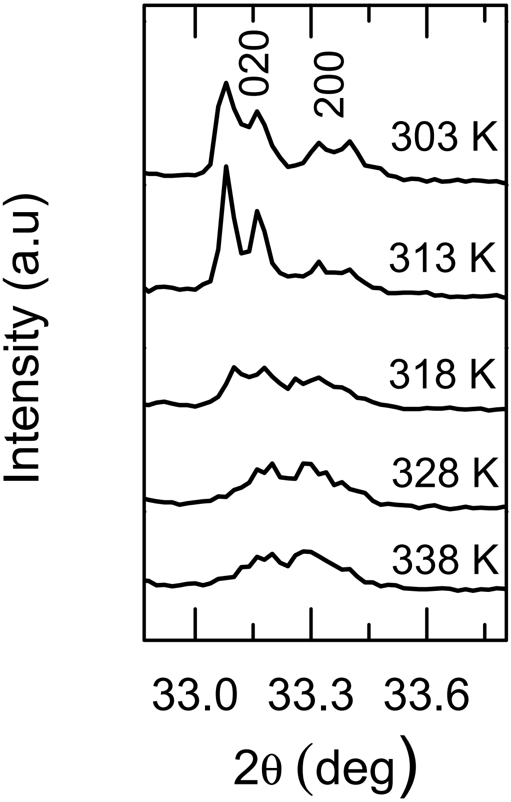

Figure 4.5: *The evolution of the 020 and 200 peaks as recorded using a Bruker-D8 Advanced Diffractometer as temperatures varies from 303 K to 338 K leading to clear split at lower temperature. The doubling of the individual (020) and (002) peaks are due to imperfect spectral filtering of the Cu-*K_α *radiation*

field cooled (FC) modes from 5 K to 340 K, in external magnetic fields of 0.1 T applied separately along the *a*, *b*, and *c* axes.

The result is displayed in Fig. 4.8 in terms of the associated magnetic susceptibility. There are no differences observed for the ZFC and FC measurement. An anisotropic behavior of the magnetic susceptibility is clearly observed along different crystallographic directions. Apart from that, the magnetic susceptibility of $Pr_{0.5}Ca_{1.5}MnO_4$ shows generally three main features: 1) a sudden upturn at 320 K, 2) a broad maximum around 200 K, and 3) a sudden drop at 127 K along the *a*- and *b*-axis while a sudden rise along the *c* below T_N. These features are even more clearly exhibited in the derivative curves of magnetic susceptibility showing clear peaks at 320 K and 127 K as seen in the inset. A relative weak kink around

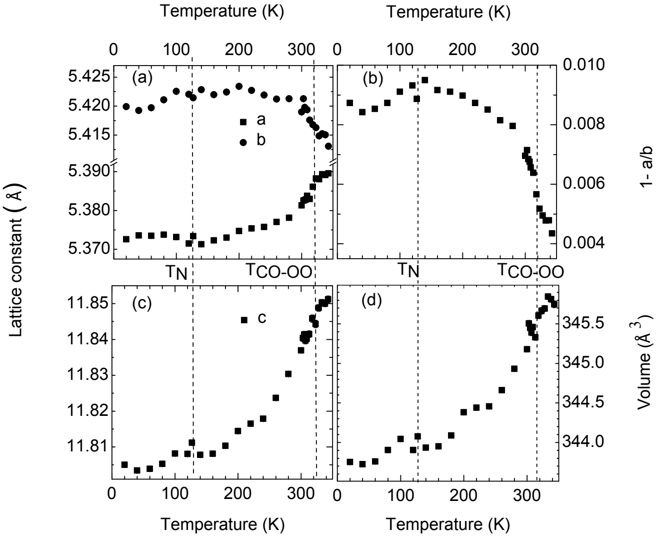

Figure 4.6: *The temperature dependence of the lattice constants along the a and b axes, (panel (a)) together with the orthorhombicity 1-a/b (panel (b)). The temperature dependence of the lattice constant along the c axis and the total unit cell volume are shown in panels (c) and (d), respectively.*

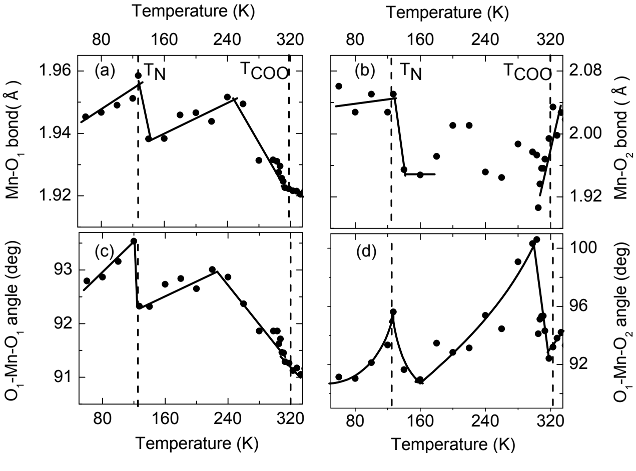

Figure 4.7: *The temperature dependence of the (a) Mn-O_1 bond length, (b) Mn-O_2 bond length, (c) O_1-Mn-O_1 bond angle, and the (d) O_1-Mn-O_2 bond angle. The O_1 and O_2 ions are in-plane and apical oxygen ions, respectively. The solid lines are guides to the eyes*

127 K is also observed along the *c*-axis.

The sudden change observed at 320 K is supposed to signify a change in the magnetic correlations at the CO-OO transition. This observation was already

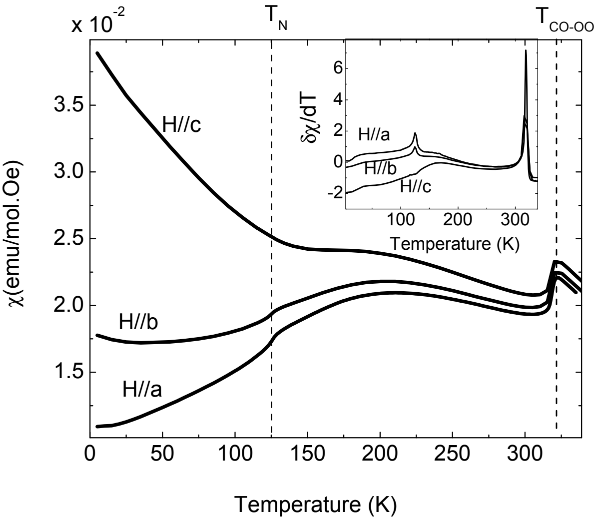

Figure 4.8: *The temperature dependence of the magnetic susceptibility along the a, b, and c axis measured in 0.1 T external magnetic field. The insert shows the derivative of magnetic susceptibility.*

reported in neutron diffraction measurement in $La_{0.5}Sr_{1.5}MnO_4$ where the CO-OO transition was marked by the increasing area with AFM fluctuation in place of the presence of magnetic domains with FM correlation [20]. Further broad maximum centered around 200 K observed in the magnetic susceptibility are also in agreement with the result of a neutron diffraction study in $Pr_{0.5}Ca_{1.5}MnO_4$, which shows the presence of short range 2D AFM correlations within the MnO_2 plane at about the same temperature [6]. This 2D AFM correlation has been suggested as a result of fluctuation induced by a competition between AFM and FM [20]. The transition at 127 K was also found in the neutron diffraction experiment and attributed to 3D AFM order with CE-type ordering [6]. The reason for anisotropic properties, particularly the increasing magnetic susceptibility along *c*-axis, is not clear at present. However, the paramagnetic contribution of rare earth has been proposed to induce anisotropic properties in several manganite [21]. Besides, the increase of magnetic susceptibility along *c*-axis might also be due to spin canting, although neutron diffraction analysis has concluded that the angle of spin canting is very small [22]. Finally, our data suggest that the Pr ion ordering might also be responsible for small kink in magnetic susceptibility below 40 K.

4.5 Transport Properties

The temperature dependent resistivity of $Pr_{0.5}Ca_{1.5}MnO_4$ was measured using the four probe method. Detail of experiment was already explained in Chapter

2. The result are plotted as ρ versus T and $\ln(\rho)$ versus $1/T^{1/3}$ in Fig. 4.9. The monotonous increase of resistivity with decreasing temperature clearly testifies that the system is not truly metallic even above T_{CO-OO} . A rather abrupt change of resistivity is nevertheless observed at 320 K, marking the onset of CO-OO-insulating state and confirming the results of a previous study[7]. It is followed by a nonlinear gradual increase of the resistivity upon decreasing temperature. The resistivity below 127 K can not be determined precisely due to the limitation of the observation. A monotonously increase of resistivity below AFM transition has been reported in Ref. [7].

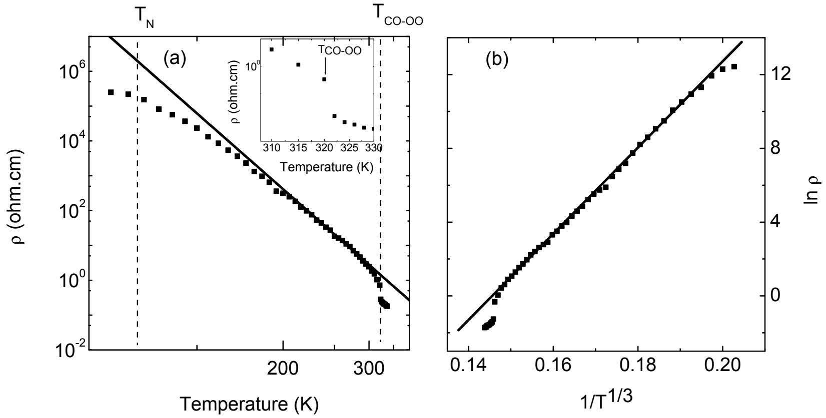

Figure 4.9: *(a) Temperature dependent resistivity of* $Pr_{0.5}Ca_{1.5}MnO_4$ *measured along the a direction. The solid line is a fit of an Arrhenius-type law to the data. The inset shows the abrupt jump of resistivity at the CO-OO transition. (b) ln(ρ) versus* $1/T^{1/3}$ *plot. The solid line through the data is a fit to a variable range hopping transport model in the CO-OO phase.*

The nonlinear variation of the resistivity in the temperature range of 127 K<T<320 K could possibly be explained by a model of activated transport. However, as shown by the solid line in Fig. 4.9 (a), an Arrhenius-like behavior, $\rho(T) = \rho_0 exp(E_0/k_B T)$, with ρ denoting the high temperature limit resistivity and E_0 representing the temperature independent activation energy, does not fit the data very well.

Since charges in charge ordered phase are expected to be more localized on the Mn sites, one might expect that a variable range hopping (VRH) model would provide a better description of the temperature dependence of the conductivity. The temperature dependence for this model is given by [23]:

$$\rho(T) = \rho_{min} exp[(T_{min}/T)^{1/(1+d)}], \tag{4.1}$$

where ρ_{min} and d are the high temperature limit resistivity and the dimensionality of the system, respectively. T_{min} is the characteristic temperature related to the density of the localized states in the vicinity of the Fermi level ($N(E_F)$) and the localization length (ζ), given approximately by $k_BT_{min} \approx 1/k_BN(E_F)\zeta^3$

The best fit using the VRH model for a 2D system (d=2) shows a good agreement with our experimental data (see Fig. 4.9 (b)), with the fitting parameters of $\rho_{min} = 2 \times 10^{-15}$ ohm·cm and $T_{min}^{1/3} = 232$ K (19 meV). Since the 1D (d=1) and 3D (d=3) variants of Eq.4.1 do not fit our experimental data well, we conclude that, as expected, the VRH transport primarily takes place within the ab-plane and $T_{min}^{1/3}$ is proportional to the localization length which is in the order of Mn-Mn distances and is expected to be of the order of lattice constants along the a and b axes that are shown to vary rather sharply with temperature around T_{CO-OO} as seen in Fig. 4.6 (a)). This suggests then that the abrupt change in the conductivity along a-axis at the CO-OO transition is intimately related to the abrupt change of the corresponding lattice parameter.

4.6 Specific Heat

The temperature dependent variation of specific heat was measured using a Quantum Design 9T PPMS (physical property measurement system). The sample was mounted on the platform using Apiezon N grease. The temperature was varied step wise from 5 up to 340 K with a step rise of 5 K. The background contribution was subtracted based on data correction provided automatically by the system. However, the obtained value is higher than the expected Dulong Petit limit of *3R* J/molK per atom where R is the gas constant. We corrected our result by subtracting all data with a constant value as to match the resulted specific heat at high temperature with the Dulong Petit limit of 175 J/molK.

The resulting specific curve is presented in Fig. 4.10. The phase transition from the disordered to the charge-orbital ordered state is marked by a sharp peak at 320K indicating the entropy release accompanying this transition. The specific heat in the low temperature regime appears to be dominated by phonon contributions without any observable anomaly at the AFM transition at $T = 127$ K . The absence of entropy release at this temperature suggests that the formation of short range AFM order already takes place at temperatures well above the AFM ordering temperature [20]. A small and broad excess of specific heat appearing around 280 K (indicated by an * symbol in Fig. 4.10) is due to the contribution from the Apiezon N grease [24].

In order to analyze the optical phonon contribution, the experimental data is fitted with Einstein equation for specific heat, which is written as follows

$$C = Nk_B \sum_{i=1}^{n} \left[\frac{\hbar\omega_i}{k_BT}\right]^2 \frac{exp\,(\hbar\omega_i/k_BT)}{\left[exp(\frac{\hbar\omega_i}{k_BT}) - 1\right]^2}, \tag{4.2}$$

where N, ω, and n are the number of atoms in the system, the optical phonon frequency, and the number of phonons contributing to specific heat, respectively.

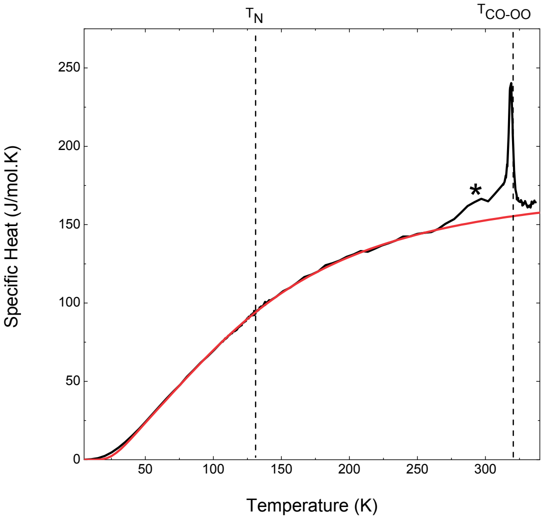

Figure 4.10: *Temperature dependent specific heat of* $Pr_{0.5}Ca_{1.5}MnO_4$*. The red curve is the best fit of Einstein model to the data taking into account the optical phonon modes at wave number of 120* cm^{-1}*, 302* cm^{-1}*, and 370* cm^{-1}*.*

The best fit of the Einstein model to our experimental data is presented as the red curve in Fig. 4.10. It is obtained by summing the contribution of three optical phonon at wave number 120 cm^{-1}, 302 cm^{-1}, and 370 cm^{-1}. These phonon frequencies are close to the optical phonon frequencies observed in Raman spectroscopy (see also next section) and are attributed to the oxygen-Pr/Ca vibration, octahedral rotation around the y axis, and octahedral rotation around the x axis, respectively [25].

The critical behavior around the CO-OO transition is most clearly displayed in Fig. 4.11, which presents the specific heat data of Fig.4.10 after subtraction of the phonon contributions. The excess of specific heat (C_{exc}) around the CO transition shows a good agreement with a critical behavior given by $|1 - T/T_{CO-OO}|^{\alpha}$, with $\alpha = -0.725$ (solid lines in the figure). This value suggests a 3D nature of the CO-OO in this layered manganite system, in agreement with the findings of Onoda *et al.* [26]. The excess of specific heat in logarithmic scale and its fit with critical exponent function is also shown in the inset of Fig. 4.11 (a). In addition, Fig. 4.11 (b) shows the corresponding change of entropy which is numerically calculated from the integration of C_{exc}/T curve around CO-OO transition. The change of entropy is about 3.2 J/molK. This value is not far from the entropy typically found in perovskite manganites which ranges from about 2 up to 4 J/molK [27, 28]. In our experiment, the background contribution might be not perfectly be subtracted so that the value of entropy can be overestimated.

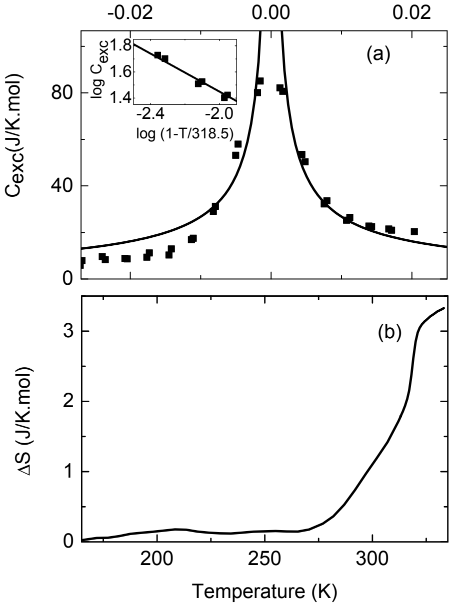

Figure 4.11: *(a) The excess specific heat around the CO -OO phase transition. Solid lines are the best fit with critical exponent expression given in the text. Inset is the plot in logarithmic scale. (b) The entropy change accompanying the CO transition at* T_{CO-OO}

4.7 Vibrational Properties

The anomalous behavior of Raman spectra have been suggested as signatures of the appearance of certain orderings in manganite [17, 29]. For instance, several Raman peaks have been observed to be more pronounced below CO-OO transition temperature. On the other hand, the AFM ordering has been marked by the softening of certain phonon modes. Unlike the perovskite systems, Raman study in single layer compound, particularly the distorted one, is relatively rare. In addition, the temperature dependent phonon behaviors reported so far have not been completely analyzed. Several questions remain open regarding the effect of distortion, the dimensionality, as well as electron-phonon coupling and and spin-lattice coupling.

In this study the correlation between the phonons and the ordering of charge, orbital occupation, and spin in distorted single layered manganite $Pr_{0.5}Ca_{1.5}MnO_4$ are studied by performing temperature dependent Raman spectroscopy measurement on the *ab*-plane of naturally cleaved single crystal $Pr_{0.5}Ca_{1.5}MnO_4$ sample. For this experiment, a continuous wave laser (532 nm) with power density of 0.5 W/cm^2 was used for excitation source. The temperature dependent polarized Raman spectra were recorded using a Jobin Yvon T64000 micro-Raman spectrometer in a cold finger Oxford microstat. The experiment was performed in the back scattering mode with $c(aa)\bar{c}$ and $c(ba)\bar{c}$ configuration and the wave number ranging from 35 to 615 cm^{-1}. The quantitative analyses of phonon behaviors in each phase are performed for the elucidation of the underlying role of charge-lattice coupling, orbital fluctuation on lattice dynamics, and spin-lattice coupling. The detailed experiment set up and configuration is described in Chapter 2.

4.7.1 The Raman Spectra

Figure 4.12 shows temperature dependent the Raman spectrum between 100 K and 350 K. For the $c(aa)\bar{c}$ configuration, a broad mode, centered at 554 cm^{-1}, as well as weaker features at 70, 180, and 210 cm^{-1} are observed above CO-OO phase transition. For the $c(ba)\bar{c}$ configuration, the broad mode centered at 554 cm^{-1} is also observed together with four other peaks at 80, 120,180, and 205 cm^{-1} above T_{CO-OO}. Upon lowering the temperature, the intensity of the 554 cm^{-1} mode increases, its frequency shifts to higher values, and the line width becomes more narrow. Several new peaks become observable below the CO-OO phase transition. New Raman modes are observed at 443, 408, 366, 314, 224, 100, 57 cm^{-1} for the $c(aa)\bar{c}$ configuration whereas new Raman modes of 448, 405, 366, 309, 210, 99, 76 cm^{-1} are observed for the $c(ba)\bar{c}$ configuration. Overall, below the CO-OO transition temperature the number of Raman modes is 9 for $c(aa)\bar{c}$, and 10 for $c(ba)\bar{c}$ configuration. The observed Raman modes and their assignments [25, 30] are given in Table 4.2.

In section 4.3, the space group of Bmab is shown to be compatible with the X-ray diffraction data. Using this space group, a total of 24 modes are expected to be Raman active for $\mathrm{Pr}_{0.5}\mathrm{Ca}_{1.5}\mathrm{MnO}_4$ with a decomposition into the symmetry modes according to $7A_g + 5B_{1g} + 4B_{2g} + 8B_{3g}$. Among those, only the A_g and B_{2g} modes are the modes accessible in our experiment: A_g are active in $c(aa)\bar{c}$ configuration, while B_{2g} in $c(ba)\bar{c}$ configuration. The other modes are only accessible in configurations which include a polarization along the c-axis, which is not included in our experiment. The full appearance of Raman modes above T_{CO-OO} is compatible with the number of active Raman modes deduced from Bmab space group. However, this changes T_{CO-OO} where we observe 9 A_g for $c(aa)\bar{c}$ and 10 B_{2g} modes in $c(ba)\bar{c}$ configuration. This clearly indicates a lowering of the crystal symmetry below T_{CO-OO}, in line with the work of Okuyama et al. which based on found XRD data proposed the Pnma space group for $\mathrm{Eu}_{0.5}\mathrm{Ca}_{1.5}\mathrm{MnO4}$ below T_{CO-OO} [19]. According to the Pnma space group, one is expected to observe the active Raman modes consisting of $29A_g + 22B_{1g} + 29B_{2g} + 22B_{3g}$ [18]. These numbers are apparently much larger than the observed Raman active modes in our experiment.

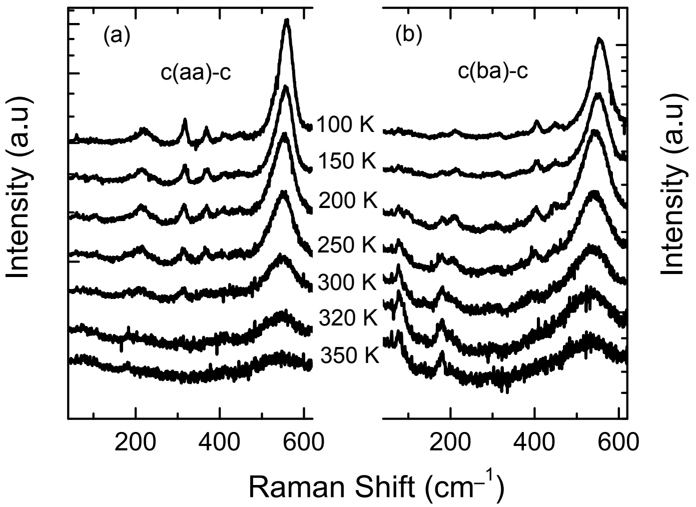

Figure 4.12: *Temperature dependent Raman spectra of* $Pr_{0.5}Ca_{1.5}MnO_4$ *in (a) c(aa)*$\bar{c}$ *configuration, and (b) c(ba)*$\bar{c}$ *configuration. For clarity, the intensities have been multiplied 50 times, shifted vertically, and presented in logarithmic scale.*

4.7.2 Temperature Dependent Raman Modes

In order to get quantitative information on the temperature dependent the Raman modes, our experimental data are fitted with the Lorentzian response functions given below:

$$I(\omega) = \sum_{i=1}^{n} \frac{a_i \sigma_i}{(\omega - \omega_i)^2 + \sigma_i^2} \tag{4.3}$$

Before fitting, we subtracted a constant background from our data and performed a Bose-Einstein thermal factor correction. From the best fit of Eq. 4.3 to our data we obtain for each mode i the scattering strength a_i, the mode frequency ω_i, and the linewidth σ_i (2σ is the full width at half maximum (FWHM)).

In order to highlight the effects of CO-OO and AFM order on the local lattice dynamics, the temperature dependence of selected Raman modes are investigated. Specifically, we focus on the stretching-Q2 Jahn Teller mode at 555 cm^{-1}, the out of phase bending mode at 448 cm^{-1}, the rotation mode at 366 cm^{-1}, and the tilting modes at 212 cm^{-1} and 180 cm^{-1}, as illustrated in Fig. 4.13.

In magnetic material, the change of phonon frequency arises from several mechanisms which can be written as [29].

$$\omega(T) - \omega(T_0) \equiv \Delta\omega(T) = (\Delta\omega)_{latt} + (\Delta\omega)_{anh} + (\Delta\omega)_{ren} + (\Delta\omega)_{s-ph} \tag{4.4}$$

Table 4.2: *Raman Modes in* $Pr_{0.5}Ca_{1.5}MnO_4$ *and their Assignments.*

T	$c(aa)\bar{c}$		$c(ba)\bar{c}$	
	v (cm^{-1})	Assignment	v (cm^{-1})	Assignment
>320 K	70	oxygen vibration toward Pr/Ca	80	oxygen vibration toward Pr/Ca
			120	oxygen vibration toward Pr/Ca
	180	tilting mode	180	tilting mode
	210	tilting mode	205	tilting mode
	554	JT stretching	554	JT stretching
<320 K	57		76	oxygen vibration toward Pr/Ca
	100	oxygen vibration toward Pr/Ca	99	oxygen vibration toward Pr/Ca
			120	oxygen vibration toward Pr/Ca
	180	A$_g$, tilting mode	182	B$_{2g}$, tilting mode
	224	A$_g$ tilting mode	212	B$_{2g}$ tilting mode
	314	A$_g$ oxygen vibration toward Pr/Ca along x axis	309	B$_{2g}$ octahedral rotation around y axis
	366	A$_g$ octahedral rotation around x axis	366	
	416	A$_g$	405	B$_{2g}$, bending mode
	447	A$_g$ bending mode	448	B$_{2g}$, bending mode
	556	A$_g$ in-phase JT stretching mode	556	B$_{2g}$ in-phase JT stretching mode

The first term on the right-hand side is a contribution due to the change of ionic binding energy arising from the lattice expansion/contraction. It is usually approximated by the Grüneisen law, $(\Delta\omega/\omega)_{latt} \propto \gamma\Delta V/V$, where $\Delta V/V$ denotes relative change of unt cell and γ is the Grüneisen parameter. The second term is the contribution of intrinsic lattice giving rise to frequency shifts at constant volume. The changes of frequency and the line width are expressed by Eqs. 4.5 and 4.6, respectively [31].

$$\omega(T) = \omega(T_0) - A\left[1 + \frac{2}{exp(\hbar\omega(T_0)/2k_BT) - 1}\right]$$
$$- B\left[1 + \frac{3}{exp(\hbar\omega(T_0)/3k_BT) - 1} + \frac{3}{(exp(\hbar\omega(T_0)/3k_BT) - 1)^2}\right] \tag{4.5}$$

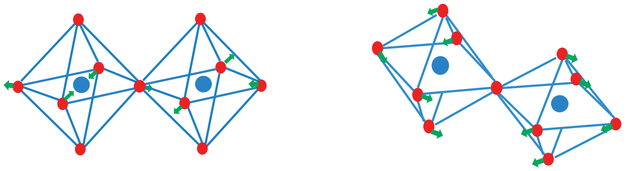

JT stretching mode
at 555 cm^{-1}

Bending mode
at 448 cm^{-1}

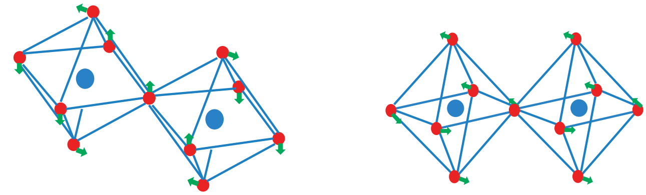

Rotation around *x* axis mode
at 366 cm^{-1}

Tilting mode at 210 cm^{-1}

Figure 4.13: *The octahedral distortions associated with the octahedral stretching, bending, rotation, and tilting modes.*

$$\begin{aligned}\sigma(T) =& C\left[1+\frac{2}{exp(\hbar\omega(T_0)/2k_BT)-1}\right]\\ &+D\left[1+\frac{3}{exp(\hbar\omega(T_0)/3k_BT)-1}+\frac{3}{(exp(\hbar\omega(T_0)/3k_BT)-1)^2}\right]\end{aligned} \tag{4.6}$$

In this case, the optical phonon decay into lower frequency phonons. As a consequence, the optical phonon frequency is shifted with temperature accroding to Eq. 4.5, and the phonon line width is thermally broadened as formulated in Eq. 4.6. In Eqs. 4.5 and 4.6, A and C are constant parameters for three phonon process where one optical phonon decays into two identical phonons whereas B and D are for four phonon processes where one phonon decay into three identical phonons. The term $\omega(T_0)$ is the phonon frequency at $T = 0$ K and k_B is the Boltzmann constant.

The third term in Eq. 4.4 is to accommodate the phonon change due to renormalization of the electronic states that may occur near the spin ordering temperature while the fourth term is due to spin-phonon coupling which might influence lattice vibrations across spin order transition. In a molecular field approximation, the phonon frequency deviation due to magnetic order is given by equation 4.7 [29]

$$(\Delta\omega(T))_{spin-phonon} \approx \frac{1}{m\omega(T)}\frac{\partial^2 J}{\partial u^2}\langle S_iS_j\rangle \approx \frac{1}{m\omega(T)}\frac{\partial^2 J}{\partial u^2}\left[\frac{M(T)}{4\mu}\right]^2 \tag{4.7}$$

The spin-phonon coupling is inversely proportional to the mass of magnetic ion (m), the respective normal phonon frequency ($\omega(T)$), and directly proportional to the change of magnetic exchange constant with respect to the magnetic ion coordinates ($\frac{\partial^2 J}{\partial u^2}$) [29]. The spin coupling strength, $\langle S_i S_j \rangle$, is proportional to the square of magnetization ($M(T)^2$) and scales with the temperature ($M(T)^2 \approx [1 - T/T_N]^\nu$) so that Eq. 4.7 can be written as [32]

$$(\Delta\omega(T))_{spin-phonon} \approx F\,[1 - T/T_N]^\nu \tag{4.8}$$

where F is the spin-phonon coupling strength. Eq. 4.8 might also be extended to other cases such as the influence of charge order on the lattice dynamics. In such cases, F and T_N are replaced by the respective interaction, *e.g.* the charge-lattice coupling and the correspond transition temperature, respectively.

To obtain the general characteristics of temperature dependent phonon evolution, the anharmonic model given by Eqs. 4.5 and 4.6 are fitted to the temperature dependence of the frequencies and the line widths of the selected Raman modes as explained separately in the following subsection. The obtained fitting parameters are given in Table 4.3.

The Stretching Mode

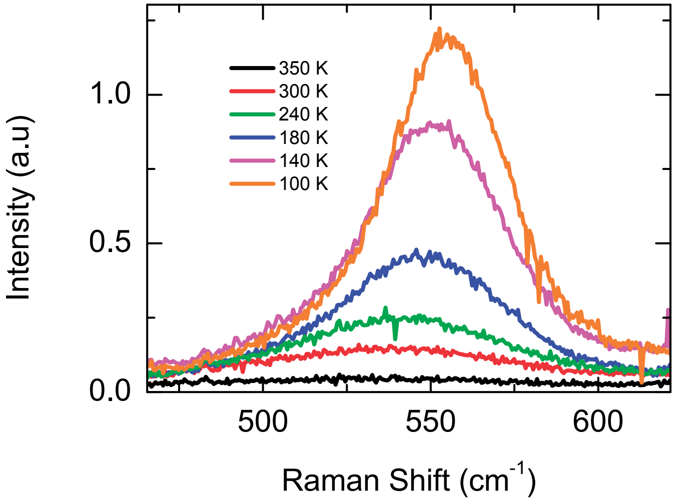

Figure 4.14: *The temperature dependence of 555 cm^{-1} mode.*

The mode at 555 cm^{-1} is associated with a stretching of the oxygen octahedra in the *ab*-plane , namely the Q2 JT distortion [17, 25]. Figure 4.14 shows that upon cooling, the intensity and the frequency of this mode increase whereas the line width decreases. The temperature dependent frequency and line width of 555 cm^{-1} mode obtained from fit of the Eq. 4.3 to the Raman spectra of Fig. 4.14 are shown in Fig. 4.15. The temperature dependent frequency shows a small kink around 200 K separating two different temperature regimes. The three phonon process in Eq.4.5 can only fit to the low temperature data (100 K$< T <$200 K) while four phonon processes can only fit to the high temperature data (200 K$< T <$360 K). The fitting results are shown as blue and red lines in Fig. 4.15 (a). The obtained fitting parameters are shown in Table 4.3. The intersection of the low and high temperature regime fits lies at 215 K which is in good agreement with the broad maximum in magnetic susceptibility data. This finding indicates that the 2D short range AFM correlations change the phonon decay channels. Though less clear, also the linewidth shows an anomaly around 215 K, as is shown in Figure 4.15 (b) which displays the temperature dependence of the line width together with fits of Eq. 4.6. The result suggests that the phonon decay is dominated by four phonon process where one optical phonon with a frequency of 555 cm^{-1} decays into three phonons, each with frequency about 187 cm^{-1}. This frequency is also observed in this experiment.

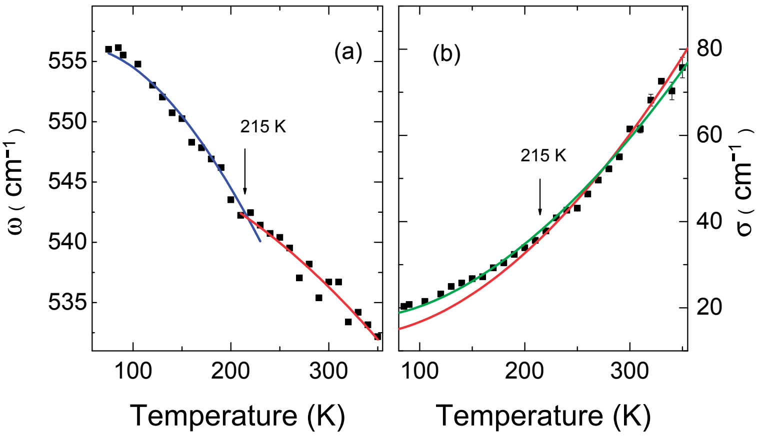

Figure 4.15: *The temperature dependence of (a) the frequency and (b) line width of the 555 cm^{-1} mode showing an anomaly near 215 K. The blue and red lines are fits assuming predominantly three and four phonon processes, respectively, while the green line represents both three and four phonon process contributions over the whole temperature regime.*

The Bending Mode

Figure 4.16 shows temperature dependent Raman spectra in the vicinity of the 448 cm^{-1} bending mode in a *c(ba)*$\bar{c}$ configuration. Close to the 448 cm^{-1} mode, there is another mode at 405 cm^{-1} which has been assigned to an oxygen Pr/Ca vibration [25]. Their intensities decrease with increasing temperature and vanish above 300 K. Similar modes with smaller intensities are also observed in the *c(aa)$\bar{c}$* configuration, most likely due to polarization leakage.

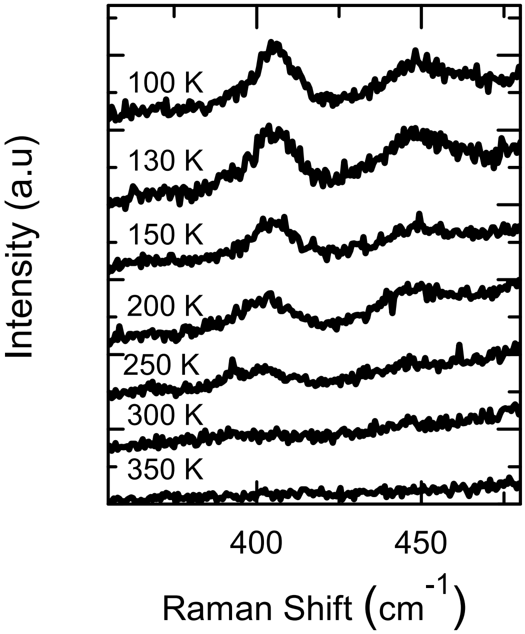

Figure 4.16: *The bending mode (448 cm^{-1}) and oxygen Pr/Ca mode (405 cm^{-1}) observed in c(ba)$\bar{c}$ configuration at temperatures from 350 K down to 100 K.*

Figures 4.17 (a) and (b) show the temperature dependence of the frequency and line width of the 448 cm^{-1} mode, respectively. The frequency can be fitted assuming predominantly three phonon processes with fitting parameters as listed in Table 4.3. On the other hand, the temperature dependence of the line width cannot be fitted to the anharmonic model. It is shown in Fig. 4.17 (b) that the line width tends to increase linearly above 200 K. An anomaly with onset around 200 K and peak around 140 K might be associated with magnetic fluctuations of 2D AFM short range interaction at 200 $K < T <$ 320 K and 3D AFM long range interaction below T_N.

Figures 4.17 (c) and (d) show the temperature dependence of the frequency and line width of the 405 cm^{-1} mode, respectively. The anharmonic model is well fitted to the frequency above 140 K whereas the line width can only be fitted above 200 K. The obtained parameters are listed in table 4.3. A small deviation of the frequency from the anharmonic behavior is observed below 140 K which might be related to fluctuations of the 3D AFM long range interaction. Fig. 4.18 shows the deviation as obtained by subtracting the anharmonic fitting result from the experimental data. It increases with the temperature decreasing below 140 K, and

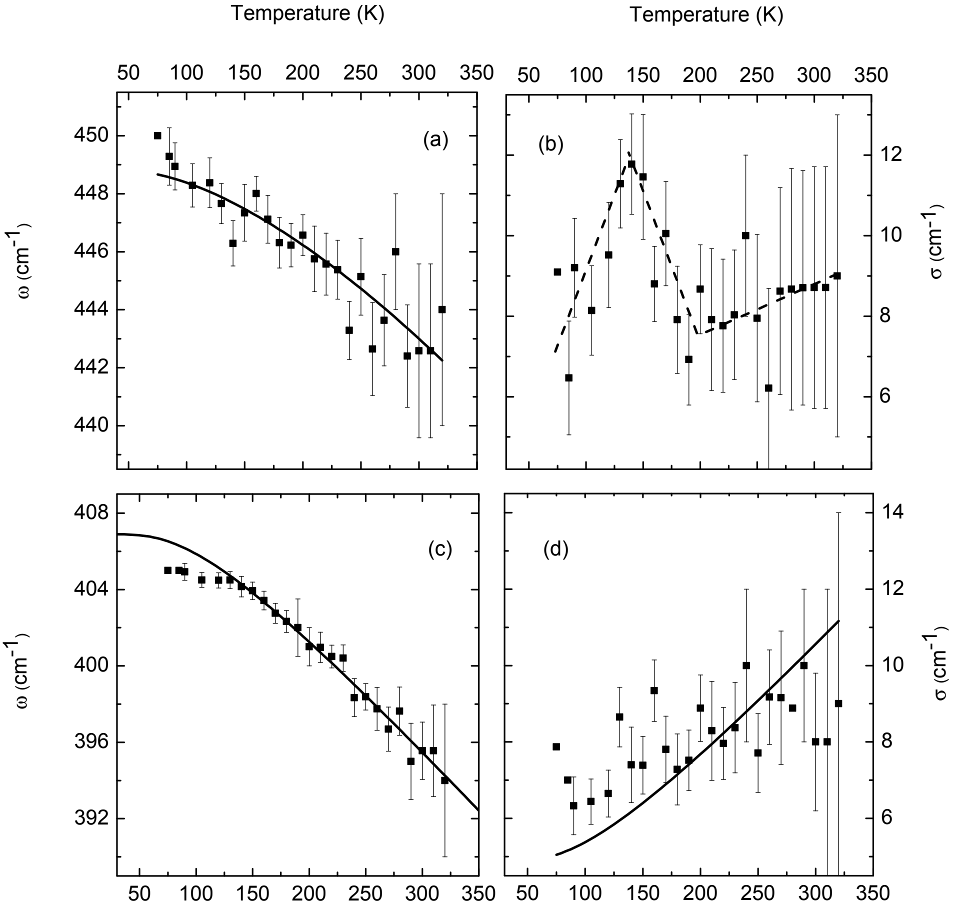

Figure 4.17: *The temperature dependence of the frequency (left panels) and line width (right panels) of the 448 (top) and 405 cm^{-1} modes (bottom). Solid lines are fits to the anharmonic model whereas the dashed lines are a guide to the eye.*

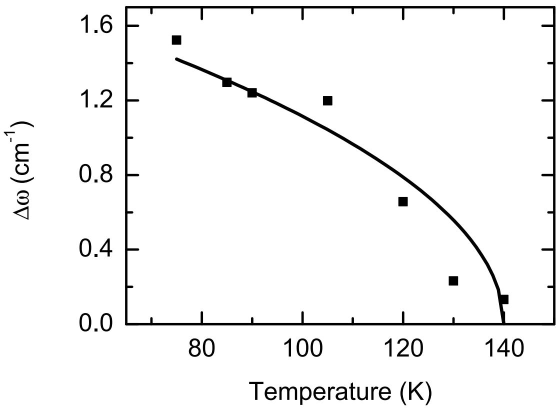

Figure 4.18: *The deviation of the frequency of the 405 cm^{-1} mode from the anharmonic model below the AFM order transition. The solid line is a fit of Eq. 4.8*

Eq. 4.8 is well fitted to the data with spin lattice coupling F of 2.1 cm^{-1} and a critical exponent constant β of 0.5. A deviation of linewidth below 200 K might also be attributed to the 2D AFM short range order fluctuations. The sensitivity of this mode to the spin changes suggests that this mode is a bending mode, not a vibration of Pr/Ca toward the oxygen ion as previously suggested.

The Rotation Mode

Figure 4.19 (a) shows the temperature evolution of the mode at 366 cm^{-1} in $c(aa)\bar{c}$ configuration which is assigned to the rotation of the oxygen octahedra around the a-axis [25]. This mode appears below 320 K and its intensity further increases upon decreasing temperature. As shown in Fig. 4.19 (b), a "mean field" approximation of $G(1-T/T_{CO})^{0.5}$ is well fitted to the integrated intensity around the CO transition, with a charge-lattice coupling G of 0.58 cm^{-1}. The experimental data start to deviate from the "mean field" approximation below 200 K suggesting the presence of a magnetic degree of freedom which induces an additional type of fluctuations.

The temperature dependence of the frequency and line width are shown in Figs. 4.20 (a) and (b), respectively. The increasing intensity is accompanied by a shift in the frequency to higher values and narrowing of the line width. The Raman frequency hardens by up to 4 cm^{-1} with temperature lowering down to T_N. It is interesting to note that upon cooling below T_N the frequency softens again by 2 cm^{-1} . The anharmonic model fits to the data assuming predominantly three phonon processes with fitting parameters as given in table 4.3 is shown by red lines in Fig. 4.20. A small anomaly is observed around the CO-OO transition. In order to capture the effect of the magnetic transition, the frequency softening is

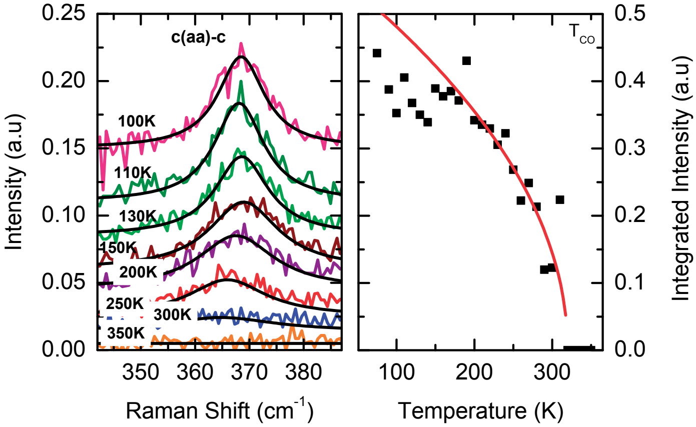

Figure 4.19: *Temperature dependent evolution of 366 cm^{-1} mode measured in c(aa)$\bar{c}$ configuration. (b) Integrated intensity (dots) and the mean field approximation fit (line)*

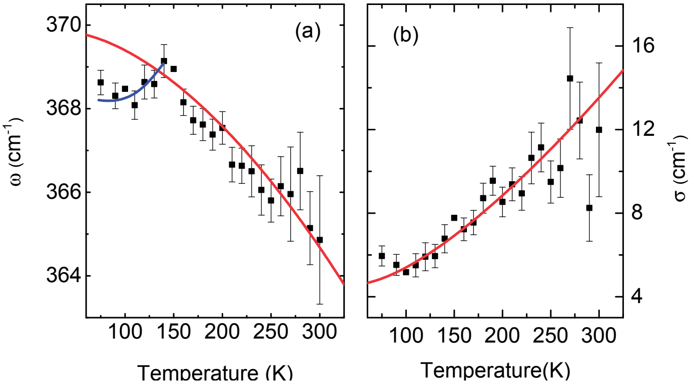

Figure 4.20: *Temperature dependence of frequency and line width of 366 cm^{-1} mode measured in c(aa)$\bar{c}$ configuration. The red lines are the anharmonic model fit to the experimental data, the blue line is a guide to the eyes.*

accentuated by subtracting the anharmonic model from the temperature dependence of frequency below 140 K. The result is shown in Fig. 4.21. A fit using Eq. 4.8 yields a spin lattice coupling F of 2.6 cm^{-1} and a critical exponents ν of 0.5.

The Tilting Mode

Figure 4.22 shows the temperature dependence of the tilting modes in PCMO observed in *c(ba)$\bar{c}$* configuration. Two modes labeled A and B are observed at 180 and 210 cm^{-1}, respectively, which show a different temperature dependence.

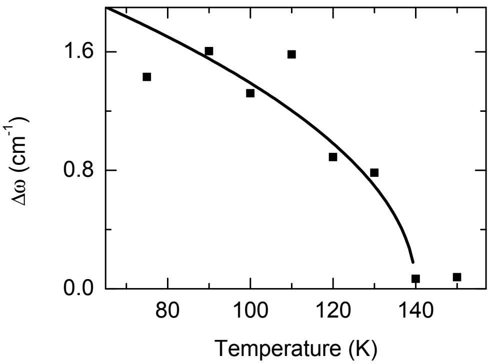

Figure 4.21: *The frequency deviation of the 366 cm^{-1} mode from the anharmonic model fit to experimental data. The solid line is a fit using Eq. 4.8.*

In order to clearly describe the relation between these modes, the ratio of the integrated intensities $I_{\mathrm{A}}/I_{\mathrm{B}}$ is shown in Fig. 4.22 (b). The data show clearly the presence of two distinct phase transitions: an abrupt increase of $I_{\mathrm{A}}/I_{\mathrm{B}}$ occurs around T_{CO-OO} while there is a change in the slope around T_N. This indicates that these modes are related to the change of the lattice constants.

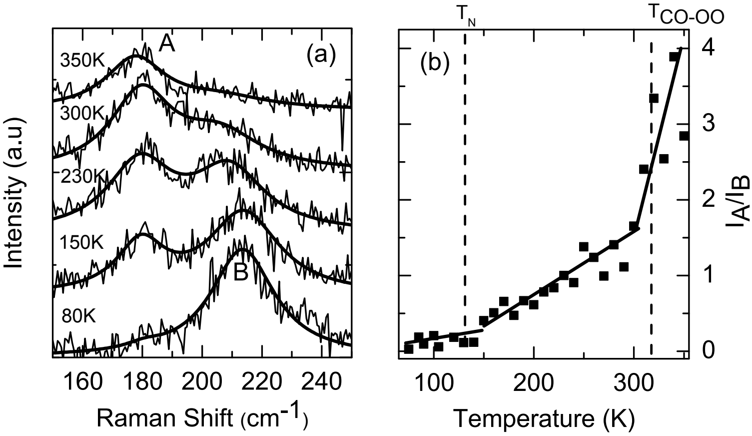

Figure 4.22: *(a) Temperature dependent evolution of the modes at 180 cm^{-1} (peak A) and 212 cm^{-1} (peak B) measured in c(ba)$\bar{c}$ configuration with their Lorentzian fits (smooth lines). (b) The temperature dependent ratio of the integrated intensities of peak A to peak B, I_A/I_B. Solid lines are guides to the eyes*

Figure 4.23 shows the temperature dependence of the frequency and line width of 180 cm^{-1} and 212 cm^{-1} modes. The frequency of the 212 cm^{-1} mode shows anomalies both at the CO-OO and AFM phase transitions. However, the line width decreases linearly with temperature down to 250 K and remains constant upon further cooling. The red lines are fits of anhamornic model to the experimental data with fitting parameters as given in Table 4.3. The softening of the frequency below the AFM transition indicates an influence of the magnetic order on the phonon while the relatively constant value of the line width below 250 K might indicate the suppression of charge and orbital fluctuations before the 3D AFM order appears. The Raman signal of the mode at 180 cm^{-1} does not show any significant anomalies as presented in Figs. 4.23 (c) and (d). The anharmonic model is well fitted to the temperature dependence of both frequency and line width. In order to accentuate the role of the spin-phonon coupling, Fig. 4.24 shows the deviation of the frequency of the mode at 212 cm^{-1} from the anharmonic fit. Eq. 4.8 is well fitted to the data using a spin-phonon coupling $F = 6.8$ cm^{-1} and a critical exponent constant $\nu = 0.57$.

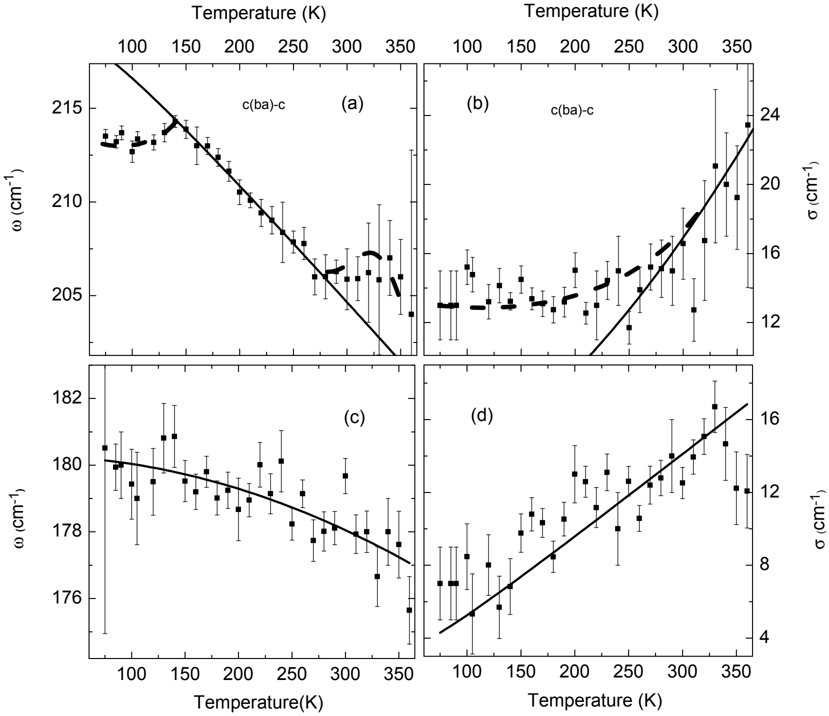

Figure 4.23: *Temperature dependence of the frequency (left panels) and line width (right panels) of 212 cm^{-1} (top) and 180 cm^{-1} modes (bottom). Solid lines are the anharmonic model fit to data, while dashed lines are guides to the eyes.*

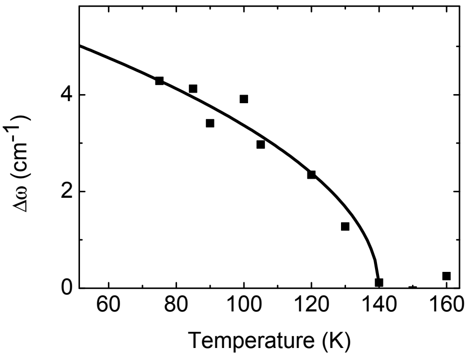

Figure 4.24: *The deviation of the frequency of the 212 cm$^-$1 mode from the fit to the anharmonic model. The solid line is a fit using Eq. 4.8.*

Table 4.3: *Fitting Parameters for Eq. 4.5 and 4.6*

Mode	ω_0 (cm^{-1})	A	B	C	D
JT Stretching					
- T < 200 K	571	8.7	6.3		
- T > 200 K	550	0	3.1	0	13.6
- 80<T<350 K	565			6.8	10.8
Octahedral Bending	452	2.57	0.58		
Oxygen vibration toward Pr/Ca	416.7	9.8	0	4.86	0
Octahedral rotation	370	0.6	0.53	4.1	0.4
Tilting Mode					
- 212 cm^{-1}	224	5.1	0.01	1.6	0.4
- 180 cm^{-1}	180.5	0.07	0.05	2.99	0

4.8 Discussion

Our temperature dependent Raman data reveal a number of concurrent and consistent signals of CO-OO transition at 320 K. These signals consist of the appearance of the rotation mode at 366 cm^{-1} around $T_{\text{CO-OO}} = 320$ K, the temperature dependence of its integrated intensity with a critical exponent $\nu = 0.5$ as well as the frequency change of the tilting mode (212 cm^{-1}) below 320 K and its apparent intensity transfer to the other tilting mode observed at 180 cm^{-1} upon increasing temperature. Especially note worthy is the rapid change of the ratio of the integrated intensities of these modes observed around T$_{CO-OO}$ indicating a corresponding rapid structural change. These Raman signals are closely correlated with the XRD data exhibiting abrupt change in the Mn-O bond lengths and Mn-O-Mn angles across this transition which clearly imply a strong charge-lattice coupling in the system at T_{CO-OO}. These finding support the result of previous studies on layered manganites which showed the relation between the CO-OO transition and an increase of the Mn-O bond length in the *ab* plane [33]. Below the CO-OO transition, the Mn - O bonds become unequal depending on the valence of the manganese ions Mn^{3+} and Mn^{4+}, respectively, constituting the charge ordered state. The effect of the symmetry breaking from $Mn^{3.5+}$-O-$Mn^{3.5+}$ into Mn^{3+}-O-Mn^{4+} bonds will create an unbalance in the rotation mode and consequently also the change in the Mn-O-Mn bond angles in the *ab*-plane as shown in Fig. 4.25. The good agreement between experimental data and a mean field fit suggests that the fluctuations of the rotation mode accompanying the COO transition are small enough to justify a "mean field" model. This finding is in agreement with previous studies in PCMO where the charge imbalance below the CO transition can be approximately described by a mean field model [34].

The CO-OO transition is expected to be accompanied by structural change. In $Pr_{0.5}Ca_{1.5}MnO_4$, the structural change is evidenced by evolution of Raman spectra as well as the change of [200] and [002] peaks in XRD data which suggest symmetry lowering with the decreasing temperature across T_{CO-OO}. Nevertheless, both the Bmab as well as Pnma space group are well fitted with the XRD data for the entire temperature. This unclear change of the structural symmetry at T_{CO-OO} might be due to the fluctuation of the oxygen positions around the Mn^{3+} and Mn^{4+}sites. The result is consistent with the monotonic change of the JT mode at 555 cm^{-1} across the T_{COO} which indicates that the orbitals are still fluctuating below the CO-OO transition. Even though this result is contradicted by neutron data which shows clear orbital order at T_{COO} [22], a recent optical conductivity study of this compound suggests the presence of orbital fluctuations at the manganese ions involving the oxygen orbitals [34]. The fluctuation of oxygen positions might also be a reason for the slightly different change in the Mn^{3+}-O and Mn^{4+}-O bond lengths accompanying the CO transition so that the rotation mode intensity can be approximated by mean field model.

The presence of charge order is also confirmed by the sudden jump in the electrical transport measurement. The analysis of the resistivity based on the concept of variable range hopping indicates charge localization. The inter-site hopping becomes less probable due to a longer distance between two nearest neighbors of Mn ions. The variable hopping analysis also suggests the 2D nature of charge transport in layered compounds.

The relation between magnetic properties and charge order is marked by a quite sharp upturn of susceptibility at T_{CO-OO}. The coincidence of this susceptibility change with the rapid change of the lattice parameters, the Mn-O bond lengths, and Mn-O-Mn angles suggests the relation between the magnetic properties and crystallographic structure. The changes of the Mn-Mn distances as well as the Mn-O-Mn angles induces a change of exchange energy. In case of very distorted system like the PCMO, this structural change is large enough to induce an enhancement of the AFM superexchange interaction. This AFM interaction competes with the FM

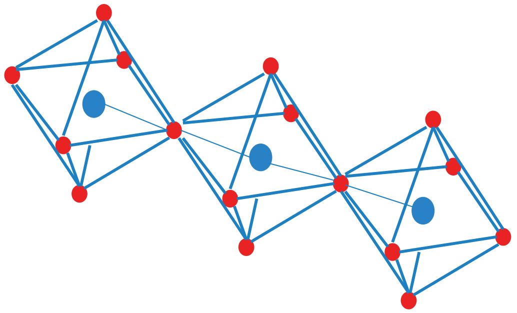

Symmetric Mn-O-Mn bonds above CO transition

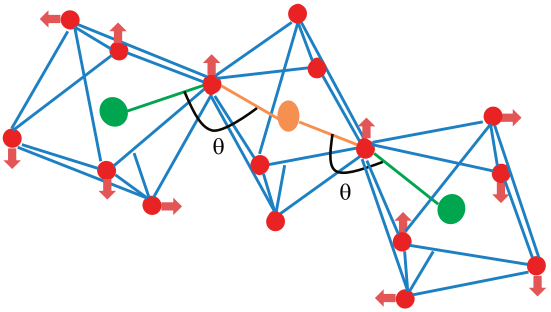

Asymmetric Mn-O-Mn bonds below CO transition

Figure 4.25: *The schematic picture of Mn-O bonds and Mn-O-Mn angles above the CO transition (upper panel) as well as the octahedral rotations and tilting angle (θ) below the CO transition (lower panel). The blue, green, and yellow circles represent* $Mn^{3.5+}$, Mn^{3+}, *and* Mn^{4+} *ions, respectively.*

fluctuations which yields a sharp jump in the magnetic susceptibility at the CO-OO transition. It is in contrast to less distorted systems like $La_{0.5}Sr_{1.5}MnO_4$ which the rapid change of lattice parameters is absent [12] and the anomaly in the magnetic susceptibility is less sharp [20].

The specific heat also shows a sharp peak accompanying the CO-OO transition. This effect is much stronger in layered compounds compared to the perovskite lattice structure [35, 36]. There is an evidence that the single layered system has stronger CO correlations than the perovskite structure as is also indicated by usually higher T_{CO-OO}. This might be related to the larger distance between neighbouring Mn ions in c direction so that the electron hopping along c direction is less probable in single layered systems thereby stabilizing the CO order in the ab plane. The analysis of the specific heat results in a value of the critical exponent α of 0.725 which is associated with the correlation constant ν of 0.63. Onoda et al. [26] have discussed that the decrease of ν is due to the unstable 2D nature of the charge order in layered manganites toward lattice distortion. The 3D nature of the charge order in single layered manganites is characterized by $\nu = 0.6$. This study suggests a 3D nature of the charge order in PCMO even though the CO correlations are stronger in the ab-plane than along the c-axis.

Below the charge ordering transition temperature, a broad maximum around 200 K was observed in the magnetic susceptibility which is generally accepted as a signature of the presence of 2D AFM short range correlations. In connection with this, a deviation from Arrhenius behavior in the resistivity is observed. The change of the frequency and line width of JT mode at 200 K also give evidence that the 2D short range AFM correlations are connected to the JT stretching mode. A large broadening of the line width above 200 K indicates the dominant contribution of four phonon processes where one phonon decays into three identical phonons. Considering the relation between JT distortions and the e_g orbitals of Mn^{3+}, the large broadening of the phonon mode is due to the fluctuations of the e_g orbital orientation when the temperature is approaching the CO-OO transition. The well match of the line width with a four phonon process model shows that the phonon life time is short when the orbital orientation is fluctuating. The smaller slope of the lattice parameters as well as relatively stable of Mn-O_1 bond lengths and O_1-Mn-O_1 angles at temperatures around 200 K might also indicate the stability of orbital. The coincidence of this orbital stability with 2D short range AFM correlations might suggest that the superexchange interaction is strong enough to induce 2D AFM short range ordering when the orbital ordering is settled. This finding does not agree with the results of neutron experiments where the orbital ordering is observed simultaneously to the charge order transition [16].

The magnetization data shows that the 3D long range AFM order occurs at 130 K. This transition is also marked by the changes of lattice constants which indicates a strong lattice-spin coupling below the magnetic transition. The changes in Mn-O bond lengths as well as the Mn-O-Mn angles at the magnetic transition correlate to the changes of the phonon modes such as the bending mode observed at 448 cm^{-1} and 405 cm^{-1}, the rotation mode around a axis at 336 cm^{-1}, , and the tilting mode at 212 cm^{-1}. The changes in frequency of the 336 cm^{-1}, 405 cm^{-1}, and 212 cm^{-1} modes as well as the change of the 448 cm^{-1} mode line width show that there is an energy transfer from the lattice to the spin system to stabilize the spin structure. In particular, the energy transfer is indicated by the upturn of the line width around the AFM order which shows that the phonon lifetime becomes shorter below the magnetic order transition. Further analysis of the frequency softening below the AFM order transition shows that the tilting, the rotation, and the bending modes show a$(1 - T/T_N)^{0.5}$ behavior as predicted within "mean field" approximation for the magnetization. The formation of short range AFM order at higher temperatures makes the long range AFM order transition has small fluctuation. It should be noted that the phonon softening is observed already at 140 K which is 10 K higher than the AFM phase transition indicating that the spin-lattice coupling has been present at short range AFM order. In this work, the strongest spin-phonon coupling is obtained for the tilting mode which shows the strong relation between AFM order and Mn-O-Mn bond angles.

4.9 Conclusions

We have shown that the comprehensive study on the phase transitions in $Pr_{0.5}Ca_{1.5}MnO_4$ by means of a variety of experimental measurements have revealed a strong correlation between the charge, orbital, lattice, and spin degrees of freedom as evidenced by the significant changes of structure, resistivity, magnetization, specific heat, and phonon evolution across the phase transitions. The charge and orbital ordering phase transition occurring at 320 K is concurrently marked by apparent change in the evolution of Raman modes, a jump in the resistivity indicating electron localization, and a sharp peaking in the specific heat showing the entropy release. The rapid variations of the lattice parameters as well as the octahedral buckling and distortions across CO transition shown by the XRD analysis indicate an actual lowering of the crystal symmetry occurring at the CO-OO phase transition as implied by the Raman data. This shows a close connection between charge and lattice. The abrupt change of the susceptibility also indicates that the CO transition is accompanied by the replacement of the spin structure formerly dominated by FM correlations with a spin structure dominated by AFM correlations. The evolution of the JT stretching mode further indicates the fluctuations of the orbital orientation even though the orbital order sets in at 320 K. The presence of 2D short range AFM correlations are proposed to indicate the stabilization of the orbital order. The formation of the short range AFM order at high temperature is evidenced by the absence of an anomaly in the specific heat at the 3D AFM phase transition. The strong spin-lattice coupling is observed to accompany the 3D AFM transition. The large distortions of the MnO_6 octahedra induced by the large size difference of the Pr versus Ca ions together with the Mn ion localization is proposed as the significant factor influencing the stability of CO-OO and AFM order, the 3D nature of CO in distorted manganite systems, the strong charge-lattice coupling, and the strong spin-lattice coupling.

Bibliography

[1] G.H. Jonker and J.H. van Santen. *Physica*, 16:337, 1950.

[2] M. B. Salamon and M. Jaime. *Review of Modern Physics*, 73:583, 2001.

[3] L. P. Gor'kova and V. Z. Kresinc. *Physics Reports*, 400:149, 2004.

[4] Y. Tomioka and Y. Tokura. *Phys. Rev. B*, 70:014432, 2004.

[5] R. Mathieu, M. Uchida, Y. Kaneko, J. P. He, X. Z. Yu, R. Kumai, T. Arima, Y. Tomioka, A. Asamitsu, Y. Matsui, and Y. Tokura. *Phys. Rev. B*, 74:020404, 2006.

[6] S. Chi, F. Ye, P. Dai, J. A. Fernandez-Baca, Q. Huang, J. W. Lynn, E. W. Plummer, R. Mathieu, Y. Kaneko, and Y. Tokura. *Proceedings of the National Academy of Sciences*, 104:10796, 2007.

[7] R. Mathieu, J. P. He, X. Z. Yu, Y. Kaneko, M. Uchida, Y. S. Lee, T. Arima, A. Asamitsu, and Y. Tokura. *European Physics Letter*, 80:37001, 2007.

[8] X. Z. Yu, R. Mathieu, T. Arima, Y. Kaneko, J. P. He, M. Uchida, T. Asaka, T. Nagai, K. Kimoto, A. Asamitsu, Y. Matsui, and Y. Tokura. *Phys. Rev. B*, 75:174441, 2007.

[9] M. Ibarra, R. Retoux, M. Hervieu, C. Autret, A. Maignan, C. Martin, and B. Raveau. *Journal of Solid State Chemistry*, 170:361 – 367, 2003.

[10] J. B. Goodenough. *Phys. Rev.*, 100:564–573, 1955.

[11] O. Jochen. *Structural Investigations on layered Manganites and Ruthenates*. PhD thesis, Universitat zu Koln, 2010.

[12] D. Senff, P. Reutler, M. Braden, O. Friedt, D. Bruns, A. Cousson, F. Bourée, M. Merz, B. Büchner, and A. Revcolevschi. *Phys. Rev. B*, 71:024425, 2005.

[13] T. Kimura, K. Hatsuda, Y. Ueno, R. Kajimoto, H. Mochizuki, H. Yoshizawa, T. Nagai, Y. Matsui, A. Yamazaki, and Y. Tokura. *Phys. Rev. B*, 65:020407, 2001.

[14] D. J. Huang, W. B. Wu, G. Y. Guo, H.-J. Lin, T. Y. Hou, C. F. Chang, C. T. Chen, A. Fujimori, T. Kimura, H. B. Huang, A. Tanaka, and T. Jo. *Phys. Rev. Lett.*, 92:087202, 2004.

[15] V. Capogrosso, M. Malvestuto, I. P. Handayani, P. H. M. van Loosdrecht, A. A. Nugroho, and E. Magnanoand F. Parmigiani. *Phys. Rev. B*, 87:155118, 2013.

[16] H. Ulbrich. *Interplay between charge, orbital, and magnetic order in manganites.* PhD thesis, Universitat zu Koln, 2010.

[17] K. Yamamoto, T. Kimura, T. Ishikawa, T. Katsufuji, and Y. Tokura. *Phys. Rev. B*, 61:14706, 2000.

[18] E. Kroumova, M.I Aroyo, J.M. Perez-Mato, A. Kirov, C. Capillas, S. Ivanchev, and H. Wondraschek. *Phase Transition*, 76:155, 2003.

[19] D. Okuyama, Y. Tokunaga, R. Kumai, Y. Taguchi, T. Arima, and Y. Tokura. *Phys. Rev. B*, 80:064402, 2009.

[20] D. Senff, O. Schumann, M. Benomar, M. Kriener, T. Lorenz, Y. Sidis, K. Habicht, P. Link, and M. Braden. *Phys. Rev. B*, 77:184413, 2008.

[21] J. Hemberger, M. Brando, R. Wehn, V. Yu. Ivanov, A. A. Mukhin, A. M. Balbashov, and A. Loidl. *Phys. Rev. B*, 69:064418, 2004.

[22] H. Ulbrich, F. Krüger, A. A. Nugroho, D. Lamago, Y. Sidis, and M. Braden. *Phys. Rev. B*, 84:094453, 2011.

[23] N.F. Mott and E.A. Davis. *Electronic Process in Non-Crystalline Materials.* Oxford University Pers. Inc., 1979.

[24] W. Schnelle, J. Engelhardt, and E. Gmelin. *Cryogenics*, 39:271, 1999.

[25] M. N. Iliev, M. V. Abrashev, H.-G. Lee, V. N. Popov, Y. Y. Sun, C. Thomsen, R. L. Meng, and C. W. Chu. *Phys. Rev. B*, 57:2872, 1998.

[26] S. Onoda, Y. Motome, and N. Nagaosa. *Phys. Rev. Lett.*, 92:236403, 2004.

[27] A. K. Raychaudhuri, Ayan Guha, I. Das, R. Rawat, and C. N. R. Rao. *Phys. Rev. B*, 64:165111, 2001.

[28] T. Qian, R. K. Zheng, T. Zhang, T. F. Zhou, W. B. Wu, and X. G. Li. *Phys. Rev. B*, 72:024432, 2005.

[29] E. Granado, A. Garc´, J. A. Sanjurjo, C. Rettori, I. Torriani, F. Prado, R. D. Sánchez, A. Caneiro, and S. B. Oseroff. *Phys. Rev. B*, 60:11879, 1999.

[30] L. Martin-Carron, A. de Andrés, M. J. Martinez-Lope, M. T. Casais, and J. A. Alonso. *Phys. Rev. B*, 66:174303, 2002.

[31] M. Balkanski, R. F. Wallis, and E. Haro. *Phys. Rev. B*, 28:1928, 1983.

[32] Ch. Kant, J. Deisenhofer, T. Rudolf, F. Mayr, F. Schrettle, A. Loidl, V. Gnezdilov, D. Wulferding, P. Lemmens, and V. Tsurkan. *Phys. Rev. B*, 80:214417, 2009.

[33] Y. Moritomo, A. Nakamura, S. Mori, N. Yamamoto, K. Ohoyama, and M. Ohashi. *Phys. Rev. B*, 56:14879, 1997.

[34] M. A. Majidi, E. Thoeng, P. K. Gogoi, F. Wendt, S. H. Wang, I. Santoso, T. C. Asmara, I. P. Handayani, P. H. M. van Loosdrecht, A. A. Nugroho, M. Rübhausen, and A. Rusydi. *Phys. Rev. B*, 87:235135, 2013.

[35] M. R. Lees, O. A. Petrenko, G. Balakrishnan, and D. McK. Paul. *Phys. Rev. B*, 59:1298, 1999.

[36] H.D. Yang, H.L. Huang, P.L. Ho, W.L. Huang, C.W. Huang, S. Mollah, S.J. Liu, and J.-Y. Lin. *Physica B: Condensed Matter*, 329:801, 2003.

Chapter 5

Optically Induced Phenomena in the Charge, Orbital, and Spin Order of $Pr_{0.5}Ca_{1.5}MnO_4$

5.1 Introduction

Optically induced phases may differ from any of the thermal equilibrium phases occurring in a material, and, moreover, their occurrence may take place on a very fast sub-picosecond time scale. Ultrafast spectroscopy has the appropriate time resolution required to monitor the ultrafast transient dynamics involving the phase transformations processes in materials. It often offers information which is not accessible by experiments under equilibrium conditions and has been used widely to optically induced phases and the complex interactions underlying the following fast dynamical processes in the manganite oxides. This includes studies of the dynamics of correlated polarons and charge disordering [1], the temporal evolution of photo-induced charge order melting associated with insulator to metal transitions [2–4], transient structural changes [5], and the so-called transient "hidden" metastable state associated with the local transformation of a charge-orbital ordered state [6].

The present study focuses on the effects of optical excitation on the charge-orbital and spin ordering in $Pr_{0.5}Ca_{1.5}MnO_4$ (PCMO), a half doped layered manganite exhibiting charge-orbital order (CO-OO), short range two dimensional (2D) antiferromagnetic (AFM) correlations, and long range AFM order [1] . In this system, the optical responses are strongly influenced by the presence and changes of the charge, orbital, and spin orders [7]. Figure 5.1 (a) shows the optical conductivity (σ) of PCMO observed along the *a*-axis. The figure shows that σ has a broad absorption band centered around 1 eV, which has been attributed to intersite *d-d* transitions. It shows a blue shift with decreasing temperature and is clearly influenced by the charge, orbital, and spin order in PCMO [7]. The band above 3 eV is attributed to the *p-d* charge transfer transition and is only weakly temperature dependent.

---

[1] detailed information of the CO-OO, short range 2D AFM correlations, and long range AFM order in $Pr_{0.5}Ca_{1.5}MnO_4$ are presented on Chapter 4 of this thesis

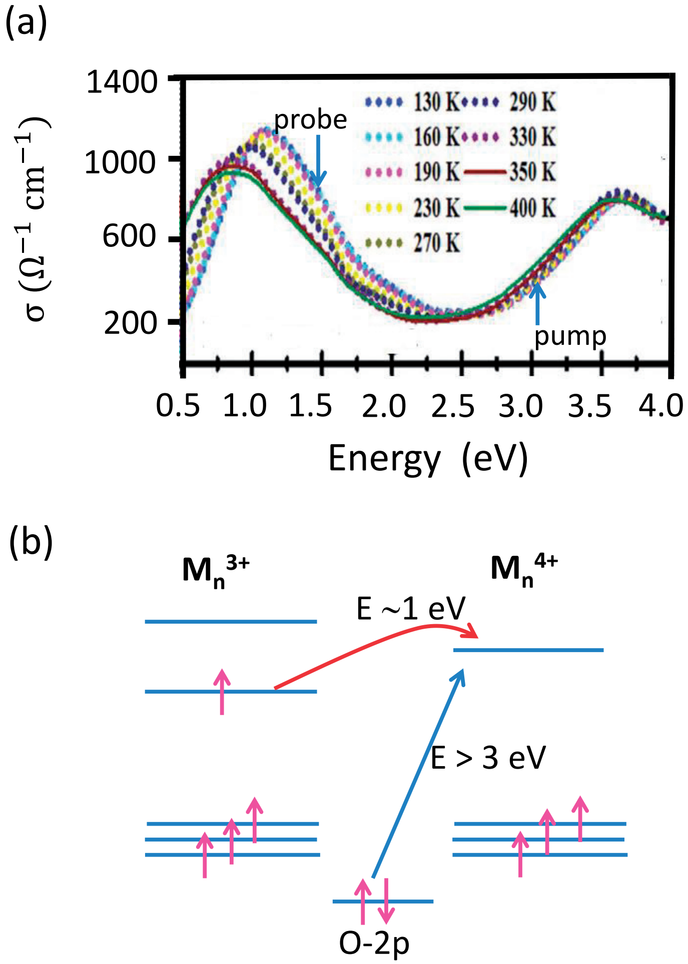

Figure 5.1: *(a) The optical conductivity of* $Pr_{0.5}Ca_{1.5}MnO_4$ *observed along a axis in the 0.5-4 eV range for various temperatures. (Adapted from Ref [7]) (b) Schematic diagram of relevant electronic energy levels in manganese and oxygen as well as illustration of the associated p-d charge transfer and and intersite d-d transitions.*

Figure 5.1 (b) shows a schematic level diagram of part of the electronic structure of two nearest neighbors (NN) Mn ions ($Mn^{3+}$and Mn^{4+}) together with possible *p-d* charge-transfer and intersite *d-d* transitions. A ferromagnetic alignment has been used in the illustration. In case of NN with AFM coupling, the intersite transition should either include a spin-flip, or be affected by the Hund's coupling energy which is typically 0.7 eV in manganite [8], and is within the broad 1 eV absorption band.

The presence of an electron in the e_g orbital of Mn^{3+} induces a Jahn-Teller (JT) distortion and an associated energy level splitting. A *p-d* charge transfer transition changes the non-JT active Mn^{4+} into a JT active Mn^{3+} ion. A JT distortion of this ion will lead to structual strain, and potentially even lattice (and orbital) disorder in the orbitally ordered phase. These local distortions can act as a nucleation center for an optically induced order-disorder transition, particularly in the case of a strongly connected MnO_6 network as found in $Pr_{0.5}Ca_{1.5}MnO_4$. This phenomenon can be studied by deploying an ultrafast pump-probe experiment. A pump pulse with an energy of about 3 eV is used to promote electrons from the oxygen $p-$orbitals to the Mn^{4+} e_g orbitals, while changes in the ordering can be observed by measuring the transient optical response in the vicinity of the intersite *d-d* transitions. In our experiment we used a pump-pulse of 3.1 eV energy and a probe pulse of 1.55 eV energy (see also figure 5.1(a)).

The experimental results discussed in this chapter show that the transient response is strongly temperature and laser fluency dependent. We interpret our experimental results in terms of photo-induced charge and lattice disorder which weaken the intersite *d-d* transitions. Around the CO-OO phase transition (T_{CO-OO}), the transient signal is strongly enhanced and characterized by a critical slowing down of the fast (1 ps) dynamics. This strong transient signal developed around CO-OO transition features a longer time scale (100's of ps), which is attributed to the creation and growth of disorder domains. The formation of AFM order at lower temperatures also influences the transient reflectivity dynamics, for instance by a modest acceleration of the fast relaxation component, indication of possible activation of an additional charge-magnon decay mechanism in the AFM state [9]. The final part of this chapter will be devoted to the discussion of a transition from the ordered into a disordered state for a laser fluence exceeding 3.5 mJ/cm^2 at 293 K.

5.2 Experimental Details

Two-color time resolved pump-probe experiments have been performed over a wide temperature range, covering T_{CO-OO} of 320 K and T_N of 127 K. A Ti-sapphire laser (Hurricane, Spectra Physics) is utilized to generate the short (<150 fs) 800 nm pulses with 1 kHz repetition rate. A 400 nm pump beam is subsequently generated with BBO crystal. The 400 nm (3.1 eV) pump pulse is employed to induce *p-d* charge transfer transitions, whereas the 800 nm probe beam (1.55 eV) is used to probe and monitor the transient relaxation process involving the intersite *d-d* transitions (see Fig. 5.1). The 400 nm pump beam has a penetration depth of ∼0.6 μm in PCMO, which is about twice that of the 800 nm probe light (∼0.35 μm). This guarantees that the volume probed by the 800 nm light is fully covered by 400 nm. The sample is a single crystal cleaved in the *ab* plane and mounted on the cold finger of a He-flow cryostat (Janis). The pump and probe polarization are chosen to be parallel to the crystallographic *a*-axis of the sample.

Temperature dependent experiments are performed with a constant pump fluence of 0.34 mJ/cm^2 on the sample surface, which corresponds roughly to impinging 1 photon on ∼1000 Mn ions. The maximum laser induced heating is estimated to be about 10 K at 300 K.[2]

In addition to the temperature dependent experiments using a relatively low fluence of pump laser, a power dependent experiments was also performed to investigate a possible optically induced transition from the ordered to a disordered phase. For this experiment, the pump fluence was varied between 0.1 and 5 mJ/cm^2 at the cold finger temperatures of 293 K (slightly below CO-OO transition), 320 K (at the phase transition), and 340 K (charge-orbitally disordered phase).

5.3 Experimental Results

5.3.1 Temperature Dependent Optical Response

The time profile of transient reflectivity (ΔR/R) obtained from our time resolved experiments are depicted in Fig. 5.2 for different temperatures. The strongest transient signal occurs around 300 K, a temperature slightly lower than T_{CO-OO}, and it generally decreases as the temperature moves away from 300 K. The observed negative transient reflectivity signal generally shows three distinctly different features corresponding to different time regimes during relaxation of the photo-excited system. The three regimes consist of the very short period near the instantaneous response, followed successively by a lasting about 1 ps fast relaxation process, and a long lived component lasting more than 300 ps. The instantaneous response occurs within 300 fs, which is close to the experimental time resolution, with an insignificant temperature dependent change of roughly less than 1 % in the transient reflectivity. Instead, the fast relaxation processes lasting from 300 fs to 1.4 ps do exhibit sensitive non-monotonous temperature dependence. The long lived transient reflectivity following the fast relaxation also shows similar temperature effect while differing in details. In addition, the process display general feature of plateau profiles with long life time exceeding our experimental time-span of 300 ps, and suggesting the existence of an optically induced metastable state. An anomalous behavior appears around T_{CO-OO} of 320 K marked by a gradual but consistent increase of the transient response at longer timescales taking the system further away from the initial equilibrium state.

The detailed temperature dependent behavior of the transient reflectivity is more clearly depicted by its temperature profile of the metastable state deduced

---

[2] The laser heating is calculated using formula $Q = Cm(T_f - T_i)$, with Q is the average laser energy obtained by multiplying the pump fluence with the laser spot size, C is the $Pr_{0.5}Ca_{1.5}MnO_4$ specific heat as presented in Fig. 10 Chapter IV, m is the molarity of the sample, T_i is the bath temperature, and T_f is the final temperature induced by laser. The integration of C curve from T_i up to T_f should give a same value as Q/m.

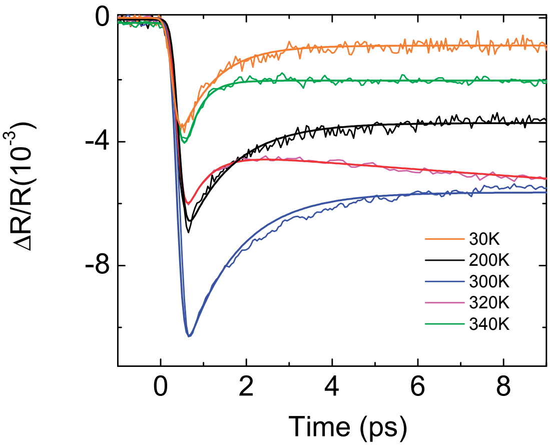

Figure 5.2: *The temporal evolution of the transient reflectivity at several temperatures in* $Pr_{0.5}Ca_{1.5}MnO_4$ *for a pump fluence of 0.34 mJ/cm*^{2}*. The smooth lines are fits of Eq. 5.1 to the data.*

from data presented in Fig. 5.2 at 10 ps normalized with the instantaneous response ($\Delta R^*/\Delta R_0$). The result is given in Fig. 5.3. It is seen that the ratio has a strong peak near T_{CO-OO}, showing a maximum at 320 K. The ratio is relatively constant for $T_N < T < T_{CO-OO}$, but shows a rapid decrease as the temperature further decreases below T_N, presumably because it becomes more difficult to maintain the metastable state due to stiffening of the lattice.

For a quantitative characterization of the above mentioned dynamical features we fitted a sum of exponential functions convoluted with a Gaussian response function to our experimental data according to the following expression

$$\frac{\Delta R(t)}{R} = \Delta R^* + (\Delta R_0 - \Delta R^*)exp[-t/\tau_1] + \Delta R^{**}[1 - exp[-t/\tau_2]] \tag{5.1}$$

The instantaneous response, represented by ΔR_0, is due to the introduction of an extra electron on the Mn^{4+} ions through the *p*-*d* transition. The presence of this extra electron creates an additional Mn^{3+} site, thereby decreasing the overall strength of the intersite *d*-*d* transitions. The initial response relaxes rapidly with a time constant τ_1 to a long lived plateau ΔR^*. In addition to this plateau behavior we introduced a second long lived component (third term in Eq.5.1) characterized by a strength ΔR^{**} and an a characteristic in-growing time τ_2 in order to capture the slowly ingrowth component near the 320 K phase transition. In general the data is well fitted by Eq.5.1 to as indicated by smooth lines in Fig. 5.2).

The fast relaxation time (τ_1) obtained from a best fit of Eq. 5.1 to the experimental data is shown in Fig. 5.4. Its temperature dependence shows three

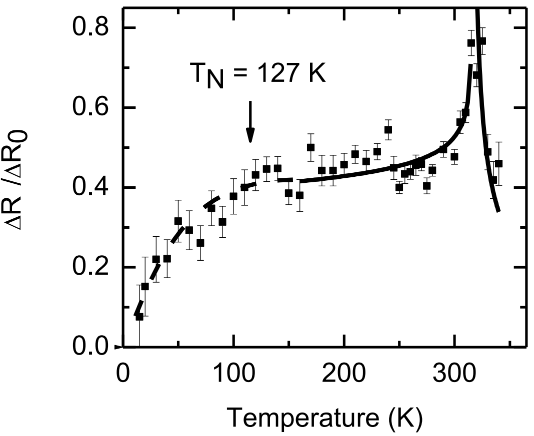

Figure 5.3: *(a) The ratio $\Delta R^*/\Delta R_0$ between the transient response in the meta stable state and the instantaneous transient response. The solid lines are fits to the data using $|[(T-Tc)/Tc]^\alpha|$ for temperature above and below 300 K, respectively. The dashed line is a guide to the eye highlighting the changed behavior below T_N.*

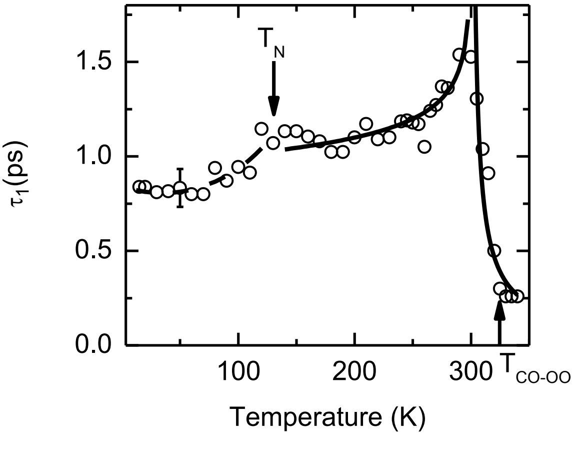

Figure 5.4: *The fast relaxation time τ_1 as a function of temperature. The solid lines are fits with $|[(T-Tc)/Tc]^\alpha|$ for temperatures above and below 300 K, respectively. The dashed line is a guide to the eyes accentuating the change of the trend below T_N.*

main features. It is very fast above T_{CO-OO}, and actually beyond the limit of the temporal resolution of our system. Upon approaching T_{CO-OO} from above, τ_1 increases sharply reaching a maximum of about 1.4 ps at 300 K which is slightly below the CO-OO temperature. Upon further decreasing the temperature, τ_1 reverses its trend and decreases rapidly toward a stable value of about 1 ps at 240 K.

Thereafter, τ_1 remains relatively constant until T_N of 130 K is reached, after which τ_1 further decreases down to 0.8 ps.

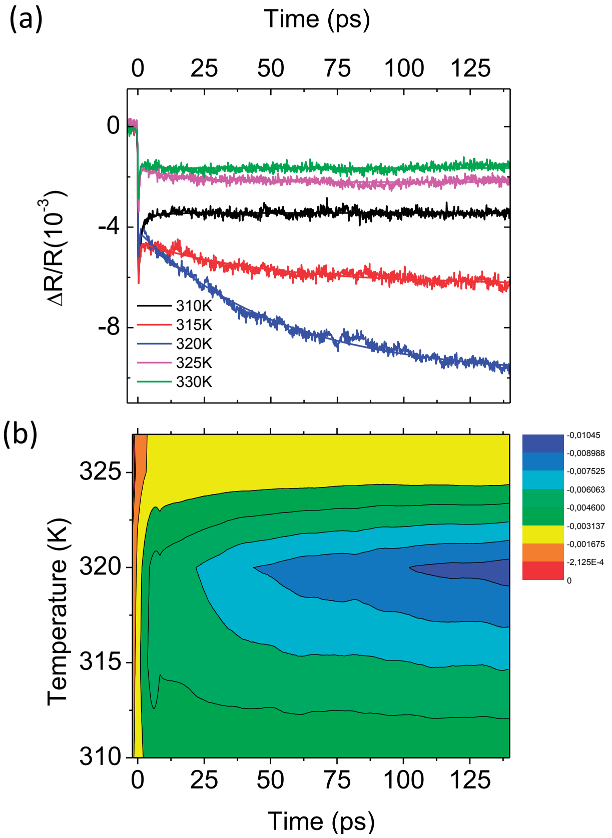

Figure 5.5: *(a) The anomalous dynamical behavior around* T_{CO-OO} *of 320 K observed using a pump power of 0.34 mJ/cm*^{2}*, together with fits using Eq. 5.1 (smooth lines). (b) Intensity map of the temperature dependence of the transient response in the vicinity of the charge-orbital ordering transition.*

It is important to add that the anomalous dynamical behavior around 320 K is further corroborated in Fig. 5.5 displaying the temperature dependent variation of transient reflectivity and τ_2. The most remarkable effect appears at 320 K where an increase of ingrowth transient reflectivity signal and a sudden reversal of the trend of τ_2) variation take place. Figure 5.5 (b) maps the amplitude of the transient reflectivity as function of time and temperature. Near T_{CO-OO}, the ingrowing signal becomes very slow, reaching a timescale of more than 50 ps. This can also be seen in Fig. 5.6, which shows τ_2 as a function of temperature obtained from the best fit of dynamical behavior using Eq. 5.1. The maximum value is about 52 ps at 320 K. The anomalous effect is only observed very close to the phase transition

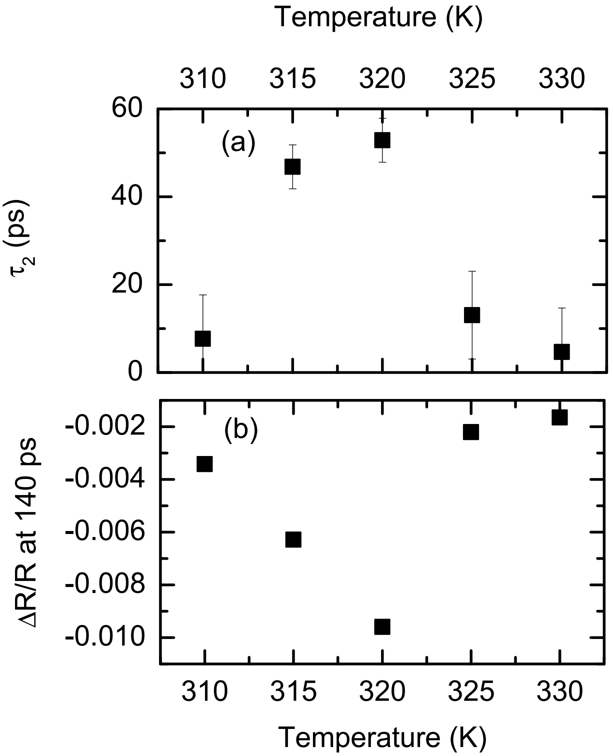

Figure 5.6: *The temperature dependence of the ingrowth time τ_2 of the anomalous signal near the charge-orbital ordering transition.*

and disappears for temperatures more than 10 K away from T_{CO-OO}.

5.3.2 Laser Fluence Dependent Optical Response

The transient response of the sample to the pump laser fluence in the ordered and disordered phases are presented in Fig. 5.7. They both exhibit the general the general features of instantaneous initial increase of ΔR/R and fast relaxation to the relatively long lived plateau of ΔR/R. In the ordered phase (293 K), the amplitude of transient reflectivity as well as the dynamics are strongly power dependent. The amplitude of ΔR/R increases monotonously with laser fluence and the corresponding fast relaxation process is getting faster with increasing laser fluence. On the other hand, the dynamical responses are found to be relatively less sensitive to increasing laser fluence in the disordered phase (340 K), even though they share qualitatively similar characteristics of monotonously increase of the transient reflectivity amplitude with power fluence. The detailed qualitative analysis of these observations will be presented in the following.

The pump laser fluence dependent variations of τ_1 and ΔR^* at 293 K are

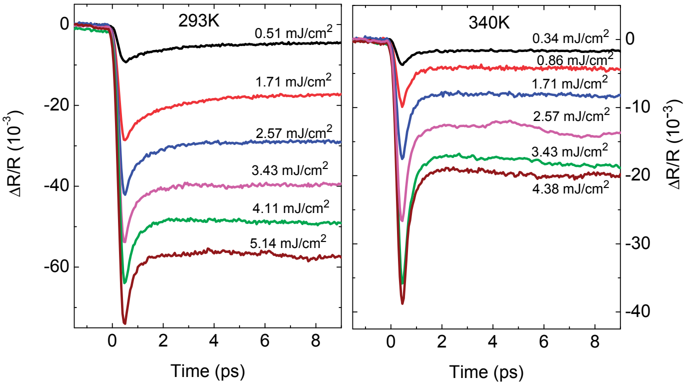

Figure 5.7: *The pump laser fluence dependent transient dynamics as observed in the ordered (293 K, left) and disordered (340 K, right) phases of* $Pr_{0.5}Ca_{1.5}MnO_4$.

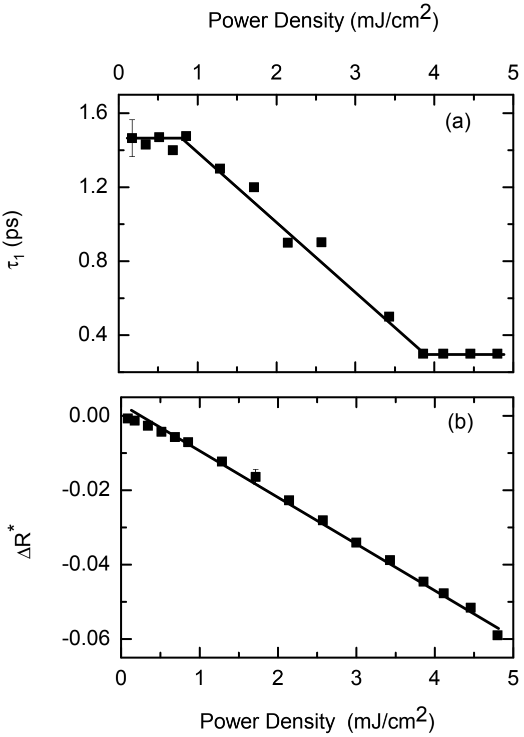

Figure 5.8: *The pump laser fluence dependent variations of (a) the fast relaxation time* (τ_1)*. (b) the amplitude of the transient reflectivity at 20 ps* (ΔR^*) *observed at* $T = 293$ *K. The solid lines are guides to the eyes.*

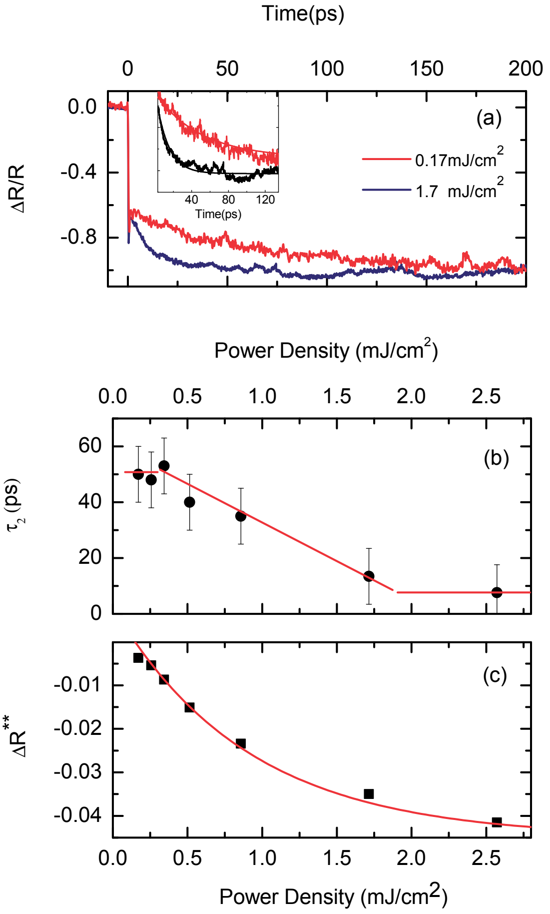

Figure 5.9: *(a) The transient dynamics of optical responses for pump fluence of 0.17 and 1.7 mJ/cm*^{2} *at* $T_{CO-OO} \approx$ 320 *K. The curves have been normalized to the transient reflectivity amplitude at 200 ps. The inset shows the curves with their fits on an expanded scale. (b) The fluence dependent variations of anomalous signal growing time* (τ_2) *and (c) the amplitude of* $\Delta R/R$ *at 200 ps* (ΔR^{**}) *as a function of pump fluence. The solid lines in (b) and (c) are guides for eyes.*

extracted from the best fits of Eq. 1 to the experimental data and the results are presented in Fig. 5.8. Below 1 mJ/cm^2, τ_1 is relatively constant at 1.4 ps, a typical value for ordered phase . When the power increases further, τ_1 decreases rapidly and finally levels off above 3.5 mJ/cm^2 to the time resolution limit of 0.3 ps, as observed in the case of the low laser fluence experiments in the disordered phase. This strongly suggests that the pump laser pulse is driving the sample into the charge disordered phase. An estimate effect of heating by the pump laser, based on specific heat data of $\mathrm{Pr_{0.5}Ca_{1.5}MnO_4}$ (see Fig. 4. 10, chapter 4), gives a final temperature of about 350 K as induced by the absorption of the 3.5 mJ/cm^2 laser pulse. On the other hand, the ΔR^* continuously increases with increasing pump fluence implying the increasing of the number of new $\mathrm{Mn^{3+}}$ with increasing of excited electrons. The monotonous change of the ΔR^* with laser fluence signifies that the change in the τ_1 is indeed due to increased laser induced heating.

The anomalous ingrowing signal at 320 K is also dependent on pump fluence. The detailed dynamics is presented in Fig. 5.9 where the amplitude of transient reflectivity is also seen to increases with pump fluence. It displays exponential trend. The τ_2 is also relatively constant below 0.3 mJ/cm^2 and decreases almost linearly upon further increase of pump fluence.

5.4 Discussion

The temperature dependent variations of various quantities presented as the experimental data have provided evidence of the strong influence of charge, orbital, and spin order on transient optical responses at different temperatures. Interesting features are revealed in those date signifying the interplays among those different types of orders in the system. In this section the underlying physical processes and mechanisms will be elaborated and explained in more details.

For that purpose let us consider the model of charge-orbital order and its photo induced changes depicted in Fig. 5.10 (a). The photo induced *p*-*d* charge transfer creates an excited electron on a $\mathrm{Mn^{4+}}$ site, thereby converting it into an extra $\mathrm{Mn^{3+}}$ site and reducing the CO-OO order . This in turn decreases the strength of the intersite $d-d$ transition and the e_g electron mobility which is manifested as the instantaneous response (ΔR_0). The photo excited electron might decay immediately into ground state with fast relaxation time (τ_1). Alternatively, it may induce a metastable local JT distortion (Fig. 5.10(b)), which is observed as the plateau (ΔR^*) in the transient reflectivity. This distortion creates a strain around the photo excited ion and may act as a nucleation center of optically induced lattice/orbital disorder (Fig. 5.10(c)). Near the CO-OO transition temperature there is sufficient activation energy to surmount the potential barrier between the ordered and disordered phases. The observed lattice parameters around CO-OO transition (see Fig. 6 Chapter IV) further suggests the structural adaptation leading to the decreasing of energy barrier around CO-OO transition temperature. Meanwhile one expects a relatively slow ingrowth of the optically induced disordered phase, which is indeed observed as the slow ingrowth transient reflectivity signal (ΔR^{**}) occurring near the phase transition.

The relatively constant value of $\Delta R^*/\Delta R_0$ for $T_N < T < T_{CO-OO}$ shown in Fig. 5.3 indicates that the number of electrons participating in the distorted lattice formation does not change significantly in this temperature range. Considering the relatively constant lattice parameters in this temperature range, it might relate to relatively constant lattice stiffness. This temperature range is also characterized

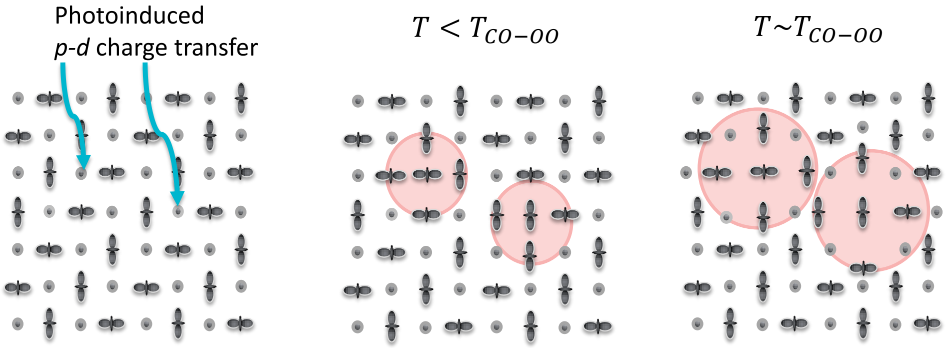

Figure 5.10: *Photo-induced JT distortion and distorted domain growth in PCMO. (a) $p-d$ transitions introduce additional Mn^{3+} sites. (b) Formation of metastable local distortions (red circles). (c) Nucleation and domain growth (red areas) close the CO-OO phase transition temperature.*

by the relatively constant τ_1 which the energy barrier between the distorted and undistorted manganite remains relatively unchanged in that temperature range.

The further decrease of $\Delta R^*/\Delta R_0$ Below T_N indicates an increased spin lattice coupling leading to an increase of the lattice stiffness so that it becomes more difficult to induce a JT distortion. In conjunction with the decrease in the absolute ratio, a slight decrease of τ_1 is also observed below T_N. This is indicative of the important influence of electron-spin coupling on the charge relaxation as previously reported [9]. In other words, charge relaxation may proceed with magnon creations in magnetically ordered systems [10].

To quantify the additional contribution of spin excitations to the relaxation rate in the magnetically ordered phase, we assume that relaxation in the magnetically disordered phase occurs only through interaction with the lattice ($\tau_1 = \tau_l$) while the relaxation rate in the magnetically ordered phase is given by $\frac{1}{\tau_1} = \frac{1}{\tau_l} + \frac{1}{\tau_s}$, with $\frac{1}{\tau_l}$ and $\frac{1}{\tau_s}$ denote the relaxation rates via electron-lattice and electron spin coupling, respectively. Figure 5.11 shows the temperature dependence of $\frac{1}{\tau_s}$, obtained by subtracting τ_l in the magnetically ordered phase with the value of τ_1 at 127 K. The obtained values for the relaxation times vary from ~20 ps near the phase transition down to ~ 3 ps at low temperature, thus relaxation through electron-spin coupling is still about three times less effective than relaxation through electron-lattice coupling .

The amplitude of the transient reflectivity generally increases with increasing pump fluence due to the increasing density of excited states, and hence the number of JT distorted Mn^{3+} sites. At 293 K, the τ_1 changes from 1.4 ps at fluence lower than 1 mJ/cm^2 to 0.3 ps at fluence larger than 3.5 mJ/cm^2. It is strongly suggestive of the local heating effect induced by the pumping laser pulse in driving the sample from its initial temperature of 293 K into the temperature regime beyond the

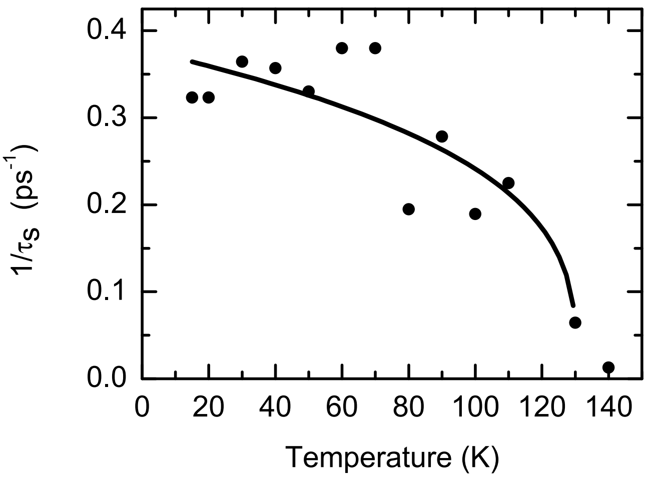

Figure 5.11: *The spin contribution to the relaxation rate. Solid line is a guide to the eye.*

charge-orbital order transition temperature. The τ_2 at 320 K also continuously decreases for laser fluence above 0.3 mJ/cm^2 which is also an indication of laser heating effect. The ΔR^{**} exhibits exponentially rising trend with pump fluence. This suggests that the strain propagation as well as the growth of disorder domains remains more or less restricted in small volume although the number photo induced Mn^{3+} increases with increasing laser fluence.

5.5 Conclusions

The temperature dependent transient response of $\mathrm{Pr_{0.5}Ca_{1.5}MnO_4}$ shows a marked influence of the charge/orbital and spin orders. Our results specifically show that optically induced additional Mn^{3+} sites through the $p-d$ transition generate a local JT distortion which acts close to the CO-OO transition temperature as nucleation centers for an optically induced disordered phase. In the magnetically ordered phase we observe a modest regain of the fast relaxation speed of the transient reflectivity signal. It is interpreted as due to the opening of an additional relaxation channel via electron-spin interaction although it is found to be only about one third the effectiveness of the electron-lattice relaxation. In addition, the laser pump is also shown to drive the system from ordered to disordered phase via the optically generated heating effect.

Bibliography

[1] Y. H. Ren, M. Ebrahim, Z. A. Xu, and G. Lüpke. *New Journal of Physics*, 11:113013, 2009.

[2] K. Miyano, T. Tanaka, Y. Tomioka, and Y. Tokura. *Phys. Rev. Lett.*, 78:4257, 1997.

[3] M. Fiebig, K. Miyano, Y. Tomioka, and Y. Tokura. *Appl. Phys. B*, 71:211, 2000.

[4] T. Ogasawara, T. Kimura, T. Ishikawa, M. Kuwata-Gonokami, and Y. Tokura. *Phys. Rev. B*, 63:113105, 2001.

[5] P. Beaud, S. L. Johnson, E. Vorobeva, U. Staub, R. A. De Souza, C. J. Milne, Q. X. Jia, and G. Ingold. *Phys. Rev. Lett.*, 103:155702, 2009.

[6] H. Ichikawa, S. Nozawa, T. Sato, A. Tomita, K. Ichiyanagi, M. Chollet, L. Guerin, N. Dean, A. Cavalleri, S. Adachi, T. Arima, H. Sawa, Y. Ogimoto, M. Nakamura, R. Tamaki, K. Miyano, and S. Koshihara. *Nat.Mater.*, 10:101, 2011.

[7] M. A. Majidi, E. Thoeng, P. K. Gogoi, F. Wendt, S. H. Wang, I. Santoso, T. C. Asmara, I. P. Handayani, P. H. M. van Loosdrecht, A. A. Nugroho, M. Rübhausen, and A. Rusydi. *Phys. Rev. B*, 87:235135, 2013.

[8] N. N. Kovaleva, A. V. Boris, C. Bernhard, A. Kulakov, A. Pimenov, A. M. Balbashov, G. Khaliullin, and B. Keimer. *Phys. Rev. Lett.*, 93:147204, 2004.

[9] Z. Lenarčič and P. Prelovšek. *Phys. Rev. Lett.*, 111:016401, 2013.

[10] S. F. Zhang. *Journal of Applied Physics*, 79:4542, 1996.

Chapter 6

Magneto-Elastic and Magneto-Electric Coupling in Geometrically Frustrated Iron Jarosite $KFe_3(OH)_6(SO_4)_2$

6.1 Introduction

The topological incompatibility between the lattice and the spin structure in a geometrically frustrated magnetic material prohibits the formation of a fully ordered ground state [1, 2]. The magnetic energy is not fully minimized and the system has a tendency to be in a manifold of nearly degenerate ground states rather than in a single ground state. Therefore, a small additional interaction can easily drive the system into one of the states leading to a variety of interesting physical properties at low temperatures, including quantum disordered ground states [3, 4] cascades of metamagnetic phase transitions [5, 6], and even multiferroic behavior [7]. Interactions which may dictate the choice of thermodynamic state include applied magnetic fields, thermal fluctuations, magnetic anisotropy, next nearest neighbor interaction, and magneto-elastic couplings.

In a highly frustrated system, a zero energy magnetic excitation should exist due to spin-liquid like spin fluctuations of the magnetically disordered ground state. In jarosite, a low energy magnetic excitation has been observed below the Néel temperature of 65 K in inelastic neutron scattering experiments [9] indicating the removal of the degeneracy upon entering the magnetically ordered phase. In the presence of important spin-lattice coupling, one expects that besides observing this magnetic excitation also the selection rules for observing phonon modes will change upon entering the magnetically ordered phase due to corresponding changes in the lattice structure. The magnetostriction phenomena may lead to anomalous behavior of the observed phonon modes[12], for instance anomaly due to a modulation of the superexchange interaction between nearest neighbor (NN) Fe ions mediated by the oxygen ions which modulate the Fe-O-Fe bond angle and/or the Fe-O bond length. In addition, the spin-lattice coupling has also been proposed to have an effect in the frustration releasing process [13, 14] which will result in the lattice distortion in order to gain the exchange energy. Specifically, the different bond lengths of distorted lattice in the system inevitably induce unequal spin correlations with the strongest spin correlation winning the competition and the frustration is therby released. The magneto-elastic coupling subsequently induces magneto-electric coupling since changes of the atomic positions are expected to change the electron distribution and electrically create polarized system [15].

Here we investigate the magneto-elastic and magneto-electric coupling in the iron jarosite $KFe_3(OH)_6(SO_4)_2$. This compound has been proposed as a good model for the realization of a two dimensional (2D) geometrically spin frustrated system . Due to its low dimensionality as well as due to the geometrical frustration, iron jarosite is expected to have no long ordered ground state at any finite temperature. Despite this expectation, antiferromagnetic (AFM) order has been observed in this compound at 65 K [8, 9]. In our study, the new Raman modes are observed below Néel temperature which are proposed to arise from magnetostrictive coupling effect due to a modulation of the Fe-O-Fe superexchange interaction by the phonons.

6.2 Iron Jarosite Properties

The material used in our study is a single crystal $KFe_3(OH)_6(SO_4)_2$ grown hydrothermally in a stainless vessel (Parr Instrument Company 4749 acid digestion bomb) with a 23 mL Teflon insert subjected to autogenous pressure. Detail of sythesis, X-ray crystallographic, and material characterization was already reposted by A.J.C. Buurma [16]. In this section, a brief review is given on the magnetic properties as well as the phase transition which support our investigation of magneto-elastic and magneto-electric coupling effects.

The crystallographic structure of iron jarosite $KFe_3(OH)_6(SO_4)_2$ is presented in Fig. 6.1 (a). It has a trigonal structure with $R\overline{3}m$ space group lattice and lattice parameters of $a = 7.312(3)$ Å and $c = 17.254(15)$ Å. There is no change of structure observed down to very low temperature. The magnetic iron Fe^{3+} (with spin $S=5/2$) ions are centered in oxygen octahedral network and form *kagomé* lattice pattern in *ab* plane as shown in Fig. 6.1 (b). The four oxygen ions in the basal plane are combined with hydrogen ions forming the hydroxy group (OH) while the two apical oxygens also belong to the SO_4^{-2} group. The non magnetic ion K^+ and SO_4^{-2} separate the two adjacent *kagomé* lattice planes so that iron jarosite might be viewed as a realization of a two dimensional (2D) magnetic structure. Having the Fe^{3+} ions located on the vertices of a mesh of corner shared triangles, the spin configuration is geometrically frustrated.

As mentioned earlier, antiferromagnetic order has been observed in this system below 65 K. Figure 6.2 shows the magnetic susceptibility of polycrystaline $KFe_3(OH)_6(SO_4)_2$ measured in zero field cooled mode from 2 K up to 300 K with external magnetic field of 500 Oe. The AFM order is indicated by an inflection of magnetic susceptibility at 65 K. An upturn of magnetic susceptibility

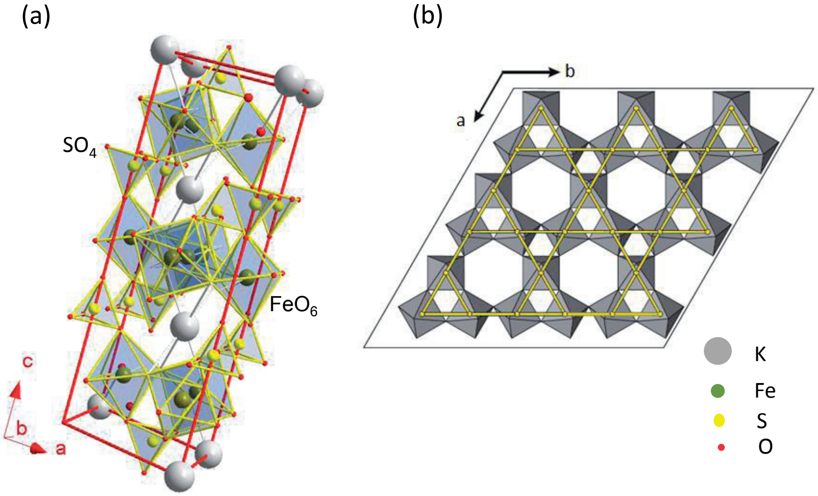

Figure 6.1: *(a) The three dimensional crystalographic structure of iron jarosite and (b) the two dimensional (2D) FeO$_6$ octahedral network in ab plane. The H atoms are not drawn explicitly. Solid yellow line in 2D figure shows the Fe^{3+} network. Figures are taken from [16].*

observed below 40K is most likely due to paramagnetic impurities or defects. The three dimensional (3D) magnetic order is proposed to have its origin in the slightly canted spin orientation which has been confirmed by single crystal magnetization measurement [17]. In this report, a sharp peak of magnetization curve was exhibited when external magnetic field was applied along *c* axis, whereas it was only a broaden cusp observed for external magnetic field applied in *ab* plane.

Fig. 6.3 (a) describes the spin structure in 2D *kagomé* plane. It has a structure with 120^0 angle between nearest neighbor Fe ion spin orientations. The spins have two possible chiralities, clockwise (+ chirality) and anticlockwise (- chirality). Figure 6.3 (b) shows the 3D spin structure. Between two adjacent layers, spins are aligned antiferromagnetically. Spins cant out of kagomé plane and form an "umbrella" structure out of kagomé plane.

Several mechanisms have been proposed to explain the canted spin structure [8, 10, 11, 18]. The total effective spin Hamiltonian has been formulated as Eq. 6.1

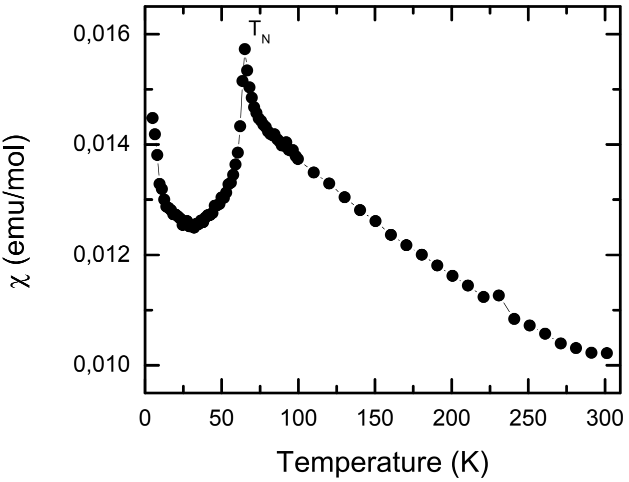

Figure 6.2: *The magnetic susceptibility measured in polycrystaline sample of* $KFe_3(OH)_6(SO_4)_2$*. Figure is adopted from [16].*

$$H = \sum_{nn}[J_1\vec{S_i}\bullet\vec{S_j} + D_{ij}\vec{S_i}\times\vec{S_j}] + \sum_{nnn} J_2\vec{S_k}\bullet\vec{S_l} - D\sum_i (S^i_{z'})^2 - E\sum_i[(S^i_{y'})^2 - (S^i_x)^2] \tag{6.1}$$

Inami et al. proposed that the 3D FM and "umbrella" structure are due to single ion anisotropy mechanism [10]. In the model, the local coordinates of inclined FeO6 octahedral (x', y',z') are defined in Fig. 6.3 (a). The dominant factor is the direct exchange interaction between two nearest neighbor of Fe ions characterizing by the J_1. The D and E parameters are denoting the contributions of the single ion anisotropy along the apical and the basal plane, respectively. The D contribution is considered to be small since the Fe spins are mostly oriented in the basal plane. The superposition of anisotropies along local axes x' and y' is proposed to induce a slightly canted spin along c so that the system has an "umbrella" structure for each layer and is coupled antiferromagnetically between two adjacent layers. The DM interaction coupling (D_{ij}) and the exchange between two next nearest neighbor ions (J_2) are not included in this model.

Another result of neutron diffraction has been analyzed using a DM based model [18]. In this model, the single ion anisotropy contribution has been considered to be very small. The non zero parameters in Eq. 6.1 are J_1, J_2, and D_{ij}, with J_1 as the dominant factor. In this model, the DM coupling was shown to be the mechanism inducing the 3D long range and slightly canted spins along c direction which subsequently trigger an "umbrella" spin structure [8, 11, 18].

The phase transitions are also accompanied by a drastic change in the specific

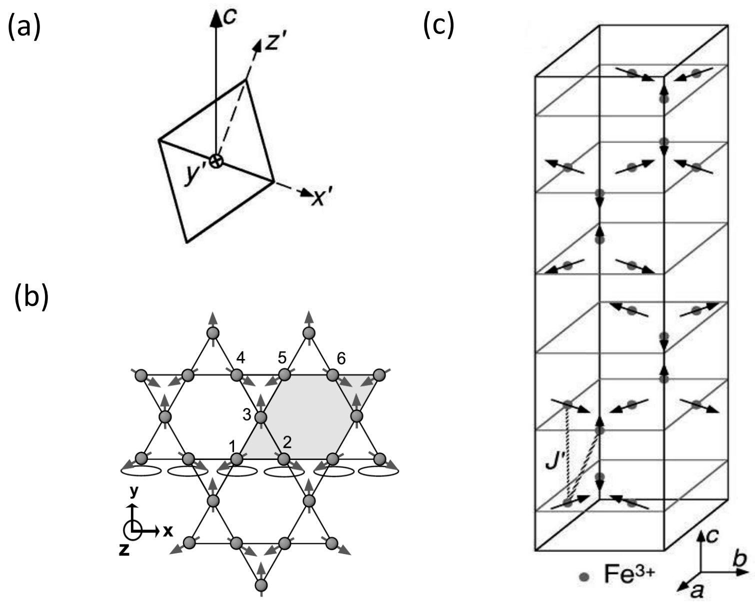

Figure 6.3: *(a) The local coordinates (x',y',z') of the inclined octahedral. (b) The 2D and (c) the 3D spin structure of* $KFe_3(OH)_6(SO_4)_2$ *as constructed from neutron neutron scattering data [9, 10]*

heat. Fig. 6.4 (a) shows a sudden jump marking the AFM order at 65 K. The inset shows the derivative of the specific heat to accentuate the expected anomaly at 31 K as indicated by capacitance data. The experimental data is fitted with Einstein specific heat model $C = Nk_B \sum_{i=1}^{n} \left[\frac{\hbar\omega_i}{k_B T}\right]^2 \left[exp\frac{\hbar\omega_i}{k_B T}\right] \left[exp(\frac{\hbar\omega_i}{k_B T}) - 1\right]^{-2}$ to determine the phonon contributions. Here, the N, ω, and n are the number of atoms in the system, the optical phonon frequency, and the number of phonons contributing to specific heat, respectively. The black and red lines in Fig. 6.4 (a) show the experimental data and the deduced phonon contributions, respectively. After subtracting the specific heat from phonon contributions, the magnetic entropy change is calculated by integrating the C/T curve over temperature around AFM phase transition ($\Delta S = \int \frac{C}{T} dT$). The result is presented in Fig. 6.4 (b). The maximum expected entropy ($S_{max} = Rln(2s+1)$, with R is molar gas constant) is indicated by dashed horizontal line. The calculated magnetic entropy is 13.6, about 91% from maximum entropy expected for spin s=5/2. It indicates no significant short range order above 65 K. The spins are collectively ordered below Neel temperature

The anomalies were also observed in the dielectric measurement. Figure 6.5 (b) shows capacitance of a single crystal $KFe_3(OH)_6(SO_4)_2$when two electrodes were applied along *a* crystallographic axis. It was measured with Andeen Hagerling

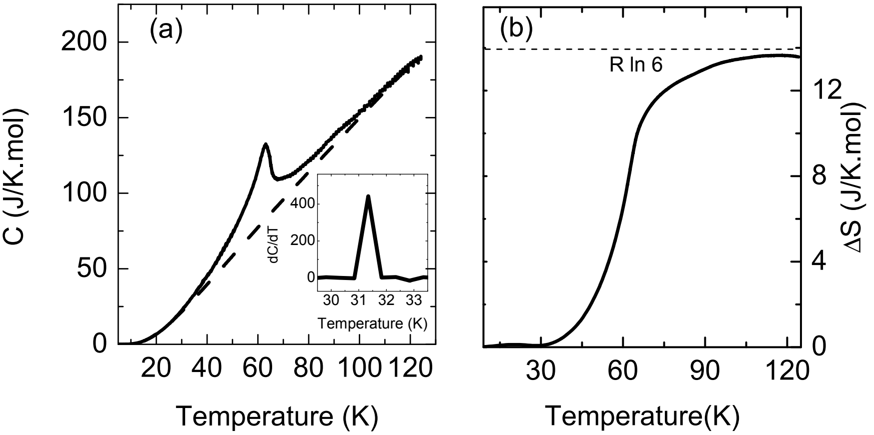

Figure 6.4: *(a) The specific heat measured from 10 to 125K. Solid and dashed lines indicate the experimental data and phonon contribution, respectively. Inset shows the derivative curve of specific heat, accentuating the expected anomaly around 31 K. (b) The magnetic entropy change (*ΔS*) calculated after subtracting phonon contribution from specific heat data. Dashed horizontal line indicates the maximum entropy expected for spn s=5/2.*

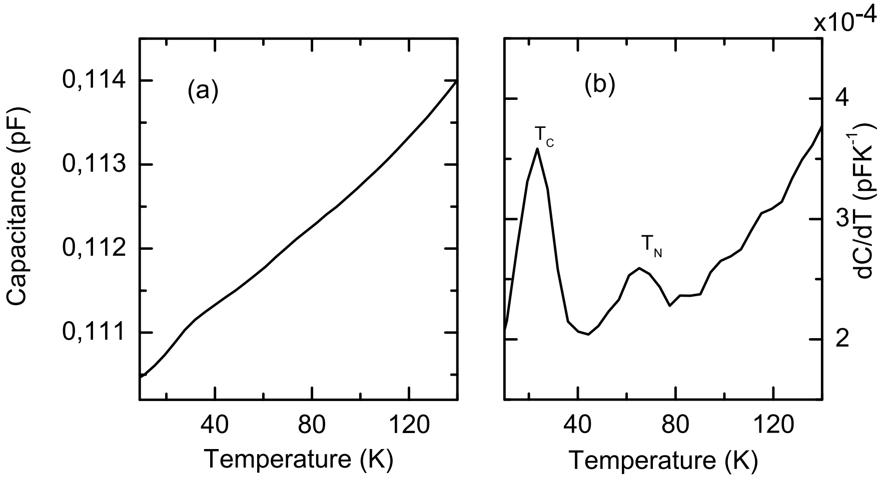

Figure 6.5: *(a) The temperature dependence of capacitance and (b) its derivative plot*

2500A 1 kHz capacitance bridge, and the temperature and magnetic field were controlled by Quantum Design PPMS (6000 model). A clear bump is observed around 25 K at capacitance curve whereas two clear bumps at 25 K and 65 K are shown by the plot of capacitance derivative, as shown in Fig. 6.5.

6.3 Raman Spectroscopy Measurement

We investigated polarized Raman spectra of $KFe_3(OH)_6(SO_4)_2$using a Jobin Yvon T64000 micro-Raman spectrometer with the 676.4 nm line of a Kr+ laser as the excitation source. The crystals used in the experiments were oriented using X-ray diffraction and mounted on the cold finger of an Oxford microstat (4-350 K) with a temperature stability of better than 0.1 K. Excitation powers have been kept below 50 mW/cm^2.

The XRD refinement result shows that the space group of iron jarosite is R-3m and the wyckoff positions of the atoms are 9d for Fe ion, 6c for S ion, 6c and 18h for O ions, and 3a for K ion. Hence, we expect Raman modes of $6A_{1g} + 8E_g$ observed. Previous studies [19–21] observed Raman modes which have been assigned as hydroxyl stretching at 3388 cm^{-1}, ν_1 symmetry stretching at 1009 cm^{-1}, antisymmetric strecthing of SO_4^{-2} at 1102 and 1011 cm^{-1}, ν_4 bending at 623 cm^{-1} with a shoulder at 632 cm^{-1}, ν_2 bending at 443.7 cm^{-1} and 452.8 cm^{-1}, Fe-O stretching mode at 434.5 cm^{-1}, and Fe-O vibrations at 365 cm^{-1} and 354 cm^{-1}.

Figure 6.6 shows our observation of Raman spectra below 400 cm^{-1} at 293 K and 10 K with the incoming and scattered light polarized along the crystallographic b-axis. Our result is in good agreement with the spectra reported earlier [19–21] except for a double peaked scattering band observed near 54 cm^{-1} at low temperatures. We observe three phonon modes in this energy range which are found at 140, 226, and 300 cm^{-1} and have been assigned as O-Fe vibrations [19, 20]. These type of Raman modes have also found in other systems possessing MnO6 octahedra such as MnO6. The 300 and 226 cm^{-1} have been attributed to rotational mode [22]. The 140 cm^{-1} is close to the frequency of oxygen vibration relative to the rare earth [22]. Thereby, we might attribute this mode to the oxygen vibration relative to the K^+ ion in our sample.

To have detail description of the phonon dynamics, we analyzed the strongest phonon mode of 226 cm^{-1} with Lorentzian functions. The thermal population is accommodated by normalizing our Raman data with Bose Einsten correction. The frequency and line width are fit with anharmonic equation. All equations used in this analysis have been written in Eq. 3-5 of chapter IV. The results are presented in Fig. 6.7.

Figure 6.7 (a) shows the evolution of phonon mode with temperature. Down to low temperature, the behaviors are characterized by the increasing of the phonon intensity, the frequency shift to higher value, and the line width narrowing. The integral of intensity as a function of temperature is presented in Fig. 6.7 (b). Below 40 K, the intensity is relatively constant. The intensity decreases gradually with temperature increasing from 40 K to 200 K. Above 200 K the integral of intensity does not show significant change. In our case, the integral of intensity might reflect the Fe-O bond strength which decreases with temperature increasing. The change of integral of intensity from 50 K up to 293 K is well fitted with exponential equation $I(T) = F - Ge^{-\Delta/T}$ with F,G, and Δ are 14, 12, and 14 K, respectively.

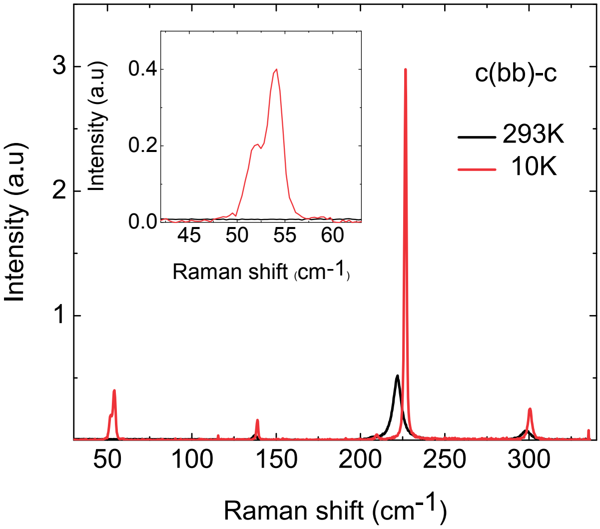

Figure 6.6: *Polarized Raman spectra* $c(bb)\bar{c}$ *at 293K and 10 K. Inset shows the appearance of new modes around 54* cm^{-1}

The result is presented as green line in Fig. 6.7 (b). The relatively constant value of integral of intensity below 50 K which deviates from the exponential behavior might relate to the presence of AFM order which the phonon energy is used to compensate the AFM exchange integral.

The phonon frequency change is shown in figure 6.7 (c). The best fit of experimental data with anharmonic equation (Eq. 4 in chapter IV) is presented as red line. The A and B are 0.12 and 0.21, respectively, which indicates that the temperature dependence of frequency behavior is dominated by four phonon process. Further analysis of the temperature dependence of line width is shown by Fig. 6.7 (d). It also follows the anharmonic behavior (Eq. 5 in chapter IV) as shown by red line. In this case, the three phonon process is dominant.

The AFM phase transition is marked by the appearance of a new Raman mode at 54 cm^{-1}. As figure 6.8 (a) shows this band appears just below the magnetic ordering transition as a weak broad feature which sharpens up and shifts to higher energy upon further lowering the temperature. The sensitivity of this mode to the AFM order suggests an assignment as tilting mode which is sensitive to the change of Fe-O-Fe angle. The intensity of this band follows the order parameter of the magnetic structure [10], as shown by blue line in figure 6.8 (b) which displays the fit of the first moment of the spectra with $(1 - T/T_C)^{\beta}$. The critical exponent β is found to 0.2. Near 30 K the mode starts to show a low energy shoulder which evolves in a clear double peak structure at lower temperatures. The frequencies

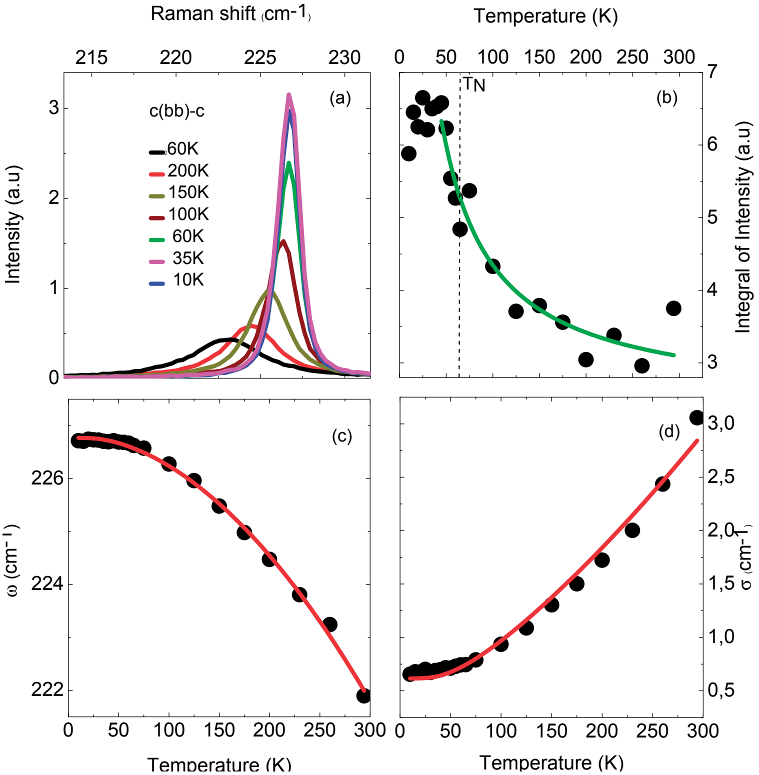

Figure 6.7: *((a) The temperature dependent evoution of phonon mode of 226 cm^{-1}. Spectra has been normalized to 300 cm^{-1} phonon mode. (b)The intensity integrated from 210 up to 235 cm^{-1}. (c) and (d) the energy shift (ω), and line brodening (γ), respectively, as function of temperature and obtained from the best fit of 226 cm^{-1} with Lorentzian function*

of the observed mode, obtained by fitting Lorentzian functions to the data are shown in Fig. 6.8(c). The energy of the band is quite close to the energy of the k=0 magnon excitation observed in inelastic neutron scattering [9], suggesting the origin of the 52 cm^{-1} mode could be from a single magnon scattering processes. However, magnetic field dependent experiments (up to 0.5 T) did not show any field induced energy shift of the band. We therefore attribute the observed band to phonon scattering, which is activated below T_N due to a magneto-elastic coupling.

In the molecular field , the phonon-spin coupling is determined by fitting the temperature dependence of frequency with $\omega = \lambda \langle S_i S_j \rangle$ [12] where λ is the spin phonon coupling proportional to the derivative of magnetic exchange constant with respect to the magnetic ion coordinates [23]. The spin coupling strength, $\langle S_i S_j \rangle$, scales with the temperature so that $\langle S_i S - j \rangle = (1 - T/T_C)^\beta$. Hence, the experimental data can be fitted with $\omega(T) = \lambda(1 - T/T_C)^\beta$. The result is presented

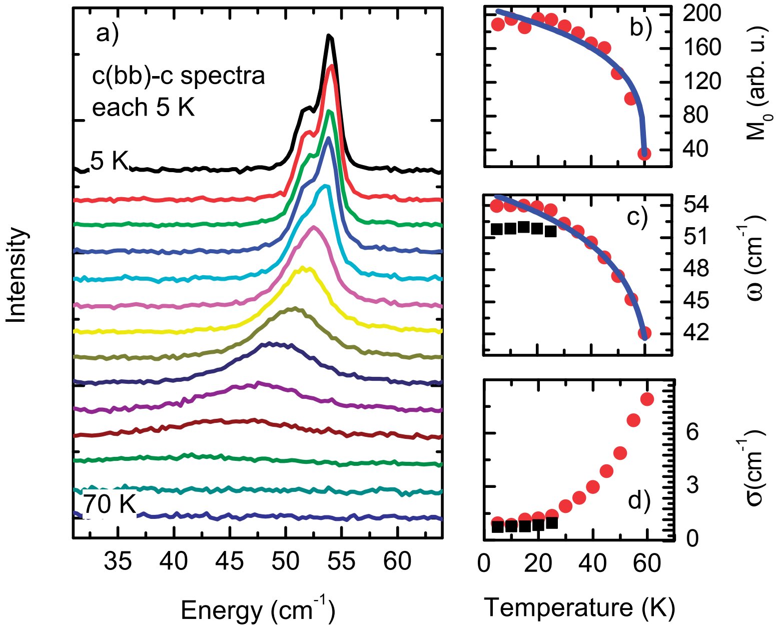

Figure 6.8: *Low energy (bb) polarized Raman spectra showing a new scattering band below* T_N*. (a) Temperature evolution between 5 and 70 K (spectra are shown each 5K). Spectra have been normalized to the integrated intensity of the strong phonon centered at 240 cm*$^{-1}$ *and have been given an incremental offset for clarity. (b) Temperature dependence of the zeroth moment M0 (integrated from 20 to 70 cm*$^{-1}$*). (c) Temperature dependence of the energy of the observed modes obtained from Lorentzian fits to the data (red circles 54 cm*$^{-1}$ *mode, black square 52 cm*$^{-1}$ *mode). Blue lines are fit with* $\lambda(1-T/T_C)^{\beta}$ *(d) Temperature dependence of the line-width of the observed modes (red circles 54 cm*$^{-1}$ *mode, black square 52 cm*$^{-1}$ *mode) obtained from Lorentzian fits to the data*

as blue line in Fig. 6.8 (c). It gives spin-phonon coupling constant of λ=55 cm^{-1} and critical exponent of $\beta = 0.09$. Further analysis of the second moment of the spectra shows that the splitting of the band occurs at 30 K, the temperature at which the largest anomaly in the static dielectric response has been observed. This result suggests the presence of magneto-electric coupling in the material.

6.4 Discussion

The appearance of a new Raman mode at 54 cm^{-1} below AFM phase transition of 65 K evidences the presence of an important spin-lattice coupling. The temperature dependent properties of phonon intensity which follows the critical exponent formula below AFM ordering temperature suggest that this phonon is activated by AFM order and might relate to change of Fe-O-Fe angle. Following the discussion of superexchange mediated magneto-elastic coupling in the triangular lattice [15], the appearance of new Raman mode is explained in terms of a magneto-elastic coupling through a modulation of the superexchange interaction. The superexchange interaction between two Fe ions in the *kagomé* plane is dependent on the Fe-O bond length and Fe-O-Fe angle. The displacement of the oxygen ion relative to the position of Fe ions may not only give rise to magneto-elastic phenomena, but also to the observed spin-phonon coupling.

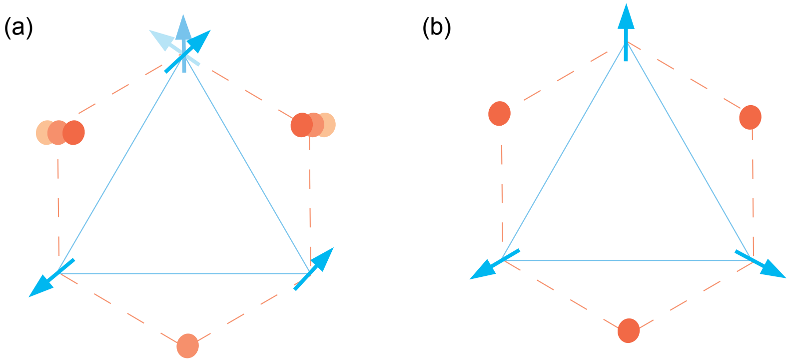

Figure 6.9: *Schematic picture of relation between magnetic order and the Fe-O-Fe bond angle and the oxygen position in a triangular lattice. (a) Above AFM phase transition, one of spin is always fluctuated due to geometrically frustrated system (shown by shaded arrows). Consequently the oxygen position is always modulated (shown by shaded circles). (b) Below AFM phase transition, the spins is stable at 120 degree configuration. The equilibrium position of oxygen is fixed*

The relation between the oxygen position and the superexchange interaction between Fe ions in a triangular lattice is sketched in Fig. 6.9. Above phase transition, the spin orientation in one of triangular corners is always fluctuated due to the geometric frustration. Consequently, there is no unique equilibrium position of oxygen ions. The oxygen position is always modulated following the spin fluctuation. Hence, there is no cooperative magnetic related Fe-O motions which generates Raman mode. On the other hand, the Fe spins form 120^0 configuration with a stable superexchange interaction below AFM phase transition as illustrated in Fig. 6.9 (b). The lattices should adjust new magnetic interaction energy by changing Fe-O bond lenghts and Fe-O-Fe angles. Consequently the oxygen ion position should also readjust to a certain fixed equilibrium position. This process cooperatively occurs for the whole crystal and generates new Raman mode.

This kind of magneto-structural effect has been observed in another frustrated system for example hexagonal manganite [24]. The isostructural change is clearly observed which the Mn-O bond length as well as Mn-O-Mn angles change below AFM phase transition without breaking the symmetry of high temperature structure. The atomic displacements occur within a unit cell and change the electronic properties of manganite which subsequently induce magneto-electric coupling in the system. In our case, the data of Fe-O bond length as well as the Fe-O-Fe angles are not available at present. However, the splitting of one hydroxyl mode into three separated modes at low temperature previously reported in Ref. [20] must indicate the presence of structural variation. The appearance of a shoulder of Raman mode below 30 K which coincides with the anomalous behavior capacitance indicate the presence of magneto-electric coupling. Further careful X-ray diffraction is required to confirm our proposal.

6.5 Conclusions

The results of Raman and dielectric experiments have shown the existence of important magneto-elastic and magneto-electric coupling in geometrically frustrated iron jarosite. It is evidenced by the appearance of new low energy modes in Raman spectrum of the antiferromagnetic phase as well as the temperature dependence of the 225 cm^{-1}, in conjunction with the magnetic ordering and the anomalous behavior of the dielectric properties. The observed phenomena are explained in terms of a magnetostrictive coupling of the displacement of oxygen ions with the magnetic superexchange interaction between the Fe^{3+} ions.

At 30 K the newly observed low energy Raman mode splits into two modes, and the dielectric properties display an clear anomaly which together suggest the occurrence of a magneto-electric coupling as well as the structural phase transition which has not been detected so far in x-ray diffraction experiments.

Bibliography

[1] A. P. Ramirez. *Journal of Physics - Condensed Matter*, 9:8171, 1997.

[2] R. Moessner and A.P. Ramirez. *Physics Today*, 81:24, 2006.

[3] John E. Greedan. *Journal of Alloys and Compounds*, 408:444, 2006.

[4] L. Balents. Spin liquid in frustrated magnet. *Nature*, 464:199, 2010.

[5] Yoshitami Ajiro, Takayuki Asano, Takeo Takagi, Mamoru Mekata, Hiroko Aruga Katori, and Tsuneaki Goto. *Physica B: Condensed Matter*, 201(0):71, 1994.

[6] T. T. A. Lummen, C. Strohm, H. Rakoto, and P. H. M. van Loosdrecht. *Phys. Rev. B*, 81:224420, 2010.

[7] S W Cheong and M Motovoy. *Nature*, 6:13, 2007.

[8] D. Grohol, D. G. Nocera, and D. Papoutsakis. *Phys. Rev. B*, 67:064401, 2003.

[9] K. Matan, D. Grohol, D. G. Nocera, T. Yildirim, A. B. Harris, S. H. Lee, S. E. Nagler, and Y. S. Lee. *Phys. Rev. Lett.*, 96:247201, 2006.

[10] T. Inami, M. Nishiyama, S. Maegawa, and Y. Oka. *Phys. Rev. B*, 61:12181, 2000.

[11] M. Elhajal, B. Canals, and C. Lacroix. *Phys. Rev. B*, 66:014422, 2002.

[12] Ch. Kant, J. Deisenhofer, T. Rudolf, F. Mayr, F. Schrettle, A. Loidl, V. Gnezdilov, D. Wulferding, P. Lemmens, and V. Tsurkan. *Phys. Rev. B*, 80:214417, 2009.

[13] K. Terao. *Journal of the Physical Society of Japan*, 65:1413, 1996.

[14] O. Tchernyshyov, R. Moessner, and S. L. Sondhi. *Phys. Rev. Lett.*, 88:067203, 2002.

[15] Kris T. Delaney, Maxim Mostovoy, and Nicola A. Spaldin. *Phys. Rev. Lett.*, 102:157203, 2009.

[16] J. Buurma. *Orbital Order and Magnetoelectric Coupling in Manganite and Jarosite.* PhD thesis, University of Groningen, 2010.

[17] D. Grohol, K. Matan, J-H. Cho, S-H Lee, J. W. Lynn, D. G. Nocera, and Y. S. Lee. *Nat Mater*, 4:323.

[18] K. Matan, B. M. Bartlett, J. S. Helton, V. Sikolenko, S. Mat'aš, K. Prokeš, Y. Chen, J. W. Lynn, D. Grohol, T. J. Sato, M. Tokunaga, D. G. Nocera, and Y. S. Lee. *Phys. Rev. B*, 83:214406, 2011.

[19] K. Sasaki, O. Tanake, and H. Konno. *The Canadian Mineralogist*, 36:1225, 1998.

[20] R. L. Frost, R-A. Wills, M. L. Weier, W. Martens, and S. Mills. *Spectrochimica Acta Part A*, 63:1–8, 2005.

[21] C. H. Chio, S. K. Sharma, L-C. Ming, and D. W. Muenow. *Spectrochimica Acta Part A: Molecular and Biomolecular Spectroscopy*, 75:162 – 171, 2010.

[22] M. N. Iliev, M. V. Abrashev, H.-G. Lee, V. N. Popov, Y. Y. Sun, C. Thomsen, R. L. Meng, and C. W. Chu. *Phys. Rev. B*, 57:2872, 1998.

[23] E. Granado, A. Garc´, J. A. Sanjurjo, C. Rettori, I. Torriani, F. Prado, R. D. Sánchez, A. Caneiro, and S. B. Oseroff. *Phys. Rev. B*, 60:11879, 1999.

[24] S. Lee, A. Pirogov, M. Kang, K-H. Jang, M. Yonemura, T. Kamiyama, S.-W. Cheong, F. Gozzo, Namsoo Shin, H. Kimura, Y. Noda, and J.-G. Park. *Nature*, 451, 2008.

Summary

This thesis presents the results of studies on the properties and related dynamical phenomena arising from the interplay between the charge, orbital, and spin degrees of freedom in correlated systems. The underlying physical mechanisms are further correlated with the crystal structure of the associated systems. The main experimental tools used in the studies are optical spectroscopies in combination with structural, specific heat, electrical transport, and magnetic characterization. The systems investigated in this thesis include the transition metal oxides of $TbMnO_3$, $Pr_{0.5}Ca_{1.5}MnO_4$, and $KFe_3(OH)_6(SO_4)_2$. A particular effort has been given to probe and explore charge-orbital ordering phenomena, formation of magnetically ordered phases, the stability and dynamics of the related phase transitions, the transient optical response, and structural changes. The main results are presented in Chapter 3, 4, 5, and 6, while chapter 1 and 2 give a general introduction and an introduction to the methods used throughout this thesis.

Chapter 3 presents the result of time resolved optical pump probe experiments on $TbMnO_3$. The time dependent optical response of the sample, following the a charge transfer process induced by a 400 nm laser, was probed with an 800 nm laser pulse by measuring the transient reflectivity. The reflection at 800 nm is sensitive to intersite *d*-*d* transitions, which themselves are sensitive to the nearest neighbour spin alignment. It is found that the time profiles of the transient reflectivity measured along the mutually perpendicular *a*-and *c*-axes exhibit a different response, originating from the ferromagnetic and antiferromagnetic nearest neighbor alignment, respectively. For both axes we observe an exponential slowing down of the dynamics below the magnetic ordering transition. The results are discussed in terms of a magnon-assisted hopping of the photo-excited electron. Further analysis of the temperature dependent variations of the transient reflectivity along both crystal axes at the metastable state around 95 ps time delay reveals a pronounced change at the magnetic phase transition temperature $T_{1,N} = 41$ K and less pronounced change at a lower transition temperature $T_{2,N} = 26$ K, as well as an indication for short range magnetic order above $T_{1,N}$. An additional experiment was performed to investigate the possible appearance of photoinduced modulation of ferroelectricity by measuring the photogenerated transient pyroelectric current. It is shown that the clearly perceptible results of temperature dependent transient

voltage and the associated electric polarization modulation do display the typical effect produced by photo excitation of ferroelectric material, even though the ferroelectric polarization in $TbMnO_3$is about 1000 times smaller than that found in conventional ferroelectric PZT.

In chapter 4, we report the results of a study on the formation of charge ordering and other ordering transitions in half doped layered manganite $Pr_{0.5}Ca_{1.5}MnO_4$. Raman spectroscopy in combination with X-ray diffraction, magnetization, resistivity, and specific heat measurements were used to clarify and elucidate the nature of those phase transitions in terms of the roles of couplings among charge, lattice, and spin degrees of freedom. The charge order at occurring at 320 K is marked, among other, by an abrupt upward jump of the resistivity and a peaking of specific heat as well as by a steep increase of the magnetic susceptibility. The coupling between the charge order and lattice structure is shown by a rapid change of lattice constant around 320 K and by the increasing orthorombicity below 320 K. Additional evidence of the coupling effects are provided by Raman spectroscopy measurements showing the lowering of structural symmetry along with the strengthening of charge order as shown by the evolution of several Raman modes which become more pronounced below 320 K. In particular, the temperature dependent intensity variation of the octahedral rotational mode at 366 cm^{-1} closely resembles an order parameter like behavior below 320 K. In addition, it has been observed that the tilting modes at 212 cm^{-1} and 180 cm^{-1} also show abrupt changes around the charge order transition temperature. Evidence for the presence of two dimensional (2D) short range antiferromagnetic order is found by the appearance of a broad maximum in the temperature dependence of the magnetic susceptibility curve around 200 K. This is coincident with the presence of a broad maximum in the temperature dependent variation of the lattice constant along the a- and b axes, and the anomalous broadening of the stretching mode observed in Raman spectroscopy data. This temperature regime is also marked by a gradual intensity change of the tilting modes at 212 and 180 cm^{-1}. The 2D nature of electronic properties in this temperature regime is further confirmed by the behavior of resistivity curve which can be well described by the 2D variable range hoping model. The formation of anti-ferromagnetic order leads to a small kink in the susceptibility curve at the Néel temperature. The strong coupling between spin order and lattice is evidenced by the decrease of orthorombicity as well as the softening of Raman tilting modes and rotation modes below the Néel temperature. The absence of entropy change at the antiferromagnetic transition temperature confirms that the short range antiferromagnetic order already exists at temperature above the Néel temperature.

Chapter 5 is devoted to the effects of optical excitation on the charge-orbital and spin orderings in $Pr_{0.5}Ca_{1.5}MnO_4$. Time resolved pump probe experiments were used, exciting the *p*-*d* charge transfer transition and probing the subsequent relaxation process through the intersite *d*-*d* transition. The optical response measured in term of transient reflectivity are shown to be strongly influenced by the charge and spin ordering. The strongest effect was observed around the charge/orbital ordering phase transition at 320 K, marked by the sharp rise of the transient reflectivity signal as temperature decreases toward 320 K and a sudden reversal of the trend right below that. Apart from the initial response (within less than 150 fs) which is beyond our experimental time resolution, the time dependent variation of the transient reflectivity exhibits a fast (1 ps) and subsequent slow ingrowth component (100's of ps) in the relaxation dynamics. The temperature dependent profiles of both relaxation times clearly exhibit the sudden reversal at 320 K. The slow component has been attributed to the occurrence of an optically induced phase transition arising through the emergence and growth of optically induced disorder domains. The formation of AFM order at lower temperatures (127 K) also influences the transient reflectivity dynamics, as exhibited by a modest speeding up of the fast response. This possibly results from of an additional charge-magnon decay channel which facilitates the relaxation process in the AFM state.

We present in Chapter 6 the result of our investigation of the magneto-elastic and magneto-electric couplings in the Jarosite compound $\mathrm{KFe_3(OH)_6(SO_4)_2}$. Raman spectroscopy was used to observe the low energy excitation spectrum across the magnetic ordering temperature. The magneto-elastic and magneto-electric couplings are revealed by the appearance of new Raman modes in $\mathrm{KFe_3(OH)_6(SO_4)_2}$ below the Néel temperature at 65 K and a new shoulder below 30 K which are correlated with the observed anomalous behaviors of the magnetization and the dielectric response. The new Raman modes are proposed to arise from the magnetostrictive coupling as a result of modulation of the Fe-O-Fe superexchange interaction by the phonons. The related shifts of oxygen ions relative to the Fe ion positions in this case are also expected to produce observable changes in the static dielectric constant.

In short, the results described in this thesis highlight the rich variety of charge, orbital, lattice, and spin ordered phases and the intriguing static and dynamic properties arising from these orderings in some of the transition metal oxides. We have addressed, by using a variety of static and time resolved techniques, some of the underlying physical interactions leading to a detailed insight in the physics of transition metal oxides.

Samenvatting

In dit proefschrift worden resultaten gepresenteerd uit een onderzoek naar de eigenschappen van gecorreleerde systemen die voortkomen uit de wisselwerking tussen de lading, orbitaal, en spin vrijheidsgraden. De onderliggende fysische mechanismen in deze systemen hangen ook samen met de specifieke kristal structuur. De belangrijkste experimentele methoden die zijn gebruikt zijn verschillende optische spectroscopieën. Deze zijn gebruikt in combinatie met structurele karakterisatie, warmte capaciteit metingen, elektrische transport metingen en magnetische metingen. De systemen die zijn onderzocht in dit proefschrift zijn de overgangsmetaal oxides $TbMnO_3$, $Pr_{0.5}Ca_{1.5}MnO_4$, en $KFe_3(OH)_6(SO_4)_2$. De focus van het onderzoek ligt op het bestuderen van lading-orbitaal ordening fenomenen; de formatie van magnetisch geordende fases; the stabiliteit en dynamica van fase overgangen; de optische response na een excitatie puls; en structurele veranderingen. De belangrijkste resultaten worden gepresenteerd in Hoofdstuk 3, 4, 5, en 6, terwijl Hoofdstuk 1 en 2 een algemene introductie zijn in de fysica van de bestudeerde materialen en de in dit proefschrift gebruikte experimentele methoden.

In Hoofdstuk 3 presenteren we resultaten van tijd-opgeloste optische 'pump-probe' metingen aan $TbMnO_3$. De tijd-afhankelijke optische respons van het sample, na excitatie door een 400 nm laser puls (een ladingsoverdracht proces), is gemeten door te kijken naar de reflectiviteitsveranderingen met behulp van een 800 nm laser puls. De reflectiviteit bij 800 nm is gevoelig voor de interatomaire *d*-*d* overgangen, welke op hun beurt weer gevoelig zijn voor de naaste-buur spin oriëntatie. We hebben laten zien dat de reflectiviteitsdynamica gemeten met een optische polarisatie langs de *a*-as zich anders gedraagt dan de dynamica bij polarisatie langs de *c*-as. Dit hebben we gerelateerd aan de ferromagnetische en antiferromagnetische naaste-buur oriëntatie, respectievelijk. Voor beide assen geldt dat de dynamica langzamer wordt beneden de faseovergang. De resultaten zijn geïnterpreteerd in termen van magnon-geassisteerde hoppen van foto ge-exciteerde elektronen. Verdere analyse van de temperatuurafhankelijke variaties van de reflectiviteit in de metastabiele toestand (95 ps de excitatie puls) laten zien dat er een grote reflectiviteitsverandering is bij de eerste magnetische fase overgang ($T_{1,N}$ = 41 K), en een kleinere verandering bij de tweede overgang ($T_{2,N}$ = 26 K) . Ook is er een indicatie gevonden voor magnetische order op kleine lengteschalen boven $T_{1,N}$. Verder is er onderzoek gedaan naar de foto-geïnduceerde modulatie van de ferro-elektrische polarisatie. Dit hebben we gedaan door de foto-gegenereerde pyro-elektrische stroom te meten. We hebben inderdaad een temperatuursafhankelijke voltage en elektrische polarisatie modulatie kunnen meten, zoals die veelal wordt gezien in andere ferro-elektrische materialen. Dit ondanks het feit dat de polarisatie in $TbMnO_3$ zo'n 1000 keer kleiner is dan in het bekende ferro-elektrische materiaal lood-zirkoontitanaat.

In Hoofdstuk 4, presenteren we resultaten van een studie naar de formatie van ladingsordening en andere ordeningsovergangen in de half gedoteerde, manganaat $Pr_{0.5}Ca_{1.5}MnO_4$. Raman spectroscopie in combinatie met Röntgendiffractie, magnetisatie, weerstand, en warmte capaciteit metingen zijn gebruikt om te kijken naar de rol van de koppeling tussen de lading, rooster, en spin vrijheidsgraden. De ladingsordening vindt plaats bij 320 K en wordt vergezeld door een sprong in de weerstand, een piek in de warmte capaciteit, en door een sterke groei in de magnetische susceptibiliteit. De koppeling tussen de ladingsordening en kristal structuur is aangetoond doordat er een verandering van de roosterconstante is gemeten in de buurt van de 320 K, en door de grote wordende orthorombiciteit beneden de 320 K. Meer bewijs voor de koppelingen komen van Raman spectroscopie metingen. Uit deze metingen kunnen we concluderen dat er een verlaging van de structurele symmetrie is, tesamen met een sterker wordende ladingsordening. Dit hebben we aangetoond door te kijken naar de temperatuursafhankelijkheid van verschillende Raman actieve vibraties. In het bijzonder, de temperatuursafhankelijke variatie in de intensiteit van de octahedrale rotationele vibratie (366 cm^{-1}) komt overeen met het gedrag van de order parameter beneden de 320 K. Ook laten de kantel vibraties (212 cm^{-1} en 180 cm^{-1}) een abrupte verandering zien in de buurt van de ladingsordening overgangstemperatuur. Bewijs voor twee dimensionale (2D), korte lengteschaal, anti-ferromagnetische ordening is gevonden doordat er een brede piek in de magnetische susceptibiliteit is, in de buurt van de 200 K. Bij de dezelfde temperatuur is de roosterconstante maximaal, en is er ook een abnormale verbreding van de strekvibratie (uit Raman data) en een intensiteitsverandering van de 212 en 180 cm^{-1} vibraties. Het 2D karakter van de elektronische eigenschappen is aangetoond doordat de temperatuursafhankelijke weerstand kan worden beschreven met het 2D variable-afstand-hoppen model. De vorming van anti-ferromagetische ordening leidt tot een kleine kink in de susceptibiliteit bij de Néel temperatuur. Ook is er bewijs gevonden voor een sterke koppeling tussen de spin ordening en het rooster, doordat we een verlaging van de orthorombiciteit hebben kunnen meten en omdat er een verzachting van Raman kantel en rotationele vibraties is gemeten beneden de Néel temperatuur. Het feit dat er geen entropie verandering is bij de anti-ferromagnetische overgangstemperatuur laat zien dat de korte lengteschaal anti-ferromagnetische ordening al bestaat boven de Néel temperatuur.

Hoofdstuk 5 gaat over de invloed van een optische excitatie op de lading en spin ordening in $Pr_{0.5}Ca_{1.5}MnO_4$. We hebben tijd-opgeloste 'pump-probe' metingen gedaan: we maakten een *p*-*d* ladingsoverdrachtovergang waarna we vervolgens keken naar de interatomaire *d*-*d* overgangen (als functie van de tijd). De lading en spin ordening hebben invloed op de optisch geïnduceerde veranderingen in de reflectiviteit. Het sterkste effect werd gezien bij de faseovergangstemperatuur (T=320 K). Boven deze temperatuur is er een sterke groei in de optische geïnduceerde reflectiviteitsverandering. Afgezien van de zeer snelle respons ($<$ 150 fs, korter dan onze experimentele resolutie) is er in de tijdsafhankelijke variatie van de reflectiviteit een snelle (1 ps) en een langzame ingroeiende component (honderden ps). De temperatuursafhankelijke dynamica verandert bij 320 K. De langzame component relateren we aan de groei van optische geïnduceerde wanordelijke domeinen. De formatie van de anti-ferromagetische ordening beneden de 127 K beïnvloed ook de optisch geïnduceerde veranderingen in de reflectiviteit: de snelle component wordt nog een beetje sneller. Dit komt mogelijk door het actief worden van een lading-magnon relaxatie kanaal in de anti-ferromagnetische toestand.

In Hoofdstuk 6 presenteren we resultaten uit ons onderzoek naar de magneto-elastische en magneto-elektrische koppelingen in het Jarosite materiaal $KFe_3(OH)_6(SO_4)_2$. Raman spectroscopie is gebruikt om te kijken naar het lage energie excitatie spectrum boven en beneden de magnetische ordeningstemperatuur. Bewijs voor de magneto-elastische en magneto-elektrsiche koppelingen komen van de verschijning van nieuwe Raman actieve vibraties in $KFe_3(OH)_6(SO_4)_2$ beneden de Néel temperatuur (65 K), en door de observatie van een nieuwe actieve vibratie beneden de 30 K. Deze vibraties zijn gecorreleerd aan het abnormale gedrag van de magnetisatie en van de dielektrische respons. De activering van de nieuwe Raman vibraties ontstaat waarschijnlijk door magnetostrictie. De magetostrictie ontstaat door een modulatie van de Fe-O-Fe superuitwisselingsinteractie door de fononen. De verschuiving van de zuurstof ionen ten opzichte van de positie van de ijzerionen resulteert waarschijnlijk ook in de waargenomen verandering van de dielektrische constante. De resultaten die zijn beschreven in dit proefschrift laten zien dat er in de overgangsmetaal oxides lading, orbitaal en spin geordende fases zijn met interessante statische en dynamische eigenschappen. We hebben, gebruikmakend van een verscheidenheid aan statische en tijdsopgeloste methoden, enkele van de fysische mechanismes ontrafeld die ten grondslag liggen aan de rijkdom van electronische eigenschappen van overgangsmetaal oxides.

Acknowledgments

This part is dedicated to individuals and institutions that gave supports and contributions during my PhD studentship.

First, I would like to express my gratitude to Prof. Dr. Ir. Paul van Loosdrecht, my supervisor and promotor. Paul, I met you for the first time in your solid state class 11 years ago. Together with Katarzyna, you introduced me to research in optical condensed matter physics. And it continues until now. I have learned a lot from you, not only about physics, but also about the way you manage the group, how you deal with a lot of types of students and people, and your different perspectives and views. I like to thank you for the support you have given to me, from the beginning when I applied for the scholarship until I finished my thesis. Your support has opened a lot of opportunities for me to work and get experience in a great academic environment. Thank you for your patience in guiding me during my PhD time. I hope this work will be continued in the form of new projects and collaborations in the future.

Second acknowledgment goes to Dr. Agung Nugroho, my supervisor and co-promotor. Pak Agung, you suggested I apply for the Schlumberger Faculty and Future Program, which was the first step for my PhD studentship. Thank you for your time and support. I enjoy our discussions and my stay in your group. I hope this graduation is not the end, but the beginning of more science and collaborations in the future.

I also would like to show my gratitude to Prof. Dr. Tjia May On. Pak Tjia, you never officially became my supervisor, but you have dedicated a lot of time to thinking about, discussing on, and correcting of my work, even at times when you were not so healthy. Thank you for being a member of reading committee. Your comments and suggestions improved my thesis a lot.

My acknowledgments also go to Schlumberger Faculty for Future Program and the Nuffic Netherlands Fellowship Program for financial support. Science is kind of a luxury in a developing country like Indonesia. These programs have opened ways for developing my career in science. Thank you to Eve Millon and all people in Schlumberger Foundation. Thank you to Wiebe Zijlstra for all help related to Nuffic.

My work would not have been possible without the kind contributions and collaborations of many. Thanks to Dr. Tom Lummen and Dr. Daniele Fausti who reminded me again about Raman spectroscopy after 2,5 years of absence in this field, and helped me a lot in performing Raman spectroscopy on the pyrochlore and $CuFeO_2$ samples. Dr. Dmitry Mazurenko, thank you for helping me with the time resolved spectroscopy measurement and your contribution to the TMO project. I am also grateful to Dr. Nandang Mufti for providing the $TbMnO_3$ sample with its characterization results, and measuring the specific heat of the $Pr_{0.5}Ca_{1.5}MnO_4$ sample. Dr. Ra'anan Tobey, thank you for your kind contributions to the $TbMnO_3$ project, in particular for help with writing the paper. My gratitude also goes to Dr. Graeme Blake, Dr. Syarif Riyadi, and Dr. Syivakumara Giriyapura for their help in measuring XRD and magnetic properties of $Pr_{0.5}Ca_{1.5}MnO_4$. Prof. Parmigiani, Dr. Andrivo Rusydi, and Dr. Aziz Majidi, thank you for the valuable discussions on the $Pr_{0.5}Ca_{1.5}MnO_4$ project. Thank you Dr. Johan Buurma and Prof. Thom Palstra for providing the nice sample and your contributions to iron jarosite project. I would like to show my gratitude to the reading committee members, Prof. Dr. D. Khomskii and Prof. Beatriz Noheda for their kind words and remarks. My thanks also go to Dr. Maxim S. Pchenitchnikov for his valuable comments during group meetings. For Alex Polyakov, thank you for sharing your knowledge on pyroelectric measurements.

Experimental work would not be easy without help from technicians. Thank you Ben Hesp, Foppe de Haan, Arjen Kamp, and Jacob Baas. For Ben, I also like to thank you for taking care of financial matters. For Foppe, thank you also for three dimensional picture of *d*-orbitals. For all administrative and paper work, I like to thank Jeannette de Boer, Annette Koringa, Elly Eekhof, and Yvonne van der Weerd.

I had a great time during my stay in the OCMP group. For that, I like to thank Toni Caretta who helped a lot with experimental work, shared the Raman and time resolved set up, shared a room with me for quite some time , shared ideas and thoughts, played pingpong, and often used his strong hands to push my slow bicycle so I could arrive faster in the lab. For my dear paranimfen, Katya and Vlad, life would have been so boring without the mafia game, visiting the X-mas market, and movie nights. Thank you for the great time together. Thank you also for helping me in preparing my defense. Michiel, thank you for sharing your experience and ideas with me. Thank you also for translating my thesis summary into a thesis samenvatting. For all members of OCMP group Almis, Matteo, Marian, Qi, Julius, Daniele, Tom, Pedro, Dima, Patricio, Silviu, Filippo, Artem, Ramunas,

Gloria, Ranjan, Dan, Ron, Dmitry, Ben, Foppe, Arjen, Jeannette, Maxim, Douwe, Audrius, Rob, Lili, Yajun, Ryota, Silviu, Victor, Ruben, Renate, and Sonya, thank you for always being nice to me, for your help, for all discussions and jokes, for lunch-coffee-tea-cake-ice cream time, outdoor activities, X-mas dinners, pingpong, mafia game, and movie nights. I miss all of them. I wish to have a happy reunion with you someday. A special memory goes to Katarzyna whom my work has been greatly influenced by the lessons and experience I learned from her. I wish you rest in peace, Katarzyna.

Life in Groningen has been very pleasant, not in the last place because of the presence of the Indonesian community. My thanks goes to Tante Pantja-Om Basuki for allowing me to stay in your lovely and warm house in the Haydnlaan, Itob for reserving a nice room in the Westerbadstraat, mbak Ike, Dini, Uyung, and Adit for sharing home sweet home in the Westerbadstraat, and Guntur-Intan for allowing me to join your lovely family in the Snelliusstraat. Ria Abdilla, thanks for being a nice house mate and a great partner in finding cheap beautiful flowers on the *bloemen markt.* For Titin, thanks for being a lovely house mate and ”little sister” who never complained anytime I was teasing you after my tiring day. Thanks to Nandang-Nisa, Iging-Desty, and Amel-Puti from whom I benefited academically since their husbands were working in the Zernike Institute and helped me a lot with experimental and academic matters, and who were always so lovely and offered help for a lot of stuff outside the university. I also like to thank mas Ismail-mbak Agnes, mas Eko-mbak Inne, mas Yayok-mbak Lia, Wahono-Dini, Fean, teh Enci-pak Intan, Helmi, Nizar, Muiz-Sri, Mas Chalid-mbak Nona, mbak Tina, Neng, Wiwin, mas Hengky-mbak Erna, pak Adi-mbak Sista, mbak Mita-mas Fajar, Yota, Kadek, Nizar, Hendi, Lia-Robby,Rachma, Erith-Iqbal, mbak Ratna-Arvi, Pak Miming, Delik-Putri, mbak Poppy, Mutia, Wisnu-Yuli, mbak Roga, Okta, mbak Yuni, Nida-Budi, mbak Ida, Nofian, Fajar, Astri-Kimia, Astri-UMCG, mbak Astri, Shanti, wak As, Bude Nani, Titah, Tante Silvi, Om Rudi, Tante Tini, Kadek, Doni-Nieke, bang Fany, Pandji-Faizah, Bayu-Indras, Alia-Izul, Irvan, Hafiz, Teguh-Tessa, Margareth, mbak Ros, Kenzi, Boy Fachri, Muhsin and all Indonesian in Groningen. Thanks for sharing a lot of things during my stay in Groningen especially during badminton, photo sessions, *makan-makan*, *silaturahmi*-deGromiest, and PPIG activities.

I also want to show my gratitude to Helga, Yari, and all member of WIRE (Welcome International Researchers and Employees) for always updating information and facilitating activities which gave me opportunity to know more about Netherlands, Groningen, and RUG as well as to meet people from different nations, cultures, and various subjects of study. Thank you for all hospitalities.

To all members of Physics of Magnetism and Photonics Group-Bandung Institute of Technology, Dr. Alex Iskandar, Dr. Herman, Dr. Rahmat Hidayat, Dr. Agus

Suhaeni, Dr. Daniel Kurnia, Dr. Inge M. Sutjahja, and Dr. Priastuti Wulandari, thank you for all hospitality during my sandwich program in the group. The sandwich time would have been much less fun if there were no Riser, Thoeng, Putu, Indra, Widi, Radius, Bakti, Juliar, Yonan, Ikah, Nina, Finy, Maureen, Nadia, mbak Elly, and Bintoro. Thanks for always making me laugh and feel happy. I wish you all good luck with your life and careers.

I like to thank all members of the Science Department-Telkom University for all support and flexible time constraints during the finishing period of my thesis. To Pak Suwandi and mbak Wati, thank you for your support and understanding. To Pak Indra, bu Herti, Bu Amaliyah, Pak Ramdlan, Pak Reza, Pak Qurtobi, Pak Mamat, and Pak Dudi thanks for always being nice friend and sharing some important news and responsibilities. Pak Adi, Pak Erwin, Pak Putu, Pak Asep, Pak Tri, Teh Silvi, Teh Dinda, and all members of the science department, thank you for your kind help. Thank you to Iwan Cony for designing the cover and invitation.

Despite great lessons and experience, life as a PhD student was not always easy. I was lucky to have mbak Ike, Uyung, Rany, Insanu, Mira, Ari, mbak Nurul, and mbak Azki to share all my problems, ideas, happiness, challenges, experiences, stories, and sometimes sadness. Surrounded by you during my PhD time convinced me that I was not alone and I should not be so worried when the times were difficult. Thank you for being great companions. I wish you all blessing and happiness. My gratitude is also going to mbak Diyas, who took care of ”Amanah Puri” during my stay in Groningen. *Matur nuwun mbak, mugi-mugi tansah diparingi berkah.* To Ati and mas Hendrarto, thank you for accompanying me and taking care of my stuff when I was in hectic times between Groningen and Bandung. Thank you to Shinta, Kanza, Seto, Jane, and Ari for being nice house mates during my sandwich time in Bandung. To mbak Diana, mbak Heni, mbak Pongky, Dije, Ican, Wangsa, Jupe, Ida, and Mimien, thanks for always being a friend, sharing moments and stories. I wish we will have more time to visit each other after this graduation.

My special thanks go to my family in Magelang. Pak Yani-mbak Ning, Bude Pic, Pak Yadi-Bu Tuti, you are my parents now. Thank you for your love and care. To Hesti, Haris, Tea, Wiwis, Atur, mbak Titik, mbak Sedar, mas Toat, and mbak Tiyo, I am happy to grow together with you. Thanks for all your help and support. To Agung, Indras, Nasta, and Akka, my life is not complete without all of you. Thanks for your love and understanding. Last but not least, I like to share a special memory of my mother. She expected me to go to graduate school and become a lecturer in a university someday. For her, being lecturer in university is a great honor. I disagreed with her at that time and in the end she said I was free to choose my own way. Now, about 17 years after she passed away, I finally complete her expectation. Ibu, I dedicate this book specially to you. I love you and I wish you rest in peace.

About the author

Name : Ismudiati Puri Handayani
Place, date of birth : Magelang, 12 Maret 1976
Sex : Female
Current Position : Lecturer in Telkom University, Indonesia.
E-mail : iphandayani@telkomuniversity.ac.id, i.p.handayani@rug.nl

Educations :

- Physics Department, Gadjah Mada Univeristy, Indonesia (Bachelor, 1999)
- Physics and Astronomy, University of Groningen, The Netherlands (Master, 2004)
- Zernike Institute for Advanced Materials, University of Groningen, The Nethelands (Doctoral, 2014)

Scholarships :

- Astra Top Student Scholarship for Bachelor Study
- Eric Bluemink Fund for Master Study
- Schlumberger Faculty for Future and Netherlands Fellowship Program for Doctoral Study

List of Publications :

- Dynamics of photo-excited electrons in magnetically ordered $TbMnO_3$
  I P Handayani, *R I Tobey, J Janusonis, D A Mazurenko, N Mufti, A A Nugroho, M O Tjia, T T M Palstra and P H M van Loosdrecht*, Journal of Physics : Condensed Matter, 25,116007 (2013)
- Photo-induced Modulation of Ferroelectric Polarization in Multiferroic $TbMnO_3$
  I.P. Handayani, *N. Mufti, A.A. Nugroho, M.O.Tjia, T.T.M. Palstra , and P.H.M. van Loosdrecht*, International Conference of Information and Communication Technology (ICoICT), 350 (2013).

- Probing magnetic order in $CuFeO_2$ through nuclear forward scattering in high magnetic fields
  C. Strohm, T. T. A. Lummen , ***I. P. Handayani****, T. Roth, C. Detlefs, P. J. E. M. van der Linden, and P. H. M. van Loosdrecht*, Physical Review B, 88, 060408(R) (2013)

- Temperature-dependent and anisotropic optical response of layered $Pr_{0.5}Ca_{1.5}MnO_4$ probed by spectroscopic ellipsometry
  M. A. Majidi, E. Thoeng, P. K. Gogoi, F. Wendt, S. H. Wang, I. Santoso, T. C. Asmara, ***I. P. Handayani****, P. H. M. van Loosdrecht, A. A. Nugroho, M. R¨ubhausen, and A. Rusydi,* Phys. Rev. B 87, 235135 (2013)

- Effects of charge-orbital order-disorder phenomena on the unoccupied electronic states in the single-layered half-doped $Pr_{0.5}Ca_{1.5}MnO_4$.
  V.Capogrosso,M.Malvestuto, ***I. P. Handayani****, P. H. M. van Loosdrecht, A. A. Nugroho, E. Magnano, and F. Parmigiani*, Physical Review B. 87,155118 (2013)

- Spin-lattice coupling in iron jarosite
  A.J.C.Buurma, ***I.P.Handayani****, N. Mufti, G.R. Blake, P.H.M. van Loosdrecht, and T.T.M. Palstra*, Journal of solid state chemistry, 195, 50 (2012)

- Phonon and crystal field excitations in geometrically frustrated rare earth titanates
  T.T.A.Lummen, ***I.P. Handayani****, M. C. Donker, D. Fausti, G. Dhalenne, P. Berthet, A. Revcolevschi, and P. H. M. van Loosdrecht*, Physical Review B, 77, 214310(2008)

- Para-excitons in Cu_2O-a new approach
  K. Karpinska, P.H.M. van Loosdrecht, ***I.P. Handayani****, A. Revcolevschi*, Journal of Luminescence 112, 17 (2005)